Bone microarchitecture but not bone healing is compromised by lack of the *Trpc1* gene and generation of mouse strains to visualize and to delete the *Trpc1* gene in a cell-specific way

Dissertation submitted for obtaining the university degree of

Doctor rerum naturalium

Ahsan Raza

born on 6th December 1988

Multan, Pakistan

Institute of Experimental and Clinical Pharmacology and Toxicology

Faculty of Medicine

Saarland University

2018

Doctoral supervisor: Prof. Dr. Veit Flockerzi

Acknowledgements

Firstly, I would like to express my sincere gratitude to my advisor Prof. Dr. Veit Flockerzi for his continuous support and motivational ideas during my doctoral research. His guidance has made all this possible.

The goal of achieving a doctoral title would never be possible without the utmost support of my mentor Dr. Bram van der Eerden, Erasmus Medical Centre, Rotterdam. I am very grateful for all his efforts in teaching me the µCT techniques for the bone analysis.

I would like to pay my gratitude to Dr. Stefanie Mannebach and Dr. Petra Weissgerber for their kind support, especially Dr. Mannebach for showing me the cloning and cell culture. I would like to thank Dr. David Stenger for showing me the fracture model and Prof. Dr. Michael D. Menger and Prof. Dr. Matthias Laschke for their scientific ideas and allowing me to perform µCT scanning and surgery in their laboratory. I thank Prof. Dr. Ulrich Boehm (Homburg) for providing me certain plasmids and reporter mouse strains and Prof. Dr. Marc Freichel (Heidelberg) for ES cell culture and injection of clones.

My sincere thanks go to Stefanie Buchholz for the cloning troubleshooting and showing me Southern blot. I would like to thank all members of the animal facility for providing me the experimental mice, especially Tanja Maurer and Tom Janke for the embryo transfer and successful handling of the mice breeding. I would like to pay my gratitude to Claudia Ecker for being a helpful organizer and the technical support from Martin Simon-Thomas and Kathrin Schetting.

My sincere gratitude for the unparalleled affection and prayers of my parents, loving sisters and a brother. Saima's love and Amal's smile served as a driving force. Thanks also go to my friends from both Pakistan and Germany for encouraging me to survive through this journey.

Table of contents

List of Abbreviations

≈	approximately
µCT	micro-computed tomography
µg	Microgram
µL	Microliter
µm	Micrometer
µM	Micromolar
v/v	Volume per volume
w/v	Weight per volume
°C	Degree Celsius
$AgNO_3$	Silver nitrate
ALP	Alkaline phosphatase
bp	Base pair(s)
BMD	Bone mineral density
BSA	Bovine serum albumin
BV	Bone volume
Ca	Calcium
Ca^{2+}	Calcium ions
Cat K	Cathepsin K
cDNA	Complementary deoxyribonucleic acid
cm	Centimeter
Cre	Cre recombinase
CSF-1	Colony stimulating factor 1
Cs.Th	Cross-sectional thickness
DKO	Double knockout (double gene deficient)
DMEM	Dulbecco's modified eagle medium
DMSO	Dimethylsulfoxide
DNA	Deoxyribonucleic acid
dNTP	2'-Deoxynucleoside-5'-Triphosphate (dATP, dTTP , dGTP or dTTP)
DTA	Diphtheria toxin A fragment
E	Embryonic day
E.coli	Escherichia Coli
EDTA	Ethylene diamine tetra acetic acid
Ec.V	Endocortical volume
ES cells	Embryonic Stem cells
et al.	*et alii/aliae*

FBS	Fetal bovine serum
Flp	Flp recombinase
FRT	Flp recombination target
Fwd	Forward
g	Gram(s)
gDNA	Genomic DNA
GFP	Green fluorescent protein
HCl	Hydrochloric acid
h	Hour(s)
IRES	Internal ribosome entry site
iTL	Ingenious Targeting Laboratory
κ	Kappa
Kb	Kilo base pairs
KCl	Potassium chloride
KI	Knock-in
KO	Knockout (gene deficient)
kV	Kilovolts
L	Liter
LB	Luria-Bertani (medium)
loxP	Locus of recombination in P1
M	Molar
MEM	Modified eagle medium
mg	Milligram
min(s)	Minute(s)
mL	Milliliter
$MgCl_2$	Magnesium chloride
mM	Millimolar
mRNA	Messenger ribonucleic acid
ms	Millisecond(s)
mt	Mutant
mV	Millivolt
Na^+	Sodium ion
NaCl	Sodium chloride
NaOH	Sodium hydroxide
$NaCO_3$	Sodium carbonate
$Na_2S_2O_3$	Sodium thiosulphate
Neo	Neomycin resistance gene

nt	Nucleotide(s)
OBs	Osteoblasts
OCs	Osteoclasts
OD	Optical density
P	Phosphorus
poly A	Polyadenylation signal
PBS	Phosphate buffered saline
PCR	Polymerase chain reaction
PEG	Polyethylene glycol
pgk	Phosphoglycerate kinase
pH	Negative logarithm of the hydrogen ion concentration in mol/L
PIP2	Phosphatidylinositol-4,5-bisphosphate
PLC	Phospholipase C
RANK-L	Receptor activator of NF-kappa B ligand
Rev	Reverse
RNA	Ribonucleic acid
ROI	Region of interest
rpm	Rotations per minute
RT	Room temperature
RT-PCR	Reverse transcription-PCR
SDS	Sodium dodecyl sulfate
sec or s	Second
SSC	Sodium, sodium citrate solution
TAE	Tris base/acetic acid/EDTA-solution
Taq	Thermus aquaticus
Tb.N	Trabecular number
Tb.Pf	Trabecular pattern factor
Tb.Sp	Trabecular separation
Tb.Th	Trabecular thickness
TE	Tris-EDTA
TM	Transmembrane
Tm	Melting temperature
TMD	Tissue mineral density
TNFSF11	Tumor necrosis factor (ligand) superfamily, member 11
TRACP	Tartrate resistant acid phosphatase
TRANCE	TNF-related activation-induced cytokine
Tris	Tris-(hydroxymethyl)-aminomethane

TRP	Transient receptor potential
TRPC1	Transient receptor potential canonical 1
TRPC1-IC	TRPC1-IRES-Cre
TRPV6	Transient receptor potential vanilloid 6
TV	Tissue volume
Tween-20	Polyoxyethylenesorbitan monolaurate 20
U	Unit (enzymatic activity)
UV	Ultraviolet
V	Volume
VOI	Volume of interest
w	Weight
WT/wt	Wild-type
x g	Times Earth's gravitational force

List of Figures

List of Tables

Summary:

The genes of TRP channel subunits are expressed in many tissues. I identified transcripts of *Trpc1* and *Trpv6* in bone. In order to understand their function in bone, I studied the bone phenotype in mice lacking *Trpc1* (*Trpc1*$^{-/-}$), in mice carrying a non-functional mutation of *Trpv6* (*Trpv6*$^{mt/mt}$), in mice carrying both mutations and in wild-type mice. To this aim, I had first to establish µCT measurements using femur as a long bone and to determine age-dependent changes of femurs from wild-type mice on a C57BL/6 ("B6") and on a 129SvJ/C57BL/6 ("mixed") genetic background to exclude genetic heterogeneity, which might affect the bone phenotype. Femur length was shorter, endocortical volume was reduced and cross-sectional thickness was increased in *Trpv6*$^{mt/mt}$ mice whereas the bone volume fraction, mineral density and thickness of trabecular bone was reduced in *Trpc1*$^{-/-}$ mice. In the double mutant mice, the cortical bone phenotype of *Trpv6*$^{mt/mt}$ mice was not compensated by the deletion of *Trpc1* whereas the effect of *Trpc1* deletion on trabecular bone was compensated by the *Trpv6* mutation.

I also established a femur fracture model, set up a tasklist for analyzing the callus formation by µCT and used a three-point bending test to estimate the biomechanical stiffness of the femur. Mineralization of callus was increased in *Trpv6*$^{mt/mt}$ mice but I did not observe any difference in stiffness comparing all four mouse strains.

Because of the positive bone phenotype of *Trpc1*$^{-/-}$ mice, I examined osteoclasts and osteoblasts isolated/differentiated from bone marrow cells and bone pieces for *Trpc1* expression. Both cell types were positive. In order to visualize *Trpc1* expressing cells and to delete *Trpc1* in a cell-specific way, I generated two novel mouse strains from scratch by homologous recombination: A *Trpc1*-IRES-Cre mouse strain and a "floxed" *Trpc1* mouse strain. Pups of both stains are available and with *Trpc1*-IRES-Cre strain, we already visualized *Trpc1* expressing cells in various tissues including bone. Together with the *Trpc1* "global" knockout mice (studied for their bone phenotype), the two novel *Trpc1* strains allow dissecting *Trpc1* function in a cell-specific way, especially in bone.

Zusammenfassung:

Die Gene von TRP-Kanal Untereinheiten werden in vielen Geweben exprimiert. Ich habe *Trpc1* und *Trpv6* Transkripte in Knochen identifiziert. Um deren Funktion im Knochen zu verstehen, habe ich den Knochenphänotyp von Mäusen, denen das *Trpc1*-Gen (*Trpc1*$^{-/-}$) fehlt, Mäusen die eine Kanal-inaktivierte Mutation von *Trpv6* (*Trpv6*$^{mt/mt}$) aufweisen, Mäusen welche beide Mutationen aufweisen (*Trpc1*$^{-/-}$/ *Trpv6*$^{mt/mt}$) und Wildtyp Mäuse untersucht. Für dieses Ziel musste ich zuerst µCT Messungen, unter der Verwendung von Femur als Röhrenknochen, etablieren, sowie die altersabhängigen Veränderungen der Femora von Wildtyp Mäusen und die genetische Heterogenität, die den Knochenphänotyp betreffen könnte, bei Mäusen mit einem C57BL/6 („B6") sowie einem 129SvJ/C57BL/6 („gemischtem") genetischen Hintergrund, bestimmen. Der Femur von *Trpv6*$^{mt/mt}$ Mäusen war kürzer, das endokortikale Volumen reduziert und die Dicke des Querschnitts erhöht. Da waren bei Femora von *Trpc1*$^{-/-}$-Mäusen der Anteil des Knochen Volumens, die Mineraldichte und die Dicke der Trabekel vermindert im Vergleich zu Femora. Bei den Mäusen mit Doppelmutation wurde der kortikale Knochenphänotyp von *Trpv6*$^{mt/mt}$ Mäusen nicht durch die Deletion von *Trpc1*$^{-/-}$ kompensiert, wohingegen der Effekt der *Trpc1*$^{-/-}$ Deletion auf den trabekulären Knochen durch die Mutation von *Trpv6* kompensiert wurde.

Gleichzeitig habe ich ein Frakturmodell des Femurs etabliert, eine Tasklist entwickelt zur Analyse der Kallusbildung mittels µCT und einen 3-Punkt-Biegeversuch angewendet, um die biomechanische Steifheit des Femur einzuschätzen. Die Mineralisierung des Kallusgewebes bei *Trpv6*$^{mt/mt}$ Mäusen war erhöht, allerdings konnte ich beim Vergleich aller vier Mauslinien keine Unterschiede in der Steifheit feststellen.

Wegen des eindeutigen Knochenphänotyps bei *Trpc1*$^{-/-}$ Mäusen, habe ich Osteoklasten und Osteoblasten isoliert bzw. differenziert aus Knochenmarkzellen und Knochenstückchen auf *Trpc1*-Expression untersucht. Beide Zelltypen waren positiv. Um *Trpc1*-exprimierende Zellen sichtbar zu machen und um *Trpc1* zellspezifisch auszuschalten, habe ich zwei neue Mauslinien mittels homologer Rekombination von Grund auf neu hergestellt: Eine *Trpc1*-IRES-Cre Mauslinie und eine „gefloxte" *Trpc1* Mauslinie. Die Nachkommen beider Linien sind verfügbar und mit der *Trpc1*-IRES-Cre Linie haben wir bereits *Trpc1* exprimierende Zellen in mehreren Geweben, inklusive Knochen, sichtbar gemacht. Gemeinsam mit der bis ausschließlich

verfügbaren *Trpc1* „globalen“ Knock-out Linie (die ich im Hinblick auf einen möglichen Knochenphänotyp untersucht habe), erlauben die zwei neuen *Trpc1* Linien die *Trpc1* Funktion detailliert und zellspezifisch, besonders im Knochen, zu untersuchen.

1 Introduction

1.1 Bone

Bone is a dynamic tissue organized as a framework to form a skeletal system in organisms. The skeleton plays several significant roles in the body such as protection *e.g.* the skull protects the brain, movement and locomotion, *e.g.* the organisms move due to the coordinated function of bone and muscles, and reservoir, such as the bones serve as a storage unit for minerals like calcium, phosphate and magnesium. In bone, principally there are two main cell types: Bone forming osteoblasts and bone resorbing osteoclasts, which work in a balanced fashion to maintain normal bone structure (Allen and Burr, 2014). The skeleton is continuously changing under the effects of modelling and remodeling processes (Katsimbri, 2017). Modelling includes the change in shape or size of bones mostly occurring early in development, for instance during growth of long bones. On the other hand, remodeling involves the maintenance of the structure of bones throughout the lifespan due to the coordinated activity of osteoblasts and osteoclasts (Kobayashi *et al.,* 2003).

1.1.1 Osteoblasts

Osteoblasts are specialized bone-forming cells located on the outer surfaces of bone and within the bone cavities and derived from pluripotent mesenchymal stromal cells (Katsimbri, 2017). Various signaling pathways, for instance, a Wnt signaling pathway (Day *et al.,* 2005) and proteins such as bone morphogenetic proteins (BMP) (Cao and Chen, 2005) play a vital role in osteoblasts differentiation and function. The Wnt signaling pathway, which activates ß-catenin (canonical Wnt signaling pathway) leads to the up-regulation of transcriptional factors, required for differentiation and maturation of osteoblasts and ultimately increases bone mass (Monroe *et al.,* 2012). The process for the formation of osteoblasts is called osteoblastogenesis. They start to build up the bone by the synthesis and secretion of type-I collagen and other, mostly non-collagenous specialized extracellular matrix proteins, which form the unmineralized organic matrix called osteoid. It serves as a template for osteoblasts to deposit minerals in the form of hydroxyapatite crystals leading to the formation of bone. A fraction of osteoblasts remains in the osteoid and are known as osteocytes (Katsimbri, 2017). Another small part of osteoblasts become bone lining cells covering quiescent parts of the

bone. The remainder 60-80% of the cells undergo apoptosis after completing the process of bone formation.

1.1.2 Osteoclasts

Osteoclasts are large multinucleated cells derived from mononuclear precursor cells of the monocyte macrophage lineage capable of resorbing the bone (Teitelbaum and Ross, 2003). The differentiation process of osteoclasts from their precursor cells, known as osteoclastogenesis, primarily depends on two important cytokines namely CSF-1 (colony stimulating factor 1) and RANKL (receptor activator of nuclear factor NF-κB ligand) (Yoshida *et al.,* 1990), which signal through c-fms (the receptor of macrophage colony stimulating factor, M-CSF) and RANK, respectively (Katsimbri, 2017). Resorption of bone starts when mature osteoclasts adhere to the bone surface and become polarized to produce villus-like projections (podosomes) and distinct membrane domains, the sealing zone (SZ), the ruffled border (RB) and the functional secretory domain (FSD) (Katsimbri, 2017) **(Figure 1-1)**. The SZ provides firm adhesion of the osteoclasts to the bone surface and isolates the acidic environment required for resorption from the neighboring bone matrix. Osteoclasts then start secreting several acids such as citric, hydrochloric and lactic acids at the RB in a tightly closed compartment to resorb the bone (Luxenburg *et al.,* 2007) and proteolytic enzymes such as Cathepsin K (Cat K) for degradation (Yamaza *et al.,* 1998). After degradation, the degraded collagen as well as mineral residues such as Ca^{2+} and PO^{4+} are phagocytosed by the osteoclasts and either get dissolved by lysosomes or enter the functional secretory domain (Nesbitt and Horton, 1997) eventually being released into the blood stream by the process termed as transcytosis. After completing the bone resorption process, osteoclasts undergo apoptosis (programmed cell death) due to increased extracellular Ca^{2+} levels. Dysregulation of osteoclasts such as increased activity may lead to a condition known as osteoporosis, whereas compromised functionality may cause osteopetrosis (Katsimbri, 2017).

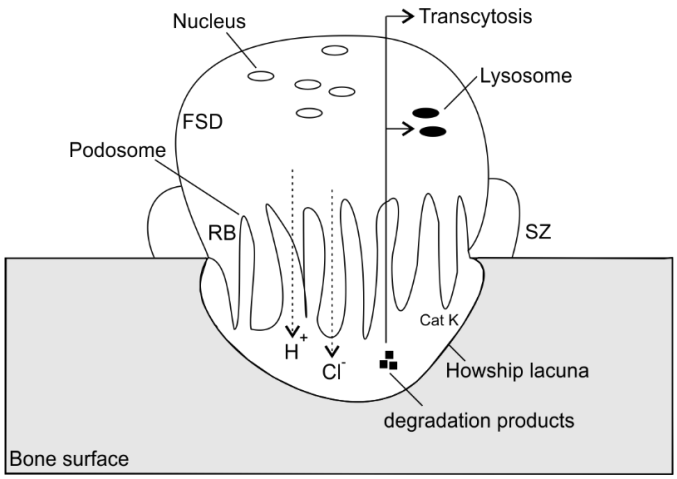

Figure 1-1 Bone resorption by an osteoclast. Schematic representation of a resorbing multinucleated osteoclast illustrating the sealing zone (SZ), ruffled border (RB) and the functional secretory domain (FSD). It resorbs the bone surface and forms a Howship lacuna by the secretion of ions (H^+ and Cl^-) and the proteolytic enzyme Cathepsin K (Cat K). The bone degradation products are phagocytosed by osteoclasts and either degraded by lysosomes or released into the blood stream by the process of transcytosis. *[Source: Figure adapted from the original in Basic and Applied Bone Biology, Editors David B.Burr, Mathew R. Allen]*

1.1.3 The bone remodeling cycle

The bone remodeling cycle **(Figure 1-2)** can be classified into five different stages, activation, resorption, reversal, formation and termination (Katsimbri, 2017). At the end of this physiological cycle, total bone volume does not alter, but the old bone get replaced by a newly formed one (Andersen *et al.,* 2009). This cycle is very crucial in maintaining the mechanical integrity of bones by replacing the old or damaged bone with a new healthier one. The cells responsible for bone remodeling *i.e.* osteoclasts and osteoblasts are arranged in a temporary anatomical cascade known as a basic multicellular unit (BMU) and the duration of the BMU is known as the bone remodeling period, which could last for several months.

1 **Activation:** It is the first stage of a cycle which involves the recruitment of osteoclast precursors to form fully functional multinucleated osteoclasts. The remodeling initiating signals either hormonal or mechanical are assessed by bone. Hormones such as parathyroid hormone (PTH) and estrogen released in response to systemic changes, mechanical stress and micro-damage to the skeleton, are considered as triggering signals to osteocytes (Bonewald, 2007). The PTH binds with PTH-receptors present on the surface of osteoblasts and stromal cells, which activates the expression of RANKL and M-CSF that are crucial for the differentiation and activation of osteoclasts (Juppner *et al.,* 1991).

2 **Resorption:** Mature multinucleated osteoclasts digest the bone by the combined action of proteolytic enzymes (Bouillon and Prodonova, 2000) and acid secretion (Kornak *et al.*, 2001). Functional osteoclasts secrete H^+ and Cl^- ions in a sealed vicinity, which lowers the pH to 4.5 to degrade the bony surface by dissolution, thus exposing them to the matrix metalloproteinase enzymes such as Cat K. The resultant pits are known as Howship lacunae (Lüllmann-Rauch, 2012). After resorption, osteoclasts undergo apoptosis thus terminating this phase (Katsimbri, 2017).

3 **Reversal:** It is the least well understood phase of the cycle and is described by the termination of resorption and initiation of a bone formation phase, which involves the recruitment of cells such as monocytes and pre-osteoblasts required for the bone formation (Everts *et al.,* 2002). The exact coupling signals that link the bone resorption and formation phases are not clear, however it is proposed that transforming growth factor-ß (TGF-ß) interferes with the production of RANKL by osteoblasts, thus inhibiting pre-osteoclasts from differentiating into functional cells; ultimately decreasing bone resorption (Katsimbri, 2017). Osteoclasts are then replaced by osteoblast-lineage cells to initiate the bone formation. Mononuclear cells present in the pre-formed cavities deposit mucopolysaccharide-rich material such as osteopontin that serves as a cement line between the new and old bone (Andersen *et al.,* 2013).

4 **Formation:** During this stage, osteoblasts lay down an unmineralized organic matrix called osteoid, primarily composed of type I collagen, which serves as a template to form mature bone after deposition of minerals over time. Some osteoblasts get buried within the newly formed osteoid also known as osteocytes. This phase lasts for several months (Katsimbri, 2017).

5 **Termination:** This is the final step of the remodeling cycle that involves the mineralization of osteoid and takes place over 90 and 130 days in the case of trabecular and cortical bones, respectively. It involves the deposition of hydroxyapatite crystals along with small amounts of acid phosphate, carbonate and magnesium. After mineralization, the bone enters into the resting or quiescent phase (Lind *et al.,* 1995).

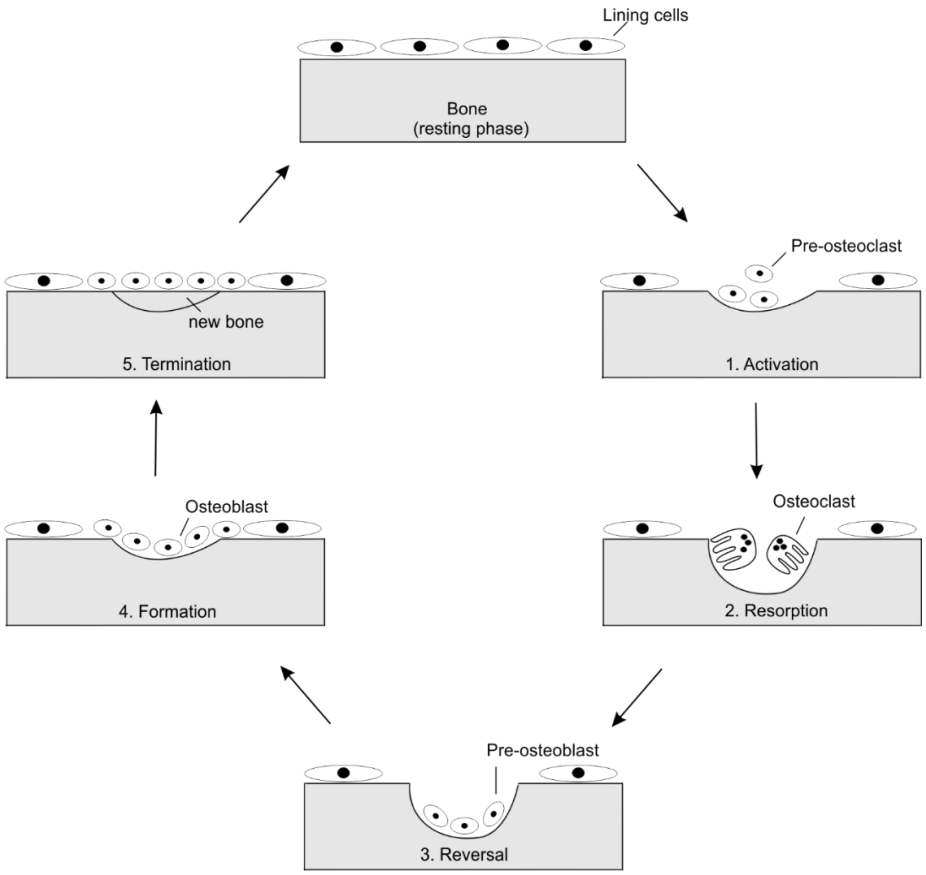

Figure 1-2 Bone remodeling cycle. A sequential schematic representation of five stages of the bone remodeling cycle is shown. Following microdamage or another trigger, a portion of bone in a resting phase enters into the first stage, **activation**, where pre-osteoclasts start accumulating over the surface of old bone followed by the second stage, **resorption**, polarized multi-nucleated osteoclasts engulf the bone and form resorption pits where pre-osteoblasts migrate to replace the osteoclasts in a **reversal** phase. In the fourth stage, **formation,** osteoblasts generate bone, and subsequently minerals (Ca^{2+},PO^{4+}) and hydroxyapatite crystals are deposited and a compact new bone is formed in the final stage, **termination**. The bone thus enters into the resting phase again. *[Source: Figure adapted from the original in* Agents Affecting Mineral Ion Homeostasis and Bone Turnover in *Goodman & Gilman's The Pharmacological Basis of Therapeutics*, 12th Edition]

1.1.4 Bone fracture

Bone fractures either due to severe mechanical traumas such as accidents, falls and sport injuries, or spontaneously in a disease state called osteoporosis. It causes anatomical discontinuity of a bone structure and inability to withstand mechanical load efficiently. Bone fractures can be broadly classified into two main types:

1. Open fracture: Along with bone, there is damage to surrounding soft tissue including skin and periosteum. Thus, there are higher risks of opportunistic infections.

2. Closed fracture: In this case, breaking of a bone occurs internally while the skin remains intact.

It is a common problem, which affects all age groups ranging from infants to elderly people. Over the recent years, incidence of osteoporotic or fragility fractures have become a serious issue worldwide. According to the International Osteoporosis Foundation (IFO), the annual number of osteoporotic fractures in the European Union (EU) will rise from 3.5 million in 2010 to 4.5 million in 2025, with an approximate incidence increase of 28% (Hernlund *et al.,* 2013). Therefore, new therapeutic advancements are in high demand to aid the fracture healing process.

1.1.4.1 Bone fracture healing

Bone fracture healing is a complex series of events where the bone heals without the formation of scar tissue. Although it is a natural process, various biophysical, biomechanical and pharmaceutical interventions may aid in rapid healing (Casanova *et al.,* 2014). Biophysical approaches such as ultrasound, shockwaves and electromagnetic field simulations help in bone anabolism or formation (Aaron *et al.,* 2006). Mechanical interventions include the usage of screws, metal plates *etc*. to stabilize the broken ends of a bone for proper healing (Histing *et al.,* 2011). The goal of medicaments is to accelerate the healing process and strengthening the callus tissue for the union of broken ends. The process of fracture healing can be divided into four different overlapping stages **(Figure 1-3)** (Schindeler *et al.,* 2008):

a. **Inflammation:** Excessive trauma leading to a bone fracture causes the disruption of the vascular supply and therefore a hypoxic condition arises in this region. Due to decreased local oxygen levels and nutrients, macrophages leucocytes and other inflammatory cells such as granulocytes, lymphocytes and monocytes migrate in this region to resist infections and also leads to the formation of a hematoma (Schindeler *et al.,* 2008). A wide range of cytokines and growth factors like transforming growth factor-ß (TGF-ß), platelet derived growth factor (PDGF), macrophage colony stimulating factor (M-CSF), bone morphogenetic proteins (BMPs) and tumor necrosis growth factor-α (TNF-α) are also secreted in this region (Einhorn, 1998), (Bolander, 1992). These factors cause the migration of multipotent mesenchymal stem cells which play a significant role in repair and subsequently bone formation (Shapiro, 2008). This process may last for seven days followed by the soft callus formation. At this stage, the

surrounding tissues and muscles mainly provide mechanical support to the broken structure.

b. **Soft callus (fibrocartilage) formation:** During this stage, the hematoma formed is replaced by a fibro-vascular tissue, which is rich in chondrocytes and fibroblasts (Schindeler *et al.,* 2008). Proliferation of chondrocytes and fibroblasts are stimulated by the coordinated activity of growth factors like TGF-ß, PDGF, insulin like growth factor (IGF) and BMPs (Gerstenfeld *et al.,* 2003), (Ai-Aql *et al.,* 2008). Chondrocytes and fibroblasts synthesize the cartilaginous matrix, mainly composed of collagen type II and fibrous tissue respectively to form a fibrocartilaginous, semi-rigid soft tissue between the broken ends to provide some mechanical stability (Barnes *et al.,* 1999). However, at this stage the callus cannot withstand any significant amount of load and is inclined to re-fracture when exposed to trauma. Cartilaginous callus is deprived of vascular system at this stage, which develops later in the woven bone. The soft callus serves as a template for bony callus formation at later stages.

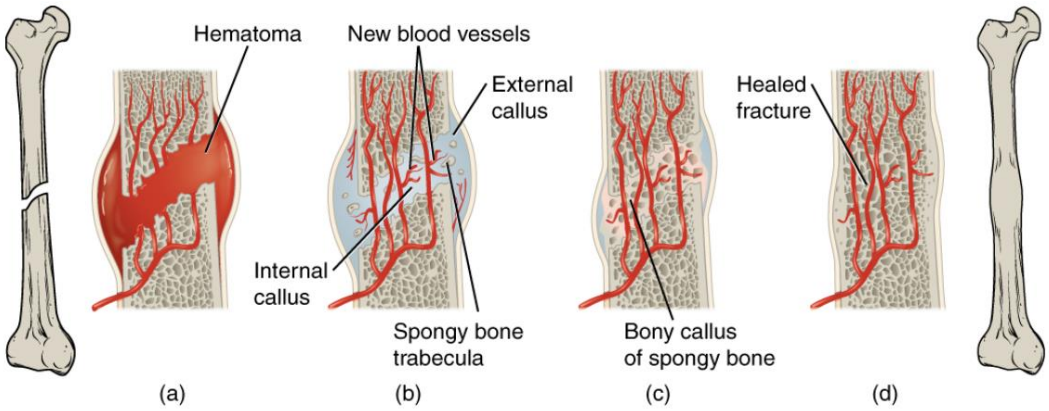

Figure 1-3 Stages of fracture healing. Schematic representation of overlapping stages of the bone healing process is shown. **(a)** Inflammation, upon fracture vascular supply disrupts and a hematoma is formed followed by **(b)** soft callus formation: periosteal (external) and endosteal (internal) soft calluses are formed, which serve as the template for **(c)** hard callus formation, osteoblasts generate spongy or woven bone having better biomechanical properties than soft callus and finally **(d)** remodeling: to convert the woven bone into a lamellar (healed) bone also known as bony callus by the combined activity of osteoclasts and osteoblasts. *[Source: Figure taken from Anatomy and Physiology by Rice University, author/publisher OpenStax, available online on BCCampus]*

c. **Hard callus formation:** This stage also known as primary bone formation and is the most active energy demanding stage of fracture repair and is characterized by a higher number of osteoblasts, as indicated by elevated osteoblast markers *e.g.* type I

collagen, alkaline phosphatase and osteocalcin in the bloodstream (Gerstenfeld *et al.,* 2003). Osteoprogenitors differentiate into osteoblasts, in the presence of certain osteogenic factors (Gerstenfeld *et al.,* 2003) and members of the BMP family (Chen *et al.,* 2004), (Nakase and Yoshikawa, 2006) generate woven bone matrix. The osteoprogenitors originate from variable sources such as from local surrounding tissues (Rumi *et al.,* 2005) or the circulation (Eghbali-Fatourechi *et al.,* 2005). The woven bone or hard callus has better mechanical stability compared to the fibrocartilage (Casanova *et al.,* 2014).

d. **Bone remodeling:** This is the final stage of fracture repair also known as secondary bone formation where the shape of bone and vascular system prior to fracture is restored (Gerstenfeld *et al.,* 2003). It is a similar to the remodeling procedure where osteoclasts and osteoblasts work in an organized fashion to maintain the bone integrity. Here lamellar bone replaces the woven or spongy bone and the mechanical strength is also restored.

1.1.4.2 Evaluation of fracture healing

Assessment of fracture healing is a very challenging task, as callus is a complex structure consisting of different type of cells and tissues that change over time. The extent and quality of fracture healing can be assessed by both structural and biomechanical evaluations. In animal models, structural evaluations involve both non-invasive methods like radiography, micro-magnetic resonance imaging (micro-MRI) and micro-computed tomography (µCT) (Morgan *et al.,* 2009) and invasive methods like histology (Epari *et al.,* 2010). Radiography is the most direct and robust way of analyzing the fracture of a bone. In the early stages of fracture healing, micro-MRI can be used to evaluate the quantity as well as the quality of fibrocartilage tissue. However, this method has a disadvantage that strong magnetic radiations interfere with the healing process itself (Casanova *et al.,* 2014). Over the last decade, µCT has emerged as a powerful tool to determine the callus microarchitecture. It not only provides information about the callus volume but also gives an estimation about the mechanical strength of the newly formed bone (Morgan *et al.,* 2009), (Shefelbine *et al.,* 2005). Most recently, Raman imaging and small-angle X-ray scattering (SAXS) have been used to evaluate the direction of collagen fibers, an indication of newly formed bone (bony callus) and resistance to re-fracture (Casanova *et al.,* 2014).

In biomechanical evaluations, varying degrees of load are applied to estimate the stress bearing capacity of a healed bone. *In vitro* three-point and four-point bending tests provide estimation of bending stiffness of fractured bones, an *in vivo* method especially suitable for long bones. Nanoindentation (Leong and Morgan, 2008) and scanning acoustic microscopy (SAM) (Eckardt and Hein, 2001) are also used for the assessment of callus biomechanical properties. In nanoindentation, a diamond tip is inserted into a specimen up to a certain depth and mechanical properties are estimated depending on the resistance of the tissue to the applied forces. In contrast, using SAM, mechanical properties or strength are estimated by the reflection of acoustic (sound) waves after hitting the callus tissue.

1.1.4.3 Micro-computed tomography (µCT)

The µCT enables to understand the bone microarchitecture by determining cortical and trabecular parameters, estimating the bone mineral density (Bouxsein *et al.,* 2010) and prediction of biomechanical properties of intact and fractured bones (Shefelbine *et al.,* 2005). It has become a valuable tool nowadays in the field of bone biology, which works on the principle of taking X-ray projected images of an object at different angles and mathematically converting them into 3-dimentional (3D) images.

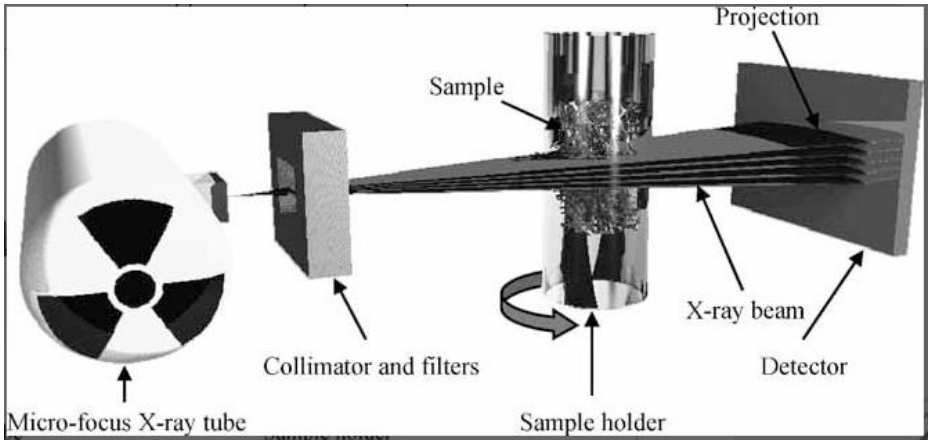

Figure 1-4 Basic operational principle of µCT scanning system. Schematic representation of a µCT scanner with all components is shown. An X-ray source emits radiation which passes through the filter to strike the object *i.e.* bone placed inside the sample holder rotating at an angle and subsequently projected X-rays are detected by the detector. The detector transfers the signal to an attached computer system to produce a resultant stack of 3D images using mathematical algorithms. [*Source: Guidelines for assessment of bone microstructure in rodents using micro-Computed Tomography; JBMR, Mary L Bouxsein et al. 2010,* with permission]

The bone is placed in an object holder and then X-rays emitted from a radiation source passes through a filter (aluminum or copper) and finally strike the rotating object. The resultant images fall on the detector attached to the computer that converts the stack of signals into 3D images by using mathematical algorithms. With the *in vitro* scanning system, the object is continuously moving at a defined angle while the X-ray source and detector remains stationary. Such systems are used for analysis for explanted organs such as femurs, teeth *etc*. In an *in vivo* scanning system, contrary to *in vitro* scanners the bone remains stationary while camera/detector revolves around the object used for imaging live animal models (Helfrich, 2012).

1.2 Transient Receptor Potential (TRP) channels

The TRP channels were first discovered in fruit-fly *Drosophila melanogaster* photoreceptors in which a spontaneous mutation caused a transient potential, instead of a sustained potential, upon steady light stimulation (Cosens and Manning, 1969). Twenty years later, the mutation responsible for this transient potential was identified by Montell and Rubin (Montell and Rubin, 1989) and the underlying gene dubbed "transient receptor potential" or "trp". Later in 1995, the first mammalian TRP cDNA *i.e.* TRPC1 was cloned (Zhu *et al.,* 1995), (Wes *et al.,* 1995). Since then TRP channels have been extensively studied to determine their potential role in mammalian physiology as well as pathology. The TRP cation channel family comprises of 28 mammalian (27 human) members and has been classified into six subfamilies based on their sequence similarities (Nilius and Owsianik, 2011). The six subfamilies include TRPC, where C stands for "canonical" which comprises of seven members *i.e.* TRPC1-C7, TRPV, with V for "vanilloid" comprises of six members *i.e.* TRPV1-V6, TRPM, with M for "melastatin" contains eight members *i.e.* TRPM1-M8, TRPP, with P for "polycystin" has three members namely TRPP2, TRPP3 and TRPP5, TRPML, with ML for "mucolipin" has also three members being TRPML1-ML3 and the last group TRPA has only one member TRPA1, with A for "ankyrin" **(Figure 1-5 a)**. All members of this superfamily share a similar characteristic of having six transmembrane domains (TM1-TM6) flanked by cytosolic N (amino) and C (carboxy) termini **(Figure 1-5 b)**. The cation permeable pore region of TRP proteins resides within the TM5-TM6 linkers. Four TRP proteins co-assemble to form a tetrameric channel. For example, TRPC4 can form homotetrameric TRPC4 channels or heterotetrameric TRPC4/TRPC1, TRPC5/TRPC1 or TRPC5/TRPC4/TRPC1 channels. The members within the subfamilies differ from each other

depending on their amino acid sequences and the length of the N and C termini (Nilius and Flockerzi, 2014a, b). The structures of more than ten TRP channel complexes have been solved by X-ray crystallography and cryo electron-microscopy (Cryo-EM) (Madej and Ziegler, 2018).

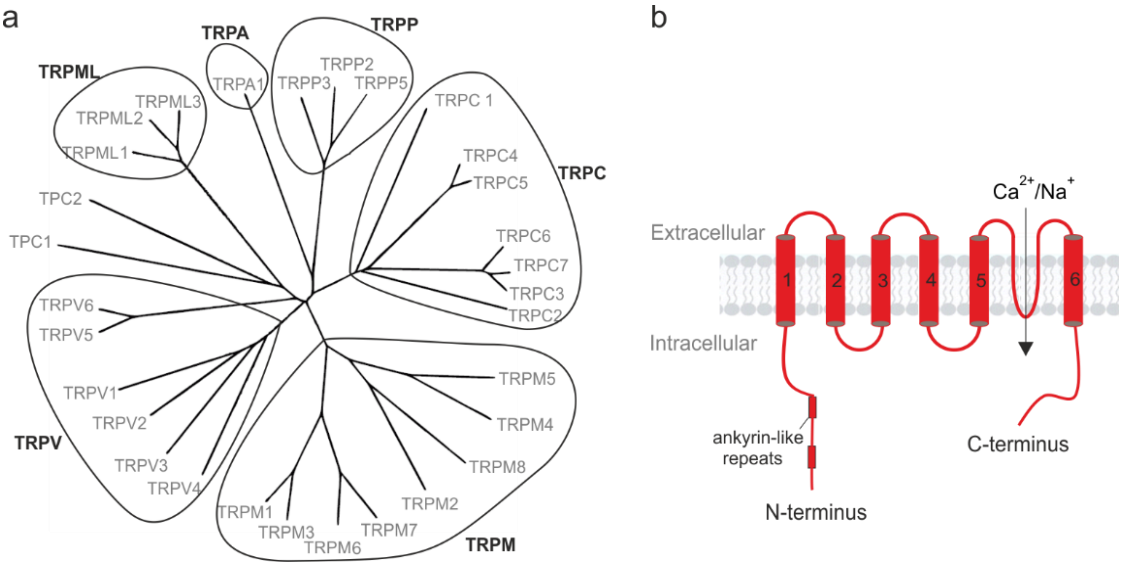

Figure 1-5 The Transient Receptor Potential (TRP) channel superfamily. (a) The classification of TRP channels into six subfamilies based on their amino acid sequence similarity *i.e.* TRPC (seven members, C1-C7), TRPM (eight members, M1-M8), TRPV (six members, V1-V6), TRPML (three members, ML1-ML3), TRPA (one member), TRPP (three members, P2-P3 and P5) and two pore channels (TPC1 and TPC2) are shown. **(b)** Scheme of a single TRP protein/subunit consisting of six transmembrane domains (1-6) flanked by cytoplasmic N-, C-termini, and the pore region permeable to cations (Ca^{2+} and Na^{+}) is present in between the transmembrane domains 5 and 6.

The majority of TRPs are known to act as non-selective cation channels, permeable to both Ca^{2+} and Na^{+} ions. Exceptions include TRPV5 and TRPV6, which are highly Ca^{2+} selective and TRPM4 and TRPM5 being highly Na^{+} selective (Nilius and Flockerzi, 2014a, b). The channels are activated by different mechanisms such as temperature change (heat or cold stimulus), pH change and by certain agonists and antagonists via secondary messengers (Freichel *et al.,* 2012).

1.2.1 Functional diversity of TRP channels

TRP-deficient mouse models have been generated by manipulating the *Trp* genes in embryonic stem (ES) cells using homologous recombination to identify their role in normal physiological as well as pathological conditions. They play a significant role from embryonic level to adulthood, in maintaining the normal physiological processes such as body

temperature, reproduction, metabolic and neuronal pathways, memory and taste perception (Nilius and Flockerzi, 2014a, b). For instance, *Trpm7* is of fundamental significance during embryonic development and *Trpm7*$^{-/-}$ embryos cannot survive more than eight days of embryogenesis (Jin *et al.*, 2012). Conversely, deletion at adulthood causes macrothrombocytopenia (Jin *et al.,* 2008). Studies have also shown lethal embryonic effects of the deletion of *Trpm6* (Walder *et al.,* 2009) and *Trpp2* (Wu *et al.,* 1998). *Trpc1*-deficient mice have shown increased body weight (Dietrich *et al.,* 2007 and own results) and decreased salivary secretions (Liu *et al.*, 2007). The significance of *Trpv6* in reproduction was determined by Weissgerber *et al.* in 2011, *i.e.* deletion of *Trpv6* leads to impaired male fertility and decreased Ca^{2+} absorption from intestine (Weissgerber *et al.,* 2012), (Weissgerber *et al.,* 2011). Other members of the TRPV family such as TRPV1 act as thermosensors and nocisensors, whereas TRPV4 is involved in maintenance of systemic osmoregulation as well as neuro-inflammation (Flockerzi and Nilius, 2007). *Trpm5* KO mouse models have shown reduced insulin secretion and thus elevated blood glucose levels (Brixel *et al.,* 2010), (Colsoul *et al.*, 2010). TRPA1 has been recognized as a sensor for the environmental stimuli such as cold, itch and pain (Nilius and Flockerzi, 2014a, b). Approximately 20 hereditary diseases in humans related to diverse fields such as cardiology, nephrology, pulmonology, urology *etc.* are linked to or caused by mutations of 12 *Trp* genes.

1.2.2 Transient Receptor Potential Canonical 1 (TRPC1)

The transient receptor potential canonical 1 (TRPC1) belongs to the subfamily of TRPC channels. *Trpc1* was the first mammalian *Trp* cDNA to be cloned (Wes *et al.,* 1995), (Zhu *et al.*, 1995) however the exact mechanism for the activation of this channel is still a matter of debate (Dietrich *et al.,* 2014). TRPC channels are activated following phospholipase C (PLC) stimulation by G_q-coupled receptors (G_qCR) or receptor tyrosine kinase (RTK) activation by certain agonists (Nilius and Flockerzi, 2014a, b). The *Trpc1* gene, which encodes TRPC1 protein, is located on chromosome 3 and 9 in the human and mouse genomes, respectively. The gene consists of 13 distinct exons while the initiation codon for the translation of the protein is present within exon one (Nilius and Flockerzi, 2014a, b). Until now, *Trpc1* reportedly translates into five different splice variants in humans and seven in rodents (mice) according to the Ensemble genome browser (http://www.ensembl.org/Mus_musculus/Info/Index).

The TRPC1 protein is predicted to have six transmembrane domains (TM1 to TM6) flanked by cytosolic C- and N-termini (Wes *et al.,* 1995), (Zhu *et al.*, 1995). In 2004, Dohke *et al.* postulated that TM5 and TM6 are involved in the formation of the ion conducting pore region of the channel (Dohke *et al.,* 2004). It also shows highest amino acid sequence similarity with the other members of its family like TRPC2, TRPC4 and TRPC5 (Flockerzi and Nilius, 2007). Although TRPC1 is the founding member of this superfamily, sufficient data to support that it could form a functional homomeric channel is still lacking. It interacts with other members of its subgroup such as TRPC4 and TRPC5 channel subunits to form heteromeric TRPC1/TRPC4, TRPC1/TRPC5 and TRPC1/TRPC4/TRPC5 channels (Broker-Lai *et al.*, 2017) For instance, co-expression of TRPC1 with TRPC4 or TRPC5 in HEK293 cells, leads to the formation of functional heterotetrameric channels as indicated by specific current-voltage (IV) relationship in comparison to the IV-relationship of homomeric TRPC5 channels (Beck *et al.*, 2017). It has also been shown that TRPC1 may interact with other proteins such as TRPV4, TRPV6 and TRPP2 (Nilius and Flockerzi, 2014a, b) and both ORAI and STIM proteins (Ambudkar, 2014).

Transcripts of *Trpc1* are expressed in many cells and tissues such as brain, heart, and kidney (Nilius and Flockerzi, 2014a, b) and it has been postulated that *Trpc1* gene is ubiquitously expressed throughout the body (Wes *et al.,* 1995), (Zhu *et al.*, 1995). This assumption is difficult to prove considering that there are no reliable ion currents detectable or suitable antibodies available. Dietrich *et al.* have generated *Trpc1*-deficient mice (Dietrich *et al.*, 2007). Most information about the physiological functions of TRPC1 derived from experiments performed on those *Trpc1*-deficient mice, which lack TRPC1 throughout the organism. Lack of TRPC1 has been associated with changes of cardiovascular, central nervous, skeletal and immune functions (Dietrich *et al.,* 2014). It has also been associated with pathologic conditions such as diabetic nephropathy (Zhang *et al.,* 2009), Parkinson's disease (Mattson, 2012), Darier-White disease (Pani and Singh, 2008) and Huntington's disease (Wu *et al.,* 2011).

1.2.3 Transient Receptor Potential Vanilloid 6 (TRPV6)

The TRPV6 channel belongs to the subfamily of TRPV channels, encoded by the gene *Trpv6* located on chromosomes 7q33-q34 and 6 in the human and mouse genomes respectively. The *Trpv6* gene contains 15 exons and 14 introns, which spans over a region of ≈15.7 kb (Hirnet *et al.*, 2003). According to the Ensemble genome browser, *Trpv6* has three splice variants to date (http://www.ensembl.org/Mus_musculus/Info/Index). The transcripts of *Trpv6* have been

detected in uterus, placenta, pancreas, prostate, parts of the digestive system (oesophagus, stomach, duodenum and colon) and kidney by RT-PCR and northern blot analyses in mouse tissues (Hirnet *et al.,* 2003), (Weissgerber *et al.,* 2011), (Lehen'kyi *et al.,* 2012). *Trpv6* transcripts along with transcripts of its closest relative *Trpv5,* have also been identified in human and mouse bone and osteoclasts. Nijenhuis *et al.* have shown the expression of *Trpv6* in bone marrow cells (Nijenhuis *et al.,* 2003). *Trpv6* mRNA has been also detected in murine syncytiotrophoblasts (Wissenbach *et al.,* 2001) and uterus (Moreau *et al.,* 2002).

TRPV6 and its closest relative TRPV5 are the only highly Ca^{2+}-selective channels in the TRP-superfamily (Peng *et al.,* 1999), (Wissenbach *et al.,* 2001). In normal physiological conditions, TRPV6 conducts only Ca^{2+} ions but in their absence it can also conducts monovalent cations like Na^{+} (Voets *et al.,* 2003), (Wissenbach *et al.,* 2001). TRPV6 proteins co-assemble to form homotetrameric channels (Saotome *et al.*, 2016) while heterotetrameric TRPV5/TRPV6 channels might occur after heterologous expression of TRPV6/TRPV5 cRNAs in oocytes (Hoenderop *et al.,* 2003). TRPV6 also shows interaction with other proteins such as TRPC1 (Schindl *et al.,* 2012), (Courjaret et al., 2013) and calmodulin (Niemeyer *et al.*, 2001). TRPV6 becomes inactivated by various compounds such as Xestospongin C (Vassilev *et al.,* 2001), Ruthenium red and certain anti-fungal drugs like econazole and miconazole (Hoenderop *et al.,* 2001).

As for many other TRP proteins, the information about the physiological functions of TRPV6 has been gathered mainly from *Trpv6*-deficient (Bianco *et al.,* 2007) (Weissgerber *et al.,* 2011) or *Trpv6*-mutant mouse lines (Weissgerber *et al.,* 2012). Mice lacking functional TRPV6 are viable but they have shown compromised body weight and reduced femoral length and mineral density (Bianco *et al.,* 2007) as well as decreased fertility (Weissgerber *et al.,* 2012), (Weissgerber *et al.,* 2011). In 2011, van der Eerden *et al.* showed reduced cortical and endocortical volume in *Trpv6* mutated mice compared to wild-type animals. The role of TRPV6 channel in prostate, breast, colon, ovarian, and thyroid gland cancers has been extensively studied by various research groups (Nilius and Flockerzi, 2014a, b). *Trpv6* transcripts are overexpressed in prostate cancer (Wissenbach *et al.,* 2001) as well as breast cancer (Lehen'kyi *et al.,* 2012) and the expression pattern correlates with the severity of the disease; especially in case of prostate cancer (Wissenbach *et al.,* 2001). These studies clearly demonstrate the

significance of *Trpv6* in carcinogenesis and might serve as a suitable marker for detection as well as a potential therapeutic target.

1.3 Targeted modification of TRP channel genes

Gene deficient mouse models have contributed significantly in understanding the functional significance of TRP channels (Flockerzi and Nilius, 2007). The classical way is to replace the chromosomal regions by targeted homologous recombination and thereby the gene of interest either can be disrupted to obtain classical/constitutive "knockout" or modified by the insertion of additional gene cassettes comprising of fluorescent reporter genes to obtain "knock-in" mouse models (Joyner, 2005).

1.3.1 Classical gene targeting

Constitutive knockout mouse models have been widely used for the functional characterization of TRP channels such as *Trpc1*$^{-/-}$ (Dietrich *et al.*, 2007) and *Trpv6*$^{-/-}$ (Weissgerber *et al.,* 2011) mouse models. This approach has several limitations such as potential embryonic lethality, if the gene of interest such as *Trpm6* (transient receptor potential melastatin 6) or *Trpm7* being essential for embryogenesis is ablated: The embryos mostly die at embryonic day 12.5 (Walder *et al.,* 2009). Another drawback especially associated with the widely expressed genes, is the determination of cell- or organ-specific role of them, since it is almost impossible to distinguish cell-autonomous effects from effects resulting from other tissues or organs.

1.3.2 Conditional gene targeting

Conditional gene targeting describes a type of gene targeting where manipulation of a particular gene of interest is carried out in a defined population of cells or in an organ at a specific time-point, using a cell-specific recombinase system (Joyner, 2005), (Albert *et al.,* 1995).

Cre-*loxP* and Flp-*FRT* are the two types of site-specific recombinase systems mostly used for generating conditional gene targeting (Joyner, 2005). The Cre-*loxP* system, derived from bacteriophage P1, is a robust system that requires three components for functioning: Cre recombinase, *loxP* target sites and mono/di-valent ions. No additional cofactors and accessory proteins are required (Nagy, 2000), (Lobe *et al.,* 1999). Cre-recombinase belongs to λ integrase

superfamily that cleaves the DNA segment flanked by *loxP* sites. The target site for the Cre enzyme is *loxP* or "locus of crossing over x at bacteriophage P1" (Sternberg *et al.,* 1981). A *lox P* site comprises of 34 base pairs with an eight bp non-palindromic core region flanked by a 13 bp palindromic region. The *loxP* site is commonly represented by a triangle and the direction of the triangle depicts the outcome of the recombination reaction like deletion (floxing a gene), inversion and translocation of that specific DNA sequence (Hoess *et al.,* 1982), **(Figure 1-6)**. The Flp-*FRT* system is analogous to the Cre-*loxP* system.

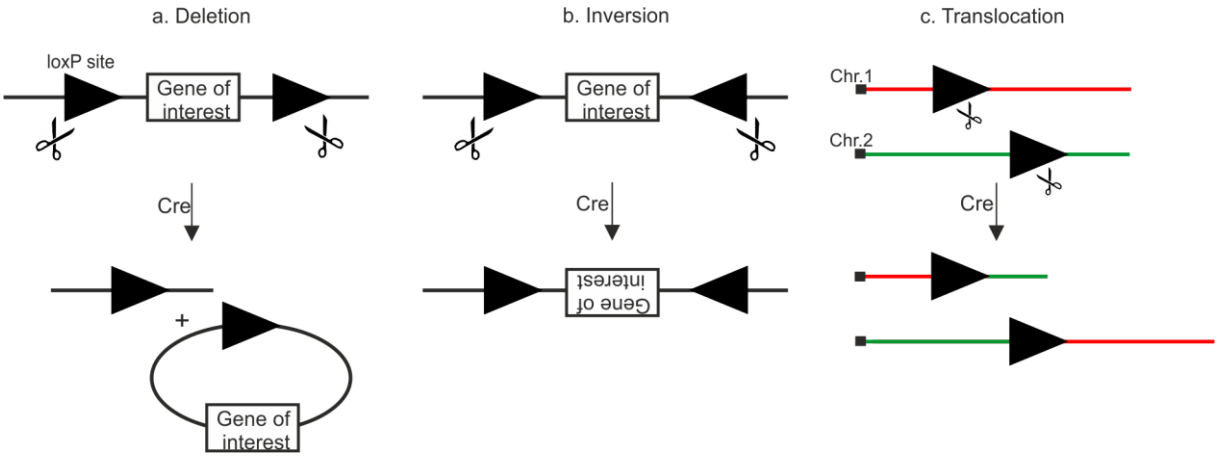

Figure 1-6 The Cre-*loxP* recombinase system. Schematic representation of DNA recombinations *i.e.* **(a)** deletion, **(b)** inversion and **(c)** translocation of a gene of interest between heterologous chromosomes upon Cre mediated excision, (black triangle depicts *loxP* site), Cre, Cre recombinase.

Aims of study

1. TRPC1 and TRPV6 proteins are expressed in bone cells but the exact role of these proteins in bone homeostasis and fracture healing is not known. The first aim was to establish µCT for the precise determination of cortical trabecular and callus parameters of bone. Using this method, I wanted to elucidate the role of TRPC1 and TRPV6 in bone microarchitecture using *Trpc1* or *Trpv6* gene-deficient and *Trpc1*/*Trpv6* double mutant mouse strains. Additionally, I correlated the µCT results with biomechanical properties of *Trpc1* or *Trpv6* gene-deficient bones using three-point bending tests. At the cellular level, I compared *in vitro* osteoclasts differentiation between *Trpc1*-deficient and wild-type mice.

2. As the cellular expression of *Trpc1* is hard to analyze due to missing appropriate antibodies for immunohistochemistry it is still an open debate where exactly TRPC1 proteins occur in mice. Therefore, the second aim was the generation of a *Trpc1*-IRES-Cre mouse line where Cre recombinase is present in all *Trpc1* expressing cells. After crossing with reporter mouse strains such as eRosa26-τGFP, *Trpc1*-positive cells are easily detectable by their fluorescence. This mouse line will help to visualize and to analyze the expression of *Trpc1* in bone as well as all over the mouse body.

3. The TRPC1 protein seems to be present in different bone cells such as osteoclasts and osteoblasts. Using global *Trpc1*-deficient mice, it is difficult to rule out the role of *Trpc1* specifically in bone, as one cannot exclude any interfering effects from the TRPC1 present in other cells or organs. To attribute a phenotype to a certain cell type it is necessary to use a conditional knockout mouse strain. Therefore, the third aim of my doctoral research was the generation of a conditional *Trpc1*–flox mouse strain. After crossing these mice with a cell-specific Cre mouse strain, it will be possible to determine TRPC1 function in the desired cell type or organ.

2 Materials and Methods

2.1 Bone analyses

2.1.1 General materials

Experiment	Materials	Supplier (catalog number)
Primary osteoclasts culture	α-MEM (Minimal Essential Medium)	gibco by Life Technologies (22561-021)
	FBS	gibco by Life Technologies (10270-106)
	Heparin (Heparin-Natrium) 5000 iE/mL	Braun GmbH
	Antibiotic antimycotic solution	Sigma-Aldrich (A5955)
	Recombinant Mouse M-CSF	R&D systems (416-ML-010)
	Recombinant Mouse TRANCE/TNFSF11/RANK L	R&D systems (462-TEC-010)
	TRACP & ALP double stain kit	TaKaRa Bio Inc. (MK300)
	Bovine Serum Albumin	Sigma-Aldrich (A4503)
	Osteo Assay Stripwell plate	Corning Inc. (3989)
Fracture model	Surgical instruments	Fine Science Tools GmbH, Heidelberg
	Tungsten guide wire (0.2 mm)	RISystem (RIS.521.100)
	Mouse screw	RISystem (RIS.221.100)
	Hand-drill 2-1mm	RISystem (RIS.390.130)
	Square box wrench 0.50 mm	RISystem (RIS. 590.111)
	Suture (Surgicryl) 3/8 circle	Smi (11151519)
	asid-med, hair removing cream	Aisd-Bonz (NDXZ10)
	Dexpanthenol 5% (BEPANTHEN®)	Bayer (3400935940179)
	Carprofen 50 mg/mL (RIMADYL®)	Zoetis Inc.
	Ketaminhydrochlorid 100 mg/mL (URSOTAMIN®)	Serumwerk Bernburg AG
	Xylazinhydrochlorid 23.32 mg/mL 2% (ROMPUM®)	Bayer
	0.9% NaCl	B.Braun
	Glucose 5%	B.Braun

2.1.2 Mice

All animal experiments have been reviewed and approved by the responsible authority, the local ethics committee of the Saarland. We abide by the 3R principle (replacement, reduction, refinement). Four independent mouse strains were used in the bone related experiments: Wild-type, *Trpc1*$^{-/-}$ (Dietrich *et al.,* 2007), *Trpv6*$^{mt/mt}$ (Weissgerber *et al.,* 2012) and double

mutant mice *i.e.* *Trpc1*$^{-/-}$/*Trpv6*$^{mt/mt}$ (generated by breeding of *Trpc1*$^{-/-}$ and *Trpv6*$^{mt/mt}$ mice). To get mice of a defined mixed genetic background all of the above mentioned genotypes were obtained by specific breeding of a 129SvJ with a C57BL/6 mouse. The resulting pups, the F1 generation were used for all experiments as "mixed" (129SvJ/C57BL/6). Mice were under a 12 h light/dark cycle with food and water *ad libitum*. All animals had the same genetic background *i.e*. mixed strain (129SvJ/C57BL/6). Only male mice were used in experiments at ages ranging from 2 to 24 weeks.

2.1.3 Methods

2.1.3.1 Primary osteoclast culture

The primary osteoclasts culture protocol was established in our laboratory by modifying the original method published by van der Eerden *et al.* (van der Eerden et al., 2005). Mice were sacrificed by cervical dislocation and bones (femurs and tibiae) were freed from muscles and surrounding soft tissues. Bones were cut at the distal end to make an opening, fixed within a small piece of microfluidic tubing and finally placed in a 1.5 mL eppendorf tube containing 250 µL mouse osteoclast culture (MOC) medium. The composition of MOC medium: Minimum essential medium with nucleosides (alpha-MEM) supplemented with 10% FBS, 170 IE/mL heparin. Hundred U/mL penicillin, 100 µg/mL streptomycin, 250 ng/mL amphotericin B were added as antibiotic/antimycotic solution. The tubes were centrifuged at 4500 rpm for 3 min to thoroughly flush out the bone marrow cells. The cell pellet was re-suspended in 750 µL medium and transferred to a Falcon tube containing 9 mL culture medium. The cells were centrifuged at 4°C for 5 min at 410 g followed by resuspension of the pellet in 1 mL medium and 9 mL lysis buffer and subsequent incubation for 5 min at 21°C. Thereafter, cells were centrifuged at 410 g for 5 min at 4°C and the cell pellet was washed (220 g for 5 min) twice with 5 mL MOC medium. Finally, the cells were counted using Neubauer's chamber (Blau Brand) and seeded at a concentration of $1x10^5$ cells per well (total volume per well was 150 µL) in an Osteo Assay Stripwell plate in the presence of 30 ng/mL M-CSF and 20 ng/mL RANKL. Every 2-3 days, approximately two-thirds of culture medium was replaced by freshly prepared MOC medium containing both growth factors and 85 µL of 6N HCl/50 mL medium. Eight days later, culture medium was aspirated and attached cells were washed once with 1xPBS (Sigma-Aldrich) and stained for tartrate-resistant acid phosphatase (TRAP) activity as per manufacturer's instructions (TaKaRa). TRAP served as a marker for osteoclasts. The von Kossa

staining was performed to determine the resorption capability of osteoclasts after visualizing the pits and trails formed.

For using the TRACP & ALP double stain kit, cells were fixed by adding 50 µL fixation solution (provided by the manufacturer) to each well and incubated for 5 min at 21°C. Wells were washed twice with deionized water and then TRAP solution was added containing 0.1 volume of sodium tartrate as per manufacturer's guidelines. The wells were incubated for 40 min at 37°C for the enzymatic reaction to take place. The enzymatic activity was stopped by adding deionized water and subsequently wells were washed three times with the deionized water. TRACP-positive red/pink colored cells, containing more than three nuclei were considered as mature osteoclasts. Those cells were counted manually using a microscope (Zeiss Axiovert 40 CFL, Carl Zeiss AG) at a magnification of 10x and in parallel representative images were taken by a camera (Zeiss AxioCam MRC5, Carl Zeiss AG).

For von Kossa staining, all reagents were prepared fresh prior to use. The culture medium was removed and wells were washed three times with deionized water followed by incubation for 30 min with 5% $AgNO_3$ in bright light. The wells were washed three times with deionized water and incubated for 2 min with 5% Na_2CO_3 (in 25% formalin). The reaction was stopped by washing three times with deionized water and subsequently 5% $Na_2S_2O_3$ was added for two minutes. At the end, the wells were washed again three times with deionized water and observed with a microscope (Zeiss Stemi 2000-C, Carl Zeiss AG) at a magnification of 1.6x and in parallel representative images were taken by a camera (Zeiss AxioCam MRC5, Carl Zeiss AG). The unstained surface (resorbed areas) was quantified using ImageJ (Version 1.51f) available online.

2.1.3.2 RT-PCR from crushed bone and bone cells

Total RNA from the crushed femurs and *in vitro* cultured osteoclasts and osteoblasts was isolated using the RNeasy Micro Kit (Qiagen). Total RNA (0.5 µg) was reverse transcribed using the Maxima first strand cDNA synthesis kit (ThermoFisher Scientific) as per the manufacturer's guidelines. One µL of cDNA was used in RT-PCR reaction for the detection of *Trpc1* transcripts using a primer set (Forward primer: 5'-TGCAAACGTTCTGAGTTACC-3' and a reverse primer: 5'-GGTTGTGATTGTGCTGACG-3') covering sequences from exons 9 to11. The composition of reaction mixture:

Component (reagent)	Quantity (µL)	Final concentration
First strand (cDNA)	1	variable
5x Phusion buffer HF	5	1x
10 mM dNTP's	0.5	200 µM
2U/µL DNA polymerase	0.5	1 U
10 µM forward primer	1.5	0.5 µM
10 µM reverse primer	1.5	0.5 µM
Deionized H_2O	ad 25	

RT-PCR conditions were as follows: initial denaturation for 30 s at 98°C, 35 amplification cycles (10 s at 98°C, 20 s at 64°C, 15 s at 72°C), and a final extension for 5 min at 72°C using a phusion high fidelity polymerase (ThermoFisher scientific) in a 25 µL reaction volume. The resultant product was loaded onto a 2% agarose standard gel (Roth) and separated by electrophoresis along with a GeneRuler 1Kb plus DNA ladder as marker (ThermoFisher scientific) to estimate the size of the amplified DNAs.

2.1.3.3 Fracture model

All mice used in this experiment were handled with great care according to the animal welfare and ethical norms. The surgical procedure as described by Herath and coworkers (Herath *et al.,* 2015) was approved by the responsible authority of the Saarland. Twenty-week-old male mice were weighed and anesthetized by administering 100 mg/kg body weight (BW) ketamine and 10 mg/kg BW xylazine intraperitoneally. Under aseptic conditions, a 5 mm medial parapatellar incision was performed on the right knee to dislocate the patella laterally. After drilling a 0.5 mm diameter hole into the intercondylar notch, an injection needle (27G $^{3/4''}$, 0.4x19 mm) was inserted through the intramedullary canal followed by a 0.2 mm tungsten guidewire coming out from the proximal side of the femur. A simple, transverse mid-shaft fracture (according to AO classification) was produced using a blunt guillotine. A weight of 80 g was dropped from a height of 100 mm in the middle of femoral shaft and afterwards the broken ends were stabilized using a 17.2 mm stainless steel mouse screw (RISystem). Wound closure was carried out using 4-0 synthetic absorbable sutures. Bone fracture and subsequent screw implantation was controlled at various steps by radiography (MX-20, Faxitron X-ray Corp., Wheeling, IL, USA) **(Figure 2-1)**. Five mg/kg BW carprofen was injected subcutaneously prior to the surgical procedure and the following day. Carprofen is a nonsteroidal anti-inflammatory and analgesic drug. All animals were housed in separate cages with *ad libitum* excess to food and water and a standard cycle of 12 h of light and dark each for four weeks.

Wound status was carefully monitored daily during the first week and then once per week until four weeks.

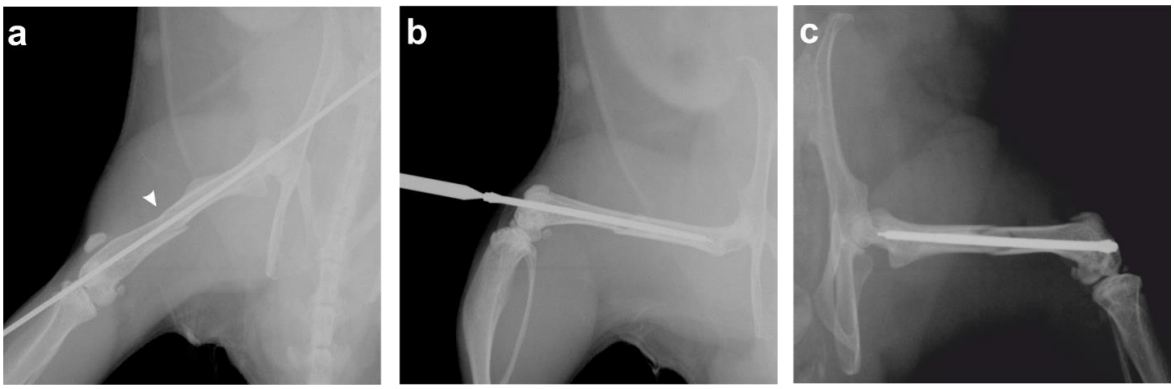

Figure 2-1 Fracture model at surgery day. Representative X-ray images taken at three different steps of surgical procedure at day zero: **(a)** Arrow-head indicates the fracture site and a guidewire passing through the bone; **(b)** insertion of a screw following a guidewire to hold the broken ends and **(c)** fractured femur stabilized by a screw.

After four weeks, mice were weighed again and wound status, activity, and gait pattern was carefully examined. The mice were sacrificed by cervical dislocation and an X-ray image of the broken bone was taken for the preliminary estimation of bone healing **(Figure 2-2)**. Afterwards, both healthy and fractured femora were removed and freed from muscles and surrounding tissue. The screw was explanted using a square box wrench. Biomechanical testing was performed by a non-destructive three-point bending test. Finally, bones were wrapped in a 0.9% NaCl soaked gauze or wet tissue paper and preserved at -80°C for callus analysis by µCT.

Figure 2-2 Fracture model after 27 days. Representative X-ray image taken at day 28 after fracture, arrow-head shows broken ends joined together by the callus formation.

2.1.3.4 Bone biomechanics

The femurs were mounted on a three-point bending device (Mini Zwick Z 2.5, Zwick GmbH) for estimation of the bending stiffness (N/mm) using a non-destructive bending test. The protocol followed the procedure described by Herath and coworkers (Herath *et al.,* 2015). The bones were placed horizontally on two lower posts 6 mm apart, with the condyles facing upwards. A gradually increasing load at a rate of 1 mm/min was applied in the middle of the femoral shaft by the upper post **(Figure 2-3)** and displacement plotted versus applied load (N) was displayed using the software testXpert V12.0 on a computer system attached with a three-point bending device. The application of force was manually stopped as soon as the displacement curve deviated slightly from the linearity. Finally, bones were wrapped within 0.9% NaCl soaked gauze and frozen at -80°C for µCT analysis. The bending stiffness ($\Delta L/\Delta D$) (N/mm) was calculated as the slope of the linear portion of the load versus displacement curve:

Bending stiffness (N/mm) = y_2-y_1/x_2-x_1, where Δx (x_2-x_1) is the displacement (D) in mm and Δy (y_2-y_1) is the load (force) applied in Newton, N.

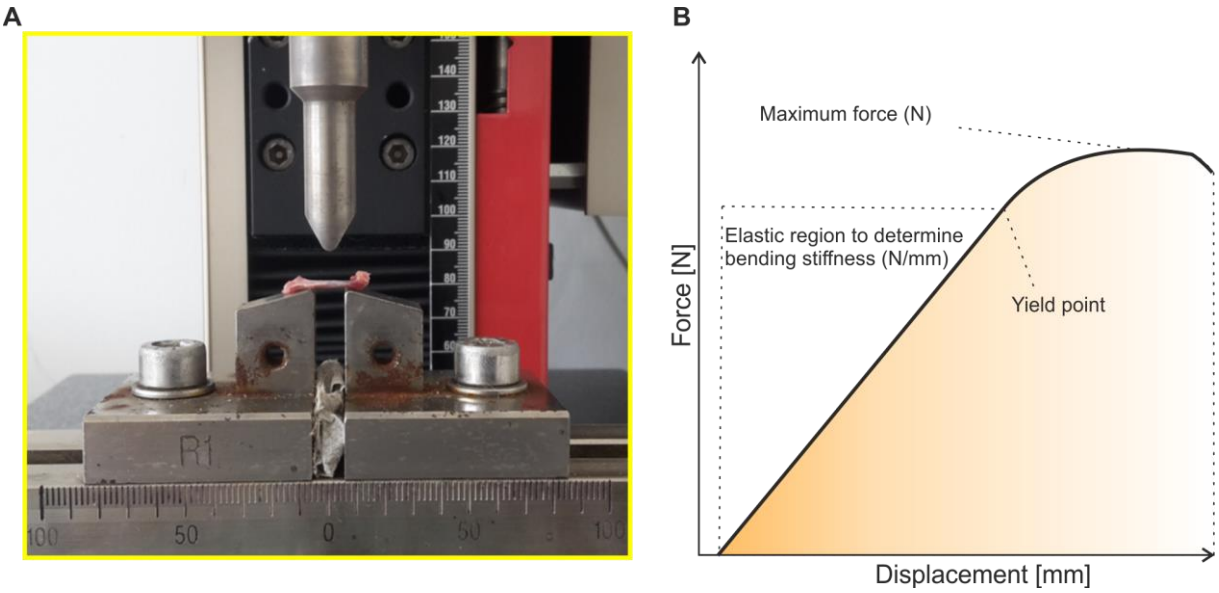

Figure 2-3 Biomechanical testing. **(A)** The three-point bending device (Mini Zwick Z 2.5) is shown with a femur lying horizontally on two lower posts 6 mm apart while a force is applied vertically from the upper post. The image is taken of the instrument (Mini Zwick Z 2.5) that is present in the Institut für Klinisch-Experimentelle Chirurgie, Universität des Saarlandes, Homburg. **(B)** Load/force-displacement curve.

2.1.3.5 Bone analysis by µCT

Intact/healthy and fractured femurs from male mice were removed and thoroughly cleaned from the surrounding muscles. All bones were scanned at a resolution of 6.5 µm using a high resolution scanning system SkyScan 1172 µCT (Bruker MicroCT, Kontisch, Belgium). The bones were wrapped in a wet tissue paper, placed in a plastic holder and mounted vertically in the sample chamber for imaging. The scanning conditions were adjusted according to the previously published guidelines by M. L. Bouxsein (Bouxsein *et al.,* 2010). X-ray source voltage and current were 50 kV and 200 µA, respectively. Beam hardening was reduced using a 0.5 mm aluminum filter. The exposure time was five seconds and scanning angular rotation was set to 180° with an increment of 0.4 rotation step (deg). NRecon (version 1.6.10.6) software was used to reconstruct the images while other software such as DataViewer (1.5.1.2) and CtAn (1.16.4.1+) were used for bone analysis (all provided by Bruker MicroCT).

Projection images obtained after scanning the bone samples were converted into tomographic cross-sectional images using NRecon software. All datasets were reconstructed under the same conditions. Misalignment compensation was always used as automatically estimated by the software and smoothing and ring artifact reduction were set at levels 2 and 5, respectively. A 20% correction in beam hardening was performed to sharpen the resultant cross-sectional images. After reconstruction, 3D femurs were oriented in the desired direction using a software DataViewer.

DataViewer was used to direct the reconstructed cross-sections of a dataset in a fixed/defined orientation for consistent analysis of the individual bones. By comparing three different views *i.e.* coronal, transaxial and sagittal views, displayed in DataViewer, the bone dataset was oriented in an upright position displayed in the coronal view keeping the femoral head upwards while in a transaxial view, the intersecting lines were kept exactly in the middle of the growth-plate cross-section **(Figure 2-4)**. In this way, all samples have similar orientations, which is important for selecting a similar volume of interest (VOI) for cortical and trabecular analysis of each bone using CtAn software.

Figure 2-4 Orientation of a 3D femur using a DataViewer software. Representative images depict three different views of a reconstructed 3D femur dataset *i.e.* coronal, transaxial and sagittal views. 3D femur appears straight with a femoral head on the top in a coronal view. In a transaxial view, the representative cross-section is oriented so that the intersecting lines are exactly in the middle of four semi-circular islands.

After orientation, the dataset was uploaded in CtAn software to determine the bone parameters. For determining the cortical and trabecular parameters, the first step was to determine the volume of interest (VOI) for both cortical and trabecular bone analyses (Bouxsein *et al.,* 2010). The center of the femoral shaft was used as a reference for selecting cortical bone VOI, whereas the trabecular bone VOI was selected with reference to the growth plate (van der Eerden *et al.,* 2012) **(Figure 2-5)**.

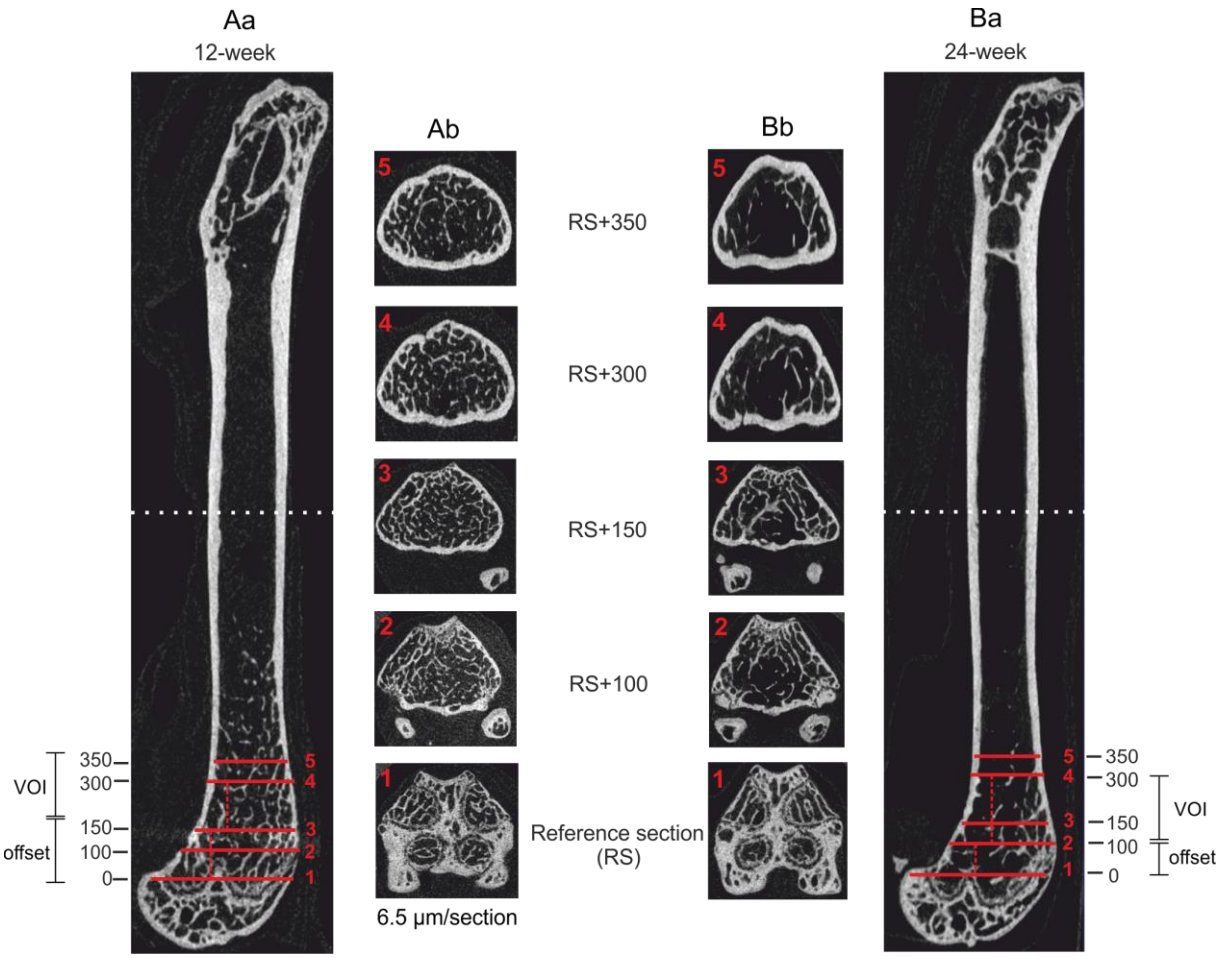

Figure 2-5 Selection of volume of interest (VOI) for cortical and trabecular analysis of femurs from 12- (left panel) and 24-week- (right panel) old mice. (Aa, Ba) For cortical bone analysis, the central dotted white line in the femoral shaft is considered as a reference, 25 cross-sections (6.5 µm each) are analyzed above and below this reference to determine the cortical bone parameters. For trabecular bone analysis, the reference for defining VOI is adapted according to the original method defined in the Bruker-microCT application note (Micro-CT analysis of mouse long bones (proximal tibia, distal femur)) as follows: Moving slice-by-slice towards the growth plate from the condyles, a point is reached where a clear "bridge" of low density cartilage (chondrocyte seam) is established from one corner of the cross-section to another. As soon as this bridge starts to disappear, that particular cross-section is taken as a landmark. This landmark defines the reference section, RS, at position 0, (indicated as 1, in red), trabecular VOI is then defined relative to this reference section, at section 100 (RS+100, 2), 150 (RS+150, 3), 300 (RS+300, 4) and 350 (RS+350, 5) **(Ab, Bb)**. For 12-week-old mice, sections between 1 and 3 are considered as offset (150 cross-sections), while VOI lies within the sections 3 and 5 (150 cross-sections). For 24-week-old mice, sections between 1 and 2 are taken as offset (100 cross-sections), while VOI consists of the sections 2 and 4 (200 cross-sections) as indicated by red lines and the corresponding cross-section.

For the cortical bone analysis, the reference was selected exactly in the middle of the femur shaft by dividing the total number of cross-sections by two and then twenty-five cross-sections above and below this reference were taken as VOI. A total of fifty cross-sections of 6.5 µm each were analyzed to determine the cortical bone parameters such as cortical bone volume (BV), endocortical volume (Ec.V), cross-sectional thickness (Cs.Th), and perimeter using a special tasklist **(**supplementary **Table 6-1)** in the supplement. Cortical tissue mineral density (TMD) was estimated using calcium hydroxyapaptite (CaHA) phantoms of known densities *i.e.* 0.25 and 0.75 g/cm^3 (Bouxsein *et al.,* 2010) following a Bruker-microCT method note (Bone mineral density (BMD) and tissue mineral density (TMD) calibration and measurement by micro-CT using Bruker-MicroCT CT-Analyser) and a special tasklist **(**supplementary **Table 6-2)** in the supplement.

For the trabecular bone analysis, the cross-section where the chondrocyte seam, a low density cartilage 'bridge', separating the four islands started to disappear was selected as a reference section or landmark **(Figure 2-5)**. Moving away from this landmark towards the diaphysis, the region including the growth plate and primary spongiosa in the metaphysis was excluded as offset **(Figure 2-5)**. Selection of an appropriate VOI for the trabecular bone analyses in mouse femur bone is crucial, because trabecular region is located adjacent to the metaphyseal growth plate. Selecting a VOI too close to the growth plate will cause contamination of primary spongiosa or extending too far from the growth plate will leads to the inclusion of empty spaces *i.e*. tissue volume, subsequently reducing the bone volume fraction (BV/TV). Moreover, trabecular bone is constantly changing with age, which highlights the need of selecting appropriate trabecular bone VOI depending on the age of mice being analyzed. A total number of 150 and 200 cross-sections in the region of the secondary or mature spongiosa for 12- and 24-week-old mice respectively were used to determine trabecular bone parameters using a special tasklist **(**supplementary **Table 6-3)** in the supplement. These parameters include trabecular number (Tb.N), trabecular thickness (Tb.Th), trabecular separation (Tb.Sp) and trabecular pattern factor (Tb.Pf). Trabecular separation is the mean distance between the trabeculae whereas trabecular pattern factor is inverse index of connectivity between the trabeculae. Trabecular bone mineral density (BMD) (includes both bony- and non-bony-voxels) was also estimated by comparing the dataset with CaHA phantoms in a similar fashion as tissue mineral density, however a separate tasklist was used **(**supplementary **Table 6-4)** in the supplement. Two different threshold ranges *i.e.* 120-255 and 80-255, estimated by the

Otsu method of thresholding (Manual for Bruker-microCT CT-Analyser v.1.13, The user's guide), were utilized for cortical and trabecular bone analyses, respectively. All four tasklists were modified from the original that were kindly provided by Dr. Bram van der Eerden, Erasmus Medical Centre, Rotterdam.

For the callus tissue analysis, the steps such as scanning, reconstruction and orientation of fractured femur bones were performed exactly in the same aforementioned manner. After loading the dataset in CtAn, the VOI was selected based on the presence of callus tissue. The VOI contained all cross-sections comprising the callus tissue *i.e.* newly formed tissue (bone) surrounding the fracture site. For ROI selection, endosteal and periosteal callus region was manually selected by eliminating the cortical bone from the surrounding callus tissue (Casanova *et al.,* 2016). **(Figure 2-6)**. Total callus volume, volume of low and highly mineralized bony callus were determined using various threshold values such as 68-255 (total volume), 68-97 (low mineralized callus) and 98-255 (highly mineralized callus) respectively (Bosemark *et al.,* 2013), (Orth *et al.,* 2017). As callus is a newly formed bone tissue, trabecular parameters such as Tb.N, Tb.Th, Tb.Sp and Tb.Pf were determined to estimate the callus microarchitecture (Casanova *et al.,* 2016), (Kondo *et al.,* 2015) using an independent tasklist **(**supplementary **Table 6-5)** in the supplement. This special tasklist for callus analysis modified from the original that was kindly provided by Dr. Robert Tower (MacKay Orthopedic Research Laboratory, Perelman, School of Medicine, University of Pennsylvania, USA).

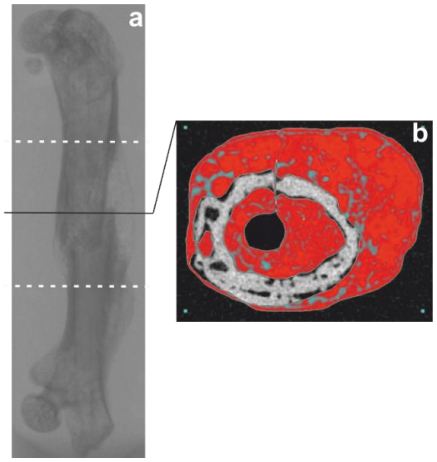

Figure 2-6 Selection of VOI and ROI for callus analysis. (a) Representative X-ray image shows the explanted fractured femur after removal of the screw; two dotted lines indicate the VOI *i.e.* all cross-sections containing the callus tissue while the central line represents **(b)** a cross-sectional image (6.5 µm) wherein periosteal and endosteal callus 'ROI' has been selected manually (highlighted in red color) delineating the cortical bone (grey) for callus analysis.

2.2 Targeted modification of the mouse *Trpc1* gene

2.2.1 General materials

2.2.1.1 List of enzymes

Enzyme	Article number*
AflII	R0520
AgeI-HF	R3552
AscI	R0558
BamHI-HF	R3136
DraI	R0129
DraIII-HF	R3510
EcoRI-HF	R3101
HindIII-HF	R3104
KpnI-HF	R3142
MluI	R0198
NdeI	R0111
NotI-HF	R3189
PflMI	R0509
PmeI	R0560
PvuI-HF	R3150
RsrII	R0501
SacI-HF	R3156
SalI-HF	R3138
ScaI-HF	R3122
StuI	R0187
XmnI	R0194
T4 DNA ligase	M0202
Antarctic phoshatase	M0289
Phusion high fidelity DNA polymerase	M0530

*All enzymes were purchased from New England BioLabs® (NEB, Ipswich, Massachusetts, USA), HF means High-Fidelity

2.2.1.2 List of kits

Kits	Supplier (catalog number)
GenElute plasmid miniprep kit	Sigma-Aldrich (PLN350)
Promega PureYield plasmid maxiprep System	Promega (A2393)
Qiagen plasmid *Plus* maxi kit	Qiagen (12963)
High pure PCR product purification kit	Roche Life Science (11732676001)
Transcriptor first strand cDNA synthesis kit	Roche Life Science (04896866001)
RNeasy micro kit (50)	Qiagen (74004)

Megaprime DNA Labeling System, dNTP	GE Healthcare (RPN1605)
Wizard SV gel and PCR clean up system	Promega (A9281)

2.2.1.3 Oligodeoxyribonucleotide primers

All oligodeoxyribonucleotide primers were purchased from Sigma-Aldrich in a lyophilized form and stored at -20°C until use. Stock solution (100 µM) was prepared by dissolving DNA in deionized water as per the manufacturer's instructions and stored at -20°C. Working solution of 10 µM was used in all experiments. The name, sequence (5'-3'), melting temperature (Tm), forward (F) or reverse (R) orientation and application/purpose of the respective oligodeoxyribonucleotide primers is listed in tables below **(Table 2-1 to Table 2-5)**

Table 2-1 Oligodeoxyribonucleotides for the generation of the *Trpc1*-IC targeting vector and amplification of cDNAs used as probes in Southern blots

Primer name	Oligodeoxyribonucleotide sequence (5'-3')	Tm (°C)	F or R	Application
CM_82	GTCGACGATATCGGTGTCTCTGG GGAGGGG	62	R	Cloning pAR_1, 5´P, *SalI* and EcoRV site
CM_83	CTTAAGAGCTTCCAAATGCTGACA CC	60	F	Amplification of 3´2 with AflII site
CM_84	CTTAAGGCTACACAGAGAAACCC TGT	60	F	Amplification of 3´2 with AflII site
CM_85	CTTAAGCCTTTCATCTGATTTTGT AACC	60	R	Amplification of 3´2 with AflII site
CM_86	CTTAAGACAGGGTTTCTCTGTGTA GC	60	R	Amplification of 3´2 with AflII site
CM_87	CCATAAGGGATCTCAGAAAGG	62	F	Amplification of 3'1 probe (IC)
CM_88	ACCTCTTGTCTATCTTTTGGC	60	R	Amplification of 3'1 probe (IC)
CM_89	GGCATTTGAAACTCAGTCCC	60	F	Amplification of 3'2 probe (IC)
CM_90	CAGAGGAAGTCCTCTGTCC	60	R	Amplification of 3'2 probe (IC)
CM_91	AGGCATACCTTTGGGTTAGG	60	F	Amplification of 3'3 probe (IC)
CM_92	CAGGCTCAACTTAAAATTCATC	60	R	Amplification of 3'3 probe (IC)
CM_93	TAGAATTATGCTTGTGTCAACC	60	F	Amplification of 3'4 probe (IC)
CM_94	GTTGCTAAATCATAACTTCATCC	62	R	Amplification of 3'4 probe (IC)
CM_95	GCATAATAAATGTTAAGAAGTGC	60	F	Amplification of 5'1 probe (IC)
CM_96	AGTGTAAAGGCTGTTCTAAGTTC	60	R	Amplification of 5'1 probe (IC)
CM_97	TCTATTCTAGTCCTCCTGCC	60	F	Amplification of 5'2 probe (IC)
CM_98	GGTGGGTCACTTAGGAAGAC	62	R	Amplification of 5'2 probe (IC)
CM_99	CAACAACAAATACGAGGAGATG	62	F	Amplification of 5'3 probe (IC)
CM_100	ATCCTATAGGTAAAGATGATGAA	60	R	Amplification of 5'3probe (IC)
CM_101	CCAGTGCATTAAGGAAAATGTG	62	F	Amplification of 5'4 probe (IC)
CM_102	GAAGAGGAATTAGCCCTAAAAG	62	R	Amplification of 5'4 probe (IC)

CM_103	CGCGTCTTAAGTAGTAGATCC	62	F	Sequencing 5'Homology (IC)
CM_104	GGATCTACTACTTAAGACGCG	62	R	Sequencing 5'Homology (IC)
CM_105	CCTGAAGGCTGAAGTAGAGG	62	F	Sequencing 5'Homology (IC)
CM_106	CCTCTACTTCAGCCTTCAGG	62	R	Sequencing 5'Homology (IC)
CM_107	GCTGTGATTGTTGGAACTTAC	60	F	Sequencing 5'Homology (IC)
CM_108	GTAAGTTCCAACAATCACAGC	60	R	Sequencing 5'Homology (IC)
CM_109	CCTCATTCTTACTATGTAGCTG	62	F	Sequencing 5'Homology (IC)
CM_110	CAGCTACATAGTAAGAATGAGG	62	R	Sequencing 5'Homology (IC)
CM_111	CTAGGGAAAACAGAATTCCCT	60	F	Sequencing 5'Homology (IC)
CM_112	AGGGAATTCTGTTTTCCCTAG	60	R	Sequencing 5'Homology (IC)
CM_125	CCATAACAGATCTGAAAGACTG	62	F	Sequencing 3'Homology (IC)
CM_126	CAGTCTTTCAGATCTGTTATGG	62	R	Sequencing 3'Homology (IC)
CM_127	CACAGAGAAATCCTGTCTTGG	62	F	Sequencing 3'Homology (IC)
CM_128	CCAAGACAGGATTTCTCTGTG	62	R	Sequencing 3'Homology (IC)
CM_129	GGTTTCCCAGCTGTCGCATG	64	F	Sequencing 3'Homology (IC)
CM_130	CATGCGACAGCTGGGAAACC	64	R	Sequencing 3'Homology (IC)
CM_131	CCATGTAGGGACTAAATTGAG	60	F	Sequencing 3'Homology (IC)
CM_132	CTCAATTTAGTCCCTACATGG	60	R	Sequencing 3'Homology (IC)
CM_133	GCGCCAAGATCTGTCAAAATT	60	F	Sequencing pAR_9 (IC)
CM_134	GGCTTCGGCCAGTAACGTTA	62	R	Sequencing pAR_9 (IC)
CM_135	GGCTTCTGAGGCGGAAAGA	60	F	Sequencing pAR_9 (IC)
CM_136	GCAAGTATGCAAATACAGTCT	58	R	Sequencing pAR_9 (IC)
CM_137	CGCCGGATCTGATATCATCG	62	F	Sequencing pKO.ICF
CM_138	CGATGATATCAGATCCGGCG	62	R	Sequencing pKO.ICF
CM_139	TAACGTTACTGGCCGAAGCC	62	F	Sequencing pKO.ICF
CM_140	CACGGGGACGTGGTTTTCC	62	F	Sequencing pKO.ICF
CM_141	GGAAAACCACGTCCCCGTG	62	R	Sequencing pKO.ICF
CM_143	CGATCGCTGCCAGGATATAC	62	F	Sequencing pKO.ICF
CM_144	GTATATCCTGGCAGCGATCG	62	R	Sequencing pKO.ICF
CM_145	CCGTAACCTGGATAGTGAAAC	62	F	Sequencing pKO.ICF
CM_146	GTTTCACTATCCAGGTTACGG	62	R	Sequencing pKO.ICF
CM_147	TTCTGGGCTCAGAGGCTGG	62	F	Sequencing pKO.ICF
CM_148	CCAGCCTCTGAGCCCAGAA	62	R	Sequencing pKO.ICF
CM_149	GCTCCTGCCGAGAAAGTATC	62	F	Sequencing pKO.ICF
CM_150	GATACTTTCTCGGCAGGAGC	62	R	Sequencing pKO.ICF
CM_151	GCTCGCTGATCAGCCTCGA	62	F	Sequencing pKO.ICF
CM_152	TCGAGGCTGATCAGCGAGC	62	R	Sequencing pKO.ICF

Table 2-2 Oligodeoxyribonucleotides for the generation of *Trpc1*-flox targeting vector and amplification of cDNAs used as probes in Southern blots

Primer name	Oligodeoxyribonucleotide sequence (5'-3')	Tm (°C)	F or R	Application
CM_159	GCTCCATTGTTACTTCACATG	60	F	Cloning of 5'Probe1*Trpc1*_C1Z
CM_160	CCTGCTGTATGTTCTGATCAG	62	R	Cloning of 5'Probe1*Trpc1*_C1Z
CM_161	CCAGTGTCCAAGTACCACAAC	64	F	Cloning of 5'Probe2*Trpc1*_C1Z
CM_162	CCTGCGCTATCTGAAATTTCAG	64	R	Cloning of 5'Probe2*Trpc1*_C1Z

CM_163	GGCTAAACATTTTGCTGAGCA	60	F	Cloning of 5'Probe3*Trpc1*_C1Z
CM_164	CCTCGTTCCTAAAGGCGTTT	60	R	Cloning of 5'Probe3*Trpc1*_C1Z
CM_165	CCTTGGATGAAGGACCAAGTT	62	F	Cloning of 3'Probe1*Trpc1*_C1Z
CM_166	CCAGTATAGCAAAATCAGTGTC	62	R	Cloning of 3'Probe1*Trpc1*_C1Z
CM_167	CCAAGTCAGTGTGCTTAGGC	62	F	Cloning of 3'Probe2*Trpc1*_C1Z
CM_168	CCAAGAATGAAACTACAGCAGA	62	R	Cloning of 3'Probe2*Trpc1*_C1Z
AR_1	CCTGCCCTAGTTGCCGAAA	60	F	Sequencing 5'Hom *Trpc1*_C1Z
AR_2	TTTCGGCAACTAGGGCAGG	60	R	Sequencing 5'Hom *Trpc1*_C1Z
AR_3	GGTTTAAGTCAACAACATCTCC	62	F	Sequencing 5'Hom *Trpc1*_C1Z
AR_4	GGAGATGTTGTTGACTTAAACC	62	R	Sequencing 5'Hom *Trpc1*_C1Z
AR_5	GGGTGAAGAGAGTATAATTAGT	60	F	Sequencing 5'Hom *Trpc1*_C1Z
AR_6	ACTAATTATACTCTCTTCACCC	60	R	Sequencing 5'Hom *Trpc1*_C1Z
AR_7	GGATTAAAGGCGTGCACCAC	62	F	Sequencing 5'Hom *Trpc1*_C1Z
AR_8	GTGGTGCACGCCTTTAATCC	62	R	Sequencing 5'Hom *Trpc1*_C1Z
AR_9	CCAGTAGGATTTCTTTGGGTT	60	F	Sequencing 5'Hom *Trpc1*_C1Z
AR_10	AACCCAAAGAAATCCTACTGG	60	R	Sequencing 5'Hom *Trpc1*_C1Z
AR_11	GCTAGCCCAGTTTCCAGTG	60	F	Sequencing 5'Hom *Trpc1*_C1Z
AR_12	CACTGGAAACTGGGCTAGC	60	R	Sequencing 5'Hom *Trpc1*_C1Z
AR_13	CCACTGTGAACTGAATCCAAC	62	F	Sequencing 5'Hom *Trpc1*_C1Z
AR_14	GTTGGATTCAGTTCACAGTGG	62	R	Sequencing 5'Hom *Trpc1*_C1Z
AR_15	GGGTTTGCTGTGTCACAGG	60	F	Sequencing 5'Hom *Trpc1*_C1Z
AR_16	CCTGTGACACAGCAAACCC	60	R	Sequencing 5'Hom *Trpc1*_C1Z
AR_17	CCAAAGACGAGATGTAACTTG	60	F	Sequencing 5'Hom *Trpc1*_C1Z
AR_18	CAAGTTACATCTCGTCTTTGG	60	R	Sequencing 5'Hom *Trpc1*_C1Z
AR_19	CGACTTAAGAGCATCACTTCA	60	F	Sequencing 5'Hom *Trpc1*_C1Z
AR_20	TGAAGTGATGCTCTTAAGTCG	60	R	Sequencing 5'Hom *Trpc1*_C1Z
AR_21	GGATGACAAGTTTGTGGCCT	60	F	Sequencing 5'Hom *Trpc1*_C1Z
AR_22	AGGCCACAAACTTGTCATCC	60	R	Sequencing 5'Hom *Trpc1*_C1Z
AR_23	GCGAGTGATCTAGAAGCGC	60	F	Sequencing 3'Hom *Trpc1*_C1Z
AR_24	GCGCTTCTAGATCACTCGC	60	R	Sequencing 3'Hom *Trpc1*_C1Z
AR_25	CCAGTCACTTAGCTGTCTAG	60	F	Sequencing 3'Hom *Trpc1*_C1Z
AR_26	CTAGACAGCTAAGTGACTGG	60	R	Sequencing 3'Hom *Trpc1*_C1Z
AR_27	CCACAGTCAGTCTATCAAGA	58	F	Sequencing 3'Hom *Trpc1*_C1Z
AR_28	TCTTGATAGACTGACTGTGG	58	R	Sequencing 3'Hom *Trpc1*_C1Z
AR_29	CCATACCTGACCCAAATGTC	60	F	Sequencing 3'Hom *Trpc1*_C1Z
AR_30	GACATTTGGGTCAGGTATGG	60	R	Sequencing 3'Hom *Trpc1*_C1Z
AR_31	CCAGGGAATCCAATGCCCC	62	F	Sequencing 3'Hom *Trpc1*_C1Z
AR_32	GGGGCATTGGATTCCCTGG	62	R	Sequencing 3'Hom *Trpc1*_C1Z
AR_33	CCTATAAGAGCAGTCACAGC	60	F	Sequencing 3'Hom *Trpc1*_C1Z
AR_34	GCTGTGACTGCTCTTATAGG	60	R	Sequencing 3'Hom *Trpc1*_C1Z
AR_51	CCGTCAGGATGGCCTTCTG	62	F	Sequencing 5'Hom *Trpc1*_C1Z
AR_52	GGGAGTTAAGGAGGGAGGGA	62	F	Sequencing 5'Hom *Trpc1*_C1Z
AR_53	CCGCCAGCCTGTATTTCGG	62	F	Sequencing 5'Hom *Trpc1*_C1Z
AR_54	CCGAAATACAGGCTGGCGG	62	R	Sequencing 5'Hom *Trpc1*_C1Z
AR_55	CTTGAGGCTGGACATGTGCC	64	R	Sequencing *Trpc1*_C1Z
AR_56	CCTCCAGCGCGGGGATCT	62	F	Sequencing *Trpc1*_C1Z
AR_57	AGATCCCCGCGCTGGAGG	62	R	Sequencing *Trpc1*_C1Z

AR_58	CTGTGCACATGTCCACATGC	62	R	Sequencing *Trpc1*_C1Z
AR_59	CCCTGCATCAGACGGAAGTAA	62	F	Sequencing *Trpc1*_C1Z
AR_60	TTACTTCCGTCTGATGCAGGG	62	R	Sequencing *Trpc1*_C1Z
AR_61	GGAGTTAGATCAGGAAGCGC	62	F	Sequencing *Trpc1*_C1Z
AR_62	GCGCTTCCTGATCTAACTCC	62	R	Sequencing *Trpc1*_C1Z
AR_63	CTAGACAGCTAAGTGACTGG	60	R	Sequencing 3'Hom *Trpc1*_C1Z
AR_64	GTACAGCGGTACAGAAGACC	62	R	Sequencing 3'Hom *Trpc1*_C1Z
AR_65	GATTGGGAAGACAATAGCAGG	62	R	Sequencing *Trpc1*_C1Z
AR_66	CAGCTTACGAACCGAACAGG	62	R	Sequencing *Trpc1*_C1Z
AR_67	CCTTTGGCTTTCACACCACC	62	R	Sequencing 3'Hom *Trpc1*_C1Z
AR_68	CCTTGAAGGACTCCAATAGG	60	R	Sequencing *Trpc1*_C1Z
AR_69	CCAGAGGCTCAAGGCTGAGT	64	F	Sequencing *Trpc1*_C1Z
AR_70	ACTCAGCCTTGAGCCTCTGG	64	R	Sequencing *Trpc1*_C1Z
AR_71	CCATTCGACCACCAAGCGAA	62	F	Sequencing *Trpc1*_C1Z
AR_72	CCTGCATCAGACGGAAGTAAA	62	F	*Trpc1*_C1Z _loxP-PCR
AR_73	GTGAGGAACATTTATTCATGTG	60	R	*Trpc1*_C1Z _loxP-PCR
AR_74	CCTGTTTCCTTTCCCTGCAT	60	F	*Trpc1*_C1Z _loxP-PCR
AR_75	AGGAGAAAACCAAATTGAACTG	60	R	*Trpc1*_C1Z _loxP-PCR

Table 2-3 Oligodeoxyribonucleotides for the genotyping of *Trpc1*-IC KI mouse strain

Primer name	Oligodeoxyribonucleotide sequence (5'-3')	Tm (°C)	F or R	Application
AR_76	GGATTTGCTTGGCTTTCGGA	60	F	*Trpc1*_SubF_IC_genotyping
AR_77	CAAAAGACGGCAATATGGTGG	62	R	*Trpc1*_SubF_IC_genotyping
AR_78	CTTCGGCCAGTAACGTTAGG	62	R	*Trpc1*_SubF_IC_genotyping
AR_79	GGGCGGAATTCATCGATGAT	60	R	*Trpc1*_SubF_IC_genotyping

Table 2-4 Oligodeoxyribonucleotides for the genotyping of conditional *Trpc1* mouse strain

Primer name	Oligodeoxyribonucleotide sequence (5'-3')	Tm (°C)	F or R	Application
AR_80	CCGCCAGCCTGTATTTCGG	62	F	*Trpc1*_MANN_flox_genotyping
AR_81	GCGGAATTCTCTAGAGTCCA	60	R	*Trpc1*_MANN_flox_genotyping
AR_82	CCGGTCGCTACCATTACCA	60	F	*Trpc1*_MANN_flox_genotyping
AR_83	GCGTGCAATCCATCTTGTTC	60	R	*Trpc1*_MANN_flox_genotyping
AR_84	CCTTCTTGACGAGTTCTTCTG	60	F	*Trpc1*_MANN_flox_genotyping
AR_85	GCTGGGTCTAGATATCTCGA	60	R	*Trpc1*_MANN_flox_genotyping
AR_86	GGACTACGGTTGTCAGGTAC	62	F	*Trpc1*_MANN_flox_genotyping

Table 2-5 Additional genotyping primers

Primer name	Oligodeoxyribonucleotide sequence (5'-3')	Tm (°C)	F or R	Application
SD_222	CCCATTCCATGCGGGGTATCG	68	F	Flp recombinase_genotyping
SD_223	GCATCTGGGAGATCACTGAG	62	R	Flp recombinase_genotyping
Cre_1	ACCTGAAGATGTTCGCGATTATCT	68	F	Cre recombinase_genotyping
Cre_2	ACCGTCAGTACGTGAGATATCTT	64	R	Cre recombinase_genotyping

new ROSA	GGAAGCACTTGCTCTCCCAAAG	70	F	τGFP_genotyping
new eROSA	GGGCGTACTTGGCATATGATACAC	72	R	τGFP_genotyping

2.2.1.4 List of buffer solutions

For miniprep (crude preparation of small amount of plasmid DNA)	*STET-L buffer, pH 8.0* 8% (w/v) Sucrose 5% (v/v) Triton X-100 0.05 M EDTA 0.05 M Tris Add Lysozyme (100 µg/mL) freshly added from 10 mg/mL Lysozyme stock solution
For maxiprep (preparation of large amount, ≥0.5 mg, of plasmid DNA)	*Cell resuspension solution* 50 mM Tris-HCl (pH 7.5) 10 mM EDTA 100 µg/mL RNase A *Cell lysis solution* 0.2 M NaOH 1% (w/v) SDS *Neutralization solution, pH 4.2* 4.09 M guanidine hydrochloride 0.759 M potassium acetate 2.12 M glacial acetic acid
For DNA storage	*TE-buffer, pH 8.0,* autoclaved 10 mM Tris 1 mM EDTA
For preparation of chemical competent bacterial cells	*Transformation storage solution (TSS) buffer* 10% (w/v) PEG 3350 5% (v/v) DMSO 1% (w/v) Tryptone/Peptone 1% (w/v) NaCl 0.5% (w/v) Yeast extract 0.05 M $MgCl_2$
For gel electrophoresis	*Tris-Borate-EDTA (TBE) buffer, pH 8.0* 90 mM Tris base 90 mM Boric acid 2 mM EDTA
	Loading buffer (6x) 0.25% (v/v) Bromophenol blue 15% (w/v) Ficoll 400 0.25% (v/v) Xylencyanol

For genotyping PCR	*10x Taq buffer, pH 8.3* 0.1 M Tris 0.5 M KCl 0.015 M $MgCl_2$
For genomic DNA preparation for genotyping	*Tissue lysis buffer, pH 8.0* 50 mM Tris HCl 100 mM NaCl 1 mM EDTA 0.5% (w/v) proteinase K 0.2% (w/v) Nonidet P40 0.2% (w/v) Tween-20
For Southern blot	0.25 *N Hydrochloric acid* 20.76 mL Hydrochloric acid (37%) ad 1000 mL deionized H_2O; used for *depurination*
	Denaturation buffer 0.5 M NaOH 1.5 M NaCl
	Neutralization buffer, pH 7.5 0.5 M Tris 3 M NaCl
	10x SSC, pH 7.0 0.15 M Sodium citrate 1.5 M NaCl
	Church buffer 0.5 M Sodium phosphate (pH 7.4) 1% (w/v) BSA 7% (w/v) SDS 1 mM EDTA 0.1 mg/mL Salmon sperm DNA, Roche, (added after being denatured at 95°C for 5 minutes)

2.2.1.5 Media for bacterial culture

Luria-Bertani (LB) medium, pH 7.4

Tryptone/Peptone 10 g
NaCl 10 g
Yeast extract 5 g
Deionized H_2O ad 1000 mL
autoclaved at 121°C, 2.0 bar for 20 minutes.

LB-agar

15 g/L agar in LB-medium, autoclaved at 121°C, 2.0 bar for 20 min and plated after cooling down to 50°C.

Antibiotics
Added in LB-medium just before plating at the following final concentrations
Ampicillin 50 µg/mL
Kanamycin 25 µg/mL

2.2.2 General methods

2.2.2.1 Restriction endonuclease treatment of plasmid DNA

Restriction enzyme reactions were carried out to generate the required DNA fragments for linearization of vector plasmids and validation of the integrity of the recombinant plasmid. Single or combinations of two different restriction enzymes were used in the reactions. Combinations of enzymes were used either simultaneously if reaction conditions were similar for both enzymes or a sequential incubation approach was used if reaction conditions were different for each enzyme. Table below summarizes the composition of a typical restriction digest used:

Component (reagent)	Quantity (µL)	Final concentration
Template DNA	variable	0.5-2 µg
Enzyme 1	1	10 U*
Enzyme 2	1	10 U
Restriction buffer (10x)	5	1x
Water, nuclease-free	ad 50 µL	

*usually ≤1/10 of total volume

After pipetting, all components were thoroughly mixed and incubated at 37°C or 25°C depending on the enzyme.

2.2.2.2 Gel electrophoresis

Agarose gel electrophoresis was used for the separation of DNA fragments based on their sizes. 0.6-4% agarose gels were used depending on the expected band sizes in the individual cloning steps. The agarose gel was prepared by dissolving agarose standard (CarlRoth) powder in 1xTBE-buffer and boiled for several minutes in a microwave until a transparent solution was obtained. Approximately, after 3 min of mild cooling by keeping at 21°C, ethidium bromide (0.05% v/v) was added followed by pouring the agarose solution into a gel tray. Ethidium bromide, a fluorescent dye, intercalates with the DNA double strands and absorbs radiation at wavelengths from 302 nm to 366 nm and re-emits energy at 590 nm (Le Pecq and Paoletti, 1966). The agarose gel solution was incubated for 20 min at 21°C for solidification and finally

stored at 4°C or directly used for running the samples. The DNA samples were solved in loading buffer (10x) applied to the gel wells and electrophoresis was performed at 100–150 V (Consort EV 261). Molecular weight markers were run in the same gel to determine the molecular weights of DNA products. The separated DNA fragments were visualized using a UV light transilluminator (HeroLab UVT-28 ME-HC) and images were taken using an attached camera (Herolab B1228-U5). For the gel purification of DNA fragments, an appropriate DNA band was excised from the gel using a sterile scalpel, the DNA was extracted from the gel by either electroelution or using a Wizard SV gel and PCR clean up system (Promega) according to the manufacturer's instructions.

2.2.2.3 Purification of DNA by electroelution

The excised portion of an agarose gel containing the required DNA fragment was placed inside a dialysis bag (Dialysis Tubing, Sigma-Aldrich) and 250 µL of autoclaved 1xTBE buffer was added (avoiding air bubbles as much as possible). The dialysis bag was sealed with the plastic clips and placed in a special electrophoresis chamber (Bio-Rad, PowerPac HC) for electroelution to occur at 135 mA at 4°C for 20-30 minutes. Electroelution was briefly monitored by UV light (312 nm). When electroelution was complete the solution containing the eluted DNA was collected. The bag was rinsed with additional 250 µL nuclease free H_2O and added to the solution containing the DNA. The DNA was finally purified using the high pure PCR product purification kit (Roche) which works on the principle of binding of DNA to the special glass fibers of filter tubes due to the presence of chaotropic salt guanidine thiocyanate and subsequent washing steps to remove the contaminants. The DNA concentration was determined using a NanoDrop spectrophotometer. The DNA was stored at -20°C until used for the ligation reaction.

2.2.2.4 Dephosphorylation of a plasmid DNA

Antarctic phosphatase was used to dephosphorylate 5' and 3' ends of DNA to prevent re-ligation of a linearized plasmid. The following protocol was applied:

26 µL linearized plasmid DNA
3 µL 10x antarctic buffer
1 µL antarctic phosphatase (5U/µL)

The reaction mixture (30 µL) was incubated at 37°C for 60 min; afterwards the enzyme was inactivated by incubating the sample at 80°C for two minutes. The dephosphorylated plasmid DNA was stored at -20°C until used for ligation reaction.

2.2.2.5 Generation of recombinant plasmids by a ligation reaction

The T4 DNA ligase catalyzes the formation of a phosphodiester bond between juxtaposed 5'-phosphate and 3'-hydroxyl ends in double stranded DNA. In a ligation reaction, ratio of mol vector and mol fragment ranges from 1:3 to 1:10. The protocol was as follows:

variable	plasmid DNA (vector)
variable	fragment DNA (insert)
1 µL	T4 DNA Ligase (400U/ µL)
2 µL	10x ligase buffer
20 µL	ad deionized water

The reaction mixture was incubated at 21°C for 60 min for ligation of "sticky" ends or overnight at 16°C for ligation of "blunt" ends. The ligase enzyme was inactivated at 65°C for ten minutes. The recombinant plasmids were then used to transform bacteria.

2.2.2.6 Bacterial transformation

Transformation refers to the process of direct up-take of exogenous plasmid DNA by bacteria through the membrane on exposure either to a chemical or electrical stimulus. Bacteria which have the ability of accepting foreign DNA are called the competent cells.

Generation of competent bacteria

To generate competent bacteria, *E.Coli* were grown overnight on ampicillin containing LB agar plates. One colony was used to inoculate 5 mL LB medium and thereafter the suspension was incubated for 16 h at 37°C without any antibiotic to obtain a pre-culture. Under sterile conditions, 1 mL pre-culture was added to 100 mL LB medium present in a baffled-flask and incubated for 2 h at 37°C with gentle shaking (orbital) at 260 rpm. Once the optical density (OD_{600}) reached 0.4-0.5, the bacterial suspension was centrifuged at 1600 g for 10 min at 4°C. The supernatants were discarded and the pellet was re-suspended in 15 mL ice-cold transformation storage solution (TSS) (Chung *et al.,* 1989). A total amount of 300 µL suspension was added to pre-cooled 1.5 mL eppendorf tubes followed by snap freezing using liquid nitrogen. The competency of prepared chemically competent bacterial cells was estimated by transforming the plasmid pUC18 and plating the transformed bacteria on

ampicillin containing plates. The transformation efficiency should be $5x10^6$ to $5x10^7$ independent bacterial colonies per µg pUC18 DNA. The bacterial cells were stored at -80°C until used for the transformation of ligation products during individual cloning steps.

Transformation of chemically competent bacterial cells

The suspension containing competent bacteria (300 µL) was thawed at 4°C for 5 min followed by the addition of 20 µL plasmid/ligation reaction and incubated for 30 min at 4°C. After incubation for 2 min at 42°C (water-bath) the suspension was immediately incubated for 2 min at 4°C. Pre-warmed 900 µL LB-medium was added to the bacterial suspension, followed by incubation for 1 h at 37°C with mild shaking (150 rpm). A portion of bacterial suspension (150 µL) was transferred onto a specific antibiotic-resistant LB-agar plate and the remaining portion was centrifuged at 800 g for 2 minutes. The supernatants were discarded and the pellet was dissolved in 150 µL LB medium and finally plated on a second LB-agar plate. The plates were incubated for approximately 16 h (overnight) at 37°C. The resulting bacterial colonies were used for the isolation of plasmid DNA.

2.2.2.7 Extraction of plasmid DNA

The isolation of plasmid DNA from bacteria is divided into two procedures based on the amount of DNA to be isolated.

Analytical isolation of plasmid DNA (Miniprep)

The "boiling method" (Holmes and Quigley, 1981) was used with slight modifications for the isolation of plasmid DNA. Individual bacterial colonies were picked by autoclaved wooden toothpicks under sterile conditions and used to inoculate 5 mL LB medium containing ampicillin. The tubes were incubated overnight at 37°C with mild shaking in an orbital shaker at 270 rpm. A portion of bacterial suspension was poured into 1.5 mL eppendorf tubes and centrifuged at 16100 g for 1 minute. The supernatants were discarded and the pellet was dissolved in 300 µL freshly prepared STET-L buffer. The tubes were incubated for 5 min on ice followed by a thermal shock for 1 min at 95°C. After centrifugation at 16100 g for 15 min, a gelatinous pellet was obtained. The pellet was removed with the wooden toothpick under sterile conditions and 300 µL of isopropanol was added followed by centrifugation at 16100 g for 30 minutes. The supernatants were discarded and the precipitate was washed (16100 g x 10 min) with 500 µL of 70% (v/v) ethanol, air-dried and dissolved in 50 µL water with RNase (40 µg/mL). The DNA was subjected to endonuclease restriction enzyme digestion.

Preparative isolation of plasmid DNA (Maxiprep)

After identifying the bacterial clones carrying the desired plasmid DNA by restriction enzyme digestion and subsequent sequencing, the next step was to isolate the plasmid DNA on a larger preparative scale. An Erlenmeyer flask containing 250 mL LB-medium and appropriate antibiotic was inoculated with 500 µL of bacterial suspension containing the desired plasmid. The flask was incubated overnight at 37°C with mild shaking at 200 rpm in an orbital shaker. For DNA isolation, two different maxiprep kits were used: Promega PureYield plasmid maxiprep System (Promega) and Qiagen plasmid *Plus* maxi kit (Qiagen). The extraction of plasmid DNA is based on the principle of alkaline lysis of bacterial cells followed by removal of the contaminants and binding of DNA to a column, finally plasmid DNA is eluted from the column in an appropriate buffer solution after successive washing steps. The DNA was extracted according to the manufacturer's instructions and stored at -20°C until use for other cloning purposes. The amount and integrity of the isolated DNA was analyzed using a NanoDrop spectrophotometer.

2.2.2.8 Determination of DNA concentration and quality

The concentration and quality of a DNA sample in an aqueous solution was determined by measuring its UV absorbance at 260 and 280 nm. The NanoDrop 1000 spectrophotometer (Thermo Scientific) was used which measures samples as small as one µL with high accuracy and reproducibility. The purity of the DNA was estimated by comparing the ratio of absorbance at 260 and 280 nm. A ratio of >1.8 was considered to be a pure DNA sample. The base line of the NanoDrop 1000 was set by water or TE buffer.

2.2.3 Southern blot technique

Southern blotting involves the transfer of electrophoretically separated DNA fragments onto a filter membrane and subsequent fragment detection by hybridizing with a radioactively labelled DNA probe. For Southern blot, 15-30 µL of hydrolyzed genomic DNA was incubated overnight at 37°C by a specific endonuclease restriction enzyme (40 U); the fragments were electrophoretically separated on a 0.6% agarose gel along with a marker, a 1 Kb DNA ladder (Invitrogen). Electrophoresis was performed at 140 V for about 3.5-4 h followed by imaging of the gel under UV light (HeroLab UVT-28 ME-HC). A fluorescent ruler was coincided with the gel in such a way that the starting zero-point matched to the level of loading wells for

estimation of DNA sizes after hybridization. After imaging, the gel was treated with 0.25 N HCl for 45 min for the depurination of genomic DNA. Depurination lays the phosphate-sugar backbone of DNA open to subsequent cleavage by hydroxyl ions. By this procedure the DNA is nicked, which improves transfer of fragments >10 Kb. Subsequently the gel was rinsed with distilled water, followed by incubation with the denaturation and neutralization buffers for 45 and 30 min respectively, with mild shaking at 21°C. Denaturation ultimately causes the conversion of a double-stranded DNA structure into a single strand DNA molecules by breaking the hydrogen bonds present between the complementary strands of the double helix of DNA. The gel was washed once with distilled water and placed over a Whatman 3MM filter paper lying on two spontex sponges soaked in 10x SSC transfer buffer in a steel pan. A gel-sized pre-wet Hybond-N nylon membrane (RPN203N, GE Healthcare, Amersham) was placed over the gel squeezing out the air bubbles by rolling a glass pipette, followed by two or three Whatman filter papers, a stack of tissue papers and a metal or glass plate. A weight of about 0.8-1 kg was placed on the top of the plate to start the transfer of genomic DNA towards the membrane by a capillary action. In order to prevent any leaky transfer of the buffer, the empty space around the gel was covered with parafilm strips. After 16 h of incubation, the nylon membrane was removed and transferred DNA was immobilized by cross-linking in Stratalinker UV cross linker (Agilent) at 0.12 J/cm^2, autocrosslink mode, followed by incubating the membrane at 80°C for two hours.

2.2.3.1 Southern probes preparation and labeling

The Southern probes (5’ and 3’ probes) for both targeting constructs, pAR_11 and C1Z, used for the generation of *Trpc1*-IC knock-in and conditional *Trpc1* knockout mice respectively, were prepared by the PCR amplification of genomic DNA, obtained from mouse (*mus musculus*, C57BL/6N strain) DNA using different primer combinations **(Table 2-1, 2-2)**. These primer combinations (forward and reverse) were designed to amplify specific regions called probes, ranging from 450 bp to 780 bp in length, placed outside the homology arms to detect the precise integration of a targeting construct within the endogenous DNA in ES cells upon homologous recombination. The PCR reaction mix and conditions used for the generation of 5’ and 3’ probes are shown below:

PCR composition:

Component (reagent)	Quantity (µL)	Final concentration
Genomic DNA	1	variable
5x Phusion buffer HF	10	1x
10 mM dNTP's	1	200 µM
2U/µL DNA polymerase	0.5	1 U
10 µM forward primer	2.5	0.5 µM
10 µM reverse primer	2.5	0.5 µM
Deionized H_2O	ad 50	

PCR protocol:

Steps	Temperature (°C)	Time	Number of cycles
Initial denaturation	98	60 s	1
Denaturation Annealing Elongation	98 63 72	10 s 20 s 30 s	27
Final extension	72	5 min	1
Hold	4	α	

The amplified PCR product was subcloned into the EcoRV cut pUC18 or pBlueKS cloning vectors. After ligation and transformation, the bacterial clones containing a desired recombinant plasmid were selected after miniprep, restriction enzyme cut and sequencing. The correct plasmids were prepared by maxiprep and the amplified DNA fragments obtained by appropriate restriction enzymes. In the next step the cDNA fragments were labelled by ^{32}P. A random oligo-primed DNA synthesis method was used to label DNA fragments to be used as probes for Southern hybridization. The probe labeling was performed using a Megaprime DNA labeling system (GE Healthcare Life Sciences). The reaction mixture was composed of DNA (≈25-30 ng), denatured by incubating at 95°C for 10 min and subsequent chilling for 3 min at 4°C, an appropriate amount of random hexamer primers, reaction buffer, Klenow polymerase and a mixture of nucleotides including $\alpha[^{32}P]$dCTP (Hartman Analytic).

Component	Quantity (µL)
DNA (≈25-30 ng)	variable
Primer solution	5
Reaction buffer (10x)	5
dATP	4
dGTP	4
dTTP	4
$\alpha[^{32}P]$dCTP (10 µCi/µL)	5
Klenow's enzyme (1 U/µL)	2

Deionized H_2O	ad 50

The mixture was incubated for 30 min at 37°C. The polymerase incorporated the nucleotides including the radioactive $\alpha[^{32}P]$dCTP into the newly synthesized complementary DNA (Feinberg and Vogelstein, 1984). The DNA was separated from non-incorporated nucleotides with 1x TE-buffer by gel filtration through NICK-columns Sephadex G-50 DNA grade (Cat. No. 17-0855-02, GE Healthcare). The elutes from the columns were collected in six individual tubes. To identify the labelled DNA and to quantify the efficacy of $\alpha[^{32}P]$dCTP incorporation, the aliquots from the six tubes were measured by liquid scintillation counting in a Wallac 1409 scintillation counter. The fractions 2 and 3 contained the labelled probes, which were later used for the hybridization.

2.2.3.2 Southern hybridization

Southern blot membrane was pre-hybridized by incubating for two hours at 65°C (mild shaking) in pre-warmed Church buffer (Church and Gilbert, 1984) to block the non-specific binding sites of the membrane. After pre-hybridization, the membrane was incubated with the hybridization solution (1 mL/cm^2 membrane surface) overnight at 65°C in a sealed plastic bag. The hybridization solution consisted of church buffer and denatured $\alpha[^{32}P]$dCTP labelled probe (2-4x10^7 cpm/mL). The denaturation of probe was carried out at 95°C for 10 min followed by rapid chilling at 4°C for 3 minutes. After overnight hybridization, the membrane was washed twice with increasing stringency *i.e.* 2x SSC/1% SDS followed by 0.4x SSC/1% SDS in a shaking water bath at 65°C for 15 min each. After the first washing step, the radioactivity on the blot and in the washing solution was monitored by a Geiger-Müller counter (LB 122, Berthold). The membrane was then exposed to a phosphoimager screen (Fujifilm BAS-IP MP 2040) which was scanned after 4 h and 24 h of exposure time by a phosphoimager (BAS reader, Raytest). In cases of weaker signals obtained after 24 h exposition time, the membrane was exposed for additional three days to one week.

2.2.4 ES cell gene targeting

The strategy and generation of the targeting constructs is described in the “Results” section. The vectors carrying the final targeting constructs (100 µg) were linearized by incubation in the presence of restriction endonucleases at 37°C for 4-7 hours. The linearized plasmids were cleaned by High pure PCR product purification kit (Roche) and send on ice to *ingenious* Targeting Laboratory*, iTL,* (Ronkonkoma, New York, USA). *iTL* performed electroporation into

C57BL/6 ES cells and selected ES cell clones by positive and negative selection. Aliquots of selected ES cells were sent to Homburg and I prepared DNA from these clones performed Southern blot analysis using 3'-, 5'- and neo DNA probes.

2.2.5 Detection of positively targeted ES cell clones

After electroporation, ES cell clones were picked up by *iTL* and 288 lyophilized clones were shipped in nine 32-well plates. The DNA of these clones was dissolved by the addition of 300 µL 1xTE buffer followed by incubation at 55°C for 3 h with mild shaking (300 rpm). The genomic DNA was stored at 4°C until restriction enzyme cut, agarose gel electrophoresis and Southern blot analyses were performed. For the detection of correctly targeted ES cell clones three probes were used; a 5'- probe and 3'- probe also known as "external probes" derived from sequences outside the homology arms and the neomycin resistance (neo) probe also known as "internal probe". The targeting construct, C1Z contained one of the *loxP* sites present adjacent to the 3' homology arm, therefore additional PCR was performed to confirm the correct insertion of that particular *loxP* site upon homologous recombination. According to the results of Southern blot and PCR the correct ES cell clones (5-6 in both cases) were expanded and karyotyped by *iTL*. The selected clones were then injected into the BALB/c blastocysts by *iTL* and by Interfakultäre Biomedizinische Forschungseinrichtung (IBF) Heidelberg University. Blastocysts were then transferred in pseudopregnant mothers which gave birth to pups which carried or did not carry the targeted allele.

2.2.6 Genotyping strategy for the identification of germline transmission of the inserted mutation

A PCR based genotyping strategy was established to distinguish between wild-type and mutant mouse strains in the F1 generation. Several primer combinations were designed spanning over various regions of the mutant allele. After identification of the desired mutant mouse strain, the mice were transferred to our laboratory from *iTL*. The heterozygous mice were housed in the quarantine of the animal facility of the Medical Faculty directed by Dr. Petra Weissgerber (Gebäude 61.4, Uniklinikum Homburg). By embryo transfer mice were introduced into the specific pathogen free animal facility. Mice were kept under a standard light/dark cycle (12 h) with food and water *ad libitum*. All breeding were conducted according to the regulations of the local authority and the ethics committee of the Saarland.

2.2.6.1 Genomic DNA preparation

Genomic DNA required for genotyping PCR was isolated from tissue samples obtained from individual mice by an ear punch. The tissue sample was incubated in lysis buffer for approximately 16 h at 55°C with vigorous shaking and stored thereafter at 4°C until use. One µL of the lysed tissue was taken as a template to perform PCR to identify the genotype.

2.2.6.2 Genotyping PCR

The PCR protocol and steps used were:

a. PCR protocol:

Component (reagent)	Quantity (µL)	Final concentration
Genomic DNA	1	variable
10x PCR buffer	2.5	1x
10 mM dNTPs	0.5	200 µM
25 mM $MgCl_2$	0.5	500 µM
Taq polymerase	1	≈1 U
10 µM forward primer	1.25	0.5 µM
10 µM reverse primer	1.25	0.5 µM
Deionized H_2O	ad 25	

b. PCR steps:

Gene	PCR conditions		Fragment size (bp)
Flp	94°C : 3 min		mt fragment: 750
	94°C : 30 s 58°C : 60 s 72°C : 60 s	35x	
	72°C : 5 min		
	15°C: ∞		
Trpc1-IC KI and *Cre*-recombinase	94°C : 90 s		*Trpc1*-IC KI detection: mt fragment: 192
	94°C : 30 s 65°C : 30 s 72°C : 30 s	10x*	*Cre*-recombinase detection: mt fragment: 392
	94°C : 30 s 60°C : 30 s 72°C : 30 s	26x	

	72°C : 5 min		
	15°C : ∞		
eROSA26	94°C : 5 min		wt fragment: 256 mt fragment: 495
	94°C : 35 s	35x	
	56°C : 45 s		
	72°C : 90 s		
	72°C : 7 min		
	15°C : ∞		

*(0.5°C decrease per cycle)

2.2.7 Statistical methods

Data were analyzed using Microsoft Excel and GraphPad Prism 5. Data are shown as mean ± SD or mean ± SEM. To estimate the significance of differences, two-tailed unpaired student's t-test for two groups and one way ANOVA followed by Bonferroni multiple comparison test for more than two groups were performed. The difference was found significant if the P-value < 0.05 (*), <0.01 (**) or < 0.001 (***).

3 Results

In this section, the results obtained for the three major goals of my thesis have been described.

3.1 Micro-computed tomography

3.1.1 Bone microarchitecture of different strains of wild-type mice

In order to understand the bone microarchitecture and to dissect the roles of TRP channels-especially of TRPC1 and TRPV6 in bone, I had to establish µCT of long bones as a method to screen bone microarchitecture. An important point is that bone microarchitecture changes with age and strongly depends on the mouse strain. So before comparing bones from wild-type mice with the bones from *Trpc1*$^{-/-}$, *Trpv6*$^{mt/mt}$ and *Trpc1*$^{-/-}$*/Trpv6*$^{mt/mt}$ mice, a clear phenotypic characterization of the bones from wild-type mice of the most common strains used for gene targeting, B6 strain (C57BL/6) and mice of a mixed genetic background (129SvJ/C57BL/6) had to be analyzed.

For that purpose, I had first to establish the use of a SkyScan1172 µCT and data acquisition using appropriate tasklists of the available software. With good advice from Dr. Phil Salmon, Application Scientist at Bruker microCT Systems, Kontich, Belgium, and with great help from Professor Dr. Bram van der Eerden from Erasmus Medical Centre, Rotterdam, The Netherlands, I succeeded in establishing the µCT methods of analyses. We decided to analyze only long bones, femurs, from male mice to reduce additional effects of the cycling hormonal status on bones, which is most prominent in females.

First, I weighed the C57BL/6 (from now on “B6”) and the 129SvJ/C57BL/6 (from now on “mixed”) mice at different ages **(Figure 3-1A, B)** and determined the femur length **(Figure 3-1D, E)**. Until 20-week of age there was a steady increase in weight of mice of both strains, with mixed mice were approximately 10% heavier especially at week 2 and week 12 compared to C57BL/6 **(Figure 3-1C)**. The length of femurs from mixed mice reached maximum (16.5 ± 0.24 mm) at week 12 **(Figure 3-1D)** but femur length from C57BL/6 increased from week 2 (8.4 ± 0.67 mm) to week 24 (15.99 ± 0.22 mm) **(Figure 3-1E)**. Femur length of mixed mice was slightly larger than that of C57BL/6 at week 12 **(Figure 3-1F)**.

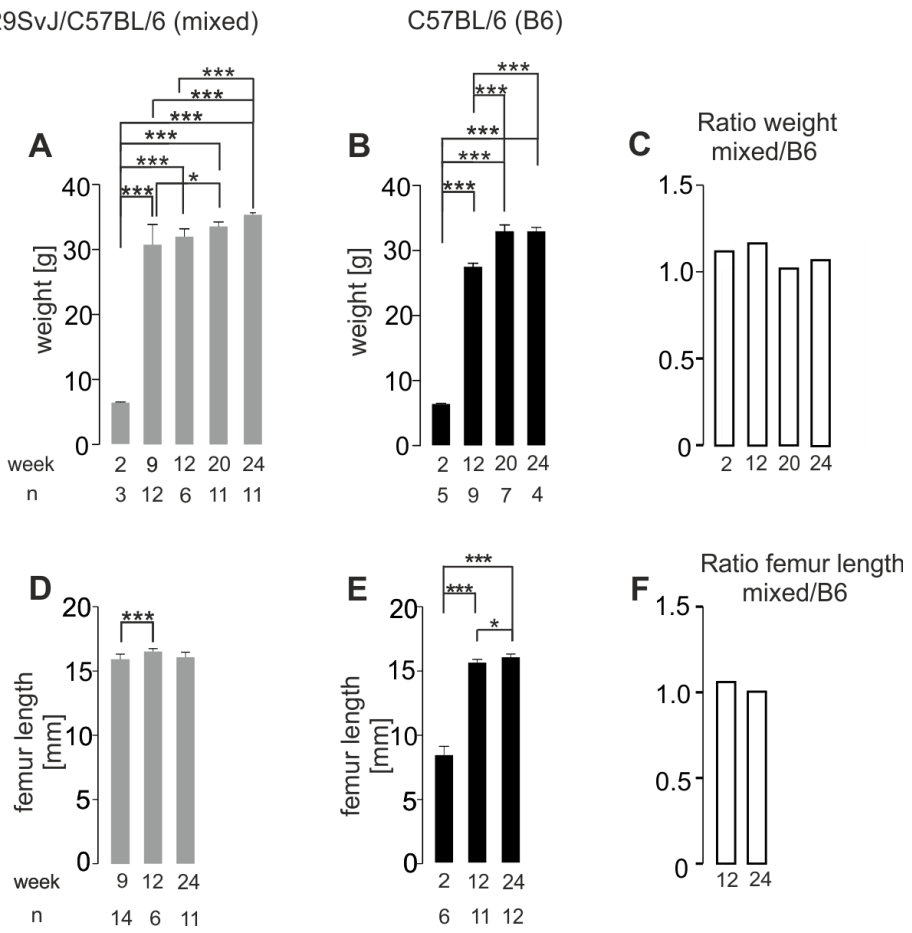

Figure 3-1 Comparison of weight and femur length of wild-type mice on mixed (129SvJ/C57BL/6) and B6 (C57BL/6) strains of different age groups. (A, B) Comparison of weight and **(D, E)** femur length estimated by µCT of wild-type male mice on mixed genetic background 129SvJ/C57BL/6 (grey bars) and B6 strain, C57BL/6 background (black bars) of different ages such as 2, 9, 12, 20 and 24 weeks. For the estimation of differences between the strains, ratios were calculated for weight **(C)** and femur length **(F)**. Data shown as mean ± SD with n, number of mice or femurs given below the bar graphs. Data analysed by one-way ANOVA with consecutive Bonferroni multiple comparison test ($p<0.05$ *, $p<0.001$ ***). Age in weeks and n indicated below the bar graphs.

Next, I analyzed the cortical parameters of femurs by µCT, averaged from fifty 6.5 µm cross-sections from the middle of the femur's diaphysis **(Figure 2-5)**. Cortical bone parameters **(Figure 3-2A)** include bone volume, endocortical volume, cross-sectional thickness and perimeter. These parameters are highlighted in red in the left column of **Figure 3-2A.** In the right column the values obtained for femurs from C57BL/6 (B6) and 129SvJ/C57BL/6 mice (mixed) are indicated, for 12-week of age (black bars) and 24-week of age (grey bars). Endocortical volume and perimeters were increased in femurs from 24-week compared to 12-week old C57BL/6 mice whereas bone volume and cross-sectional thickness were not different

(Figure 3-2A). In femurs from mice of the mixed background, bone volume and cross-sectional thickness decreased with age, whereas endocortical volume and perimeters were not changed. The estimated mineral density (g/cm^3) of cortical bone was not significantly different between any of the groups tested (1.33 ± 0.02 (B6, 12-week), 1.32 ± 0.06 (B6, 24-week), 1.32 ± 0.01 (mixed, 12-week), 1.31 ± 0.05 (mixed, 24-week), number of femurs as in **Figure 3-2**). **Table 3-1** summarizes all data obtained to characterize cortical bone by µCT.

Trabecular bone parameters **(Figure 3-2B)** averaged from metaphyseal sections as shown in **(Figure 2-5)** include bone volume as percentage of total tissue volume, trabecular number, trabecular thickness and trabecular separation as highlighted in red in the left column **(Figure 3-2B)**. In addition, I determined the trabecular pattern factor, which describes the 3D connectivity of the trabeculae by calculating an index of relative convexity or concavity of the total bone surface (Morphometric parameters measured by SkyScan^{TM} CT-analyser software). In mice of mixed background, the percentage of bone volume from tissue volume and the trabecular number decreased indicating an age-dependent loss of bone **(Figure 3-2B,** right column**)**. These values are mirrored by an increase of trabecular separation and of the trabecular pattern factor **(Figure 3-2B,** right column**)** as well as an age-dependent loss of mineral density (g/cm^3) (0.20 ± 0.04 (B6, 12-week) 0.19 ± 0.03 (B6, 24-week), 0.29 ± 0.02 (mixed, 12-week) 0.16 ± 0.02 (mixed, 24-week)). Determination of mineral density measured by µCT is only an estimation considering the attenuation of X-rays by the bone compared to the attenuation of X-rays by calcium hydroxyapatite “phantoms”. (So far, we did not apply quantitative backscattered electron imaging, qBEI, which is only available in very few laboratories, as a direct method to determine bone mineral density). **Table 3-2** summarizes all data obtained to characterize trabecular bone by µCT.

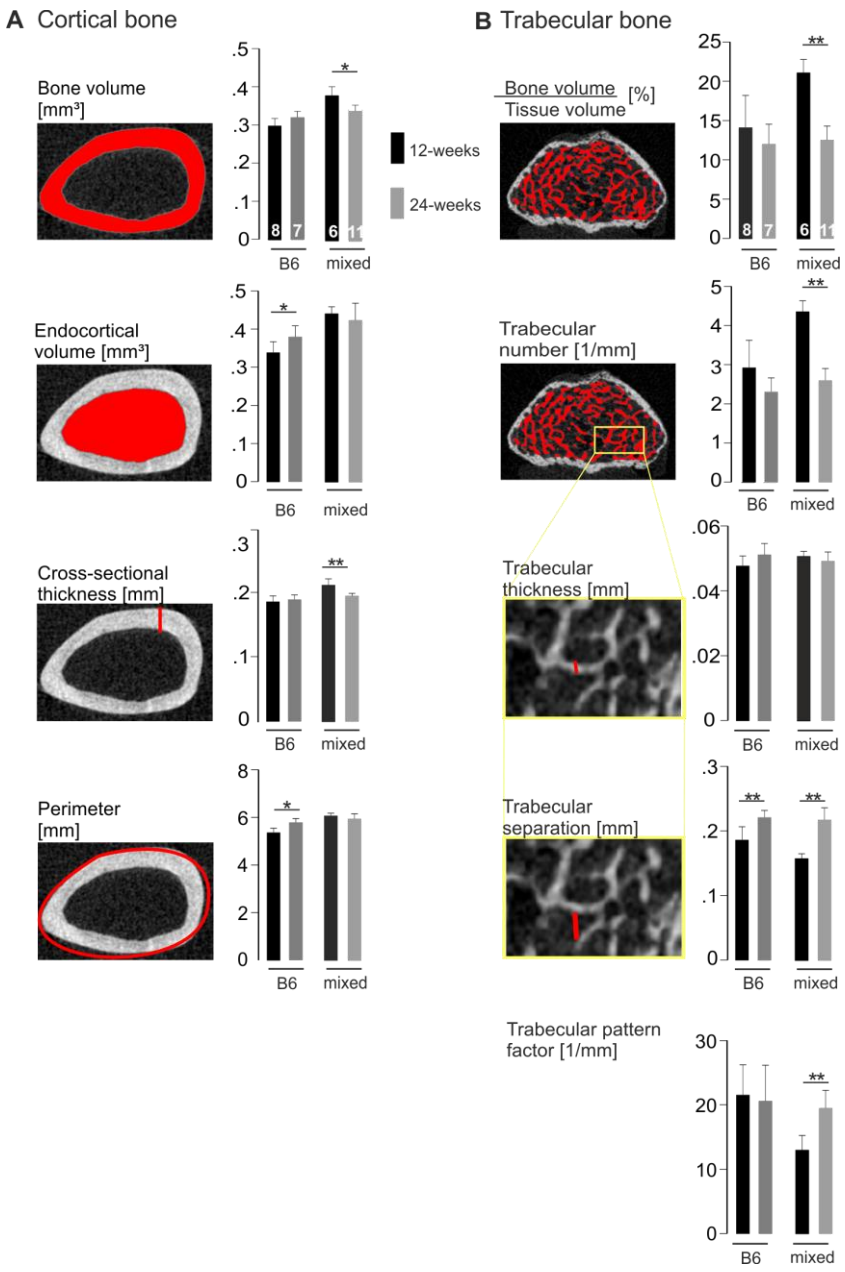

Figure 3-2 Comparison of bone microarchitecture from 12- and 24-week-old wild-type male mice on B6 strain, C57BL/6 and mixed strain, 129SvJ/C57BL/6. (A) Cortical bone parameters, left column indicate the cross-sectional images to depict the cortical parameters, right column depicts the graphical representation of cortical bone parameters: Bone volume (mm^3), endocortical volume (mm^3), cross-sectional thickness (mm) and perimeter (mm). **(B)** Trabecular bone parameters, left column indicates the cross-sectional images to depict the trabecular parameters, right column shows the graphical representation of trabecular parameters such as bone volume fraction (%), trabecular number (1/mm), trabecular thickness (mm), trabecular separation (mm) and trabecular pattern factor (1/mm). Values shown as mean ± SD, the number of femurs for each group is indicated in the upper most bars-graphs. Two-tailed unpaired student's t-test was performed on 12- and 24-week-old mice dataset for each genetic background (p-value summary, $p<0.05$ *, $p<0.01$ **). Black and grey bar graphs represent data obtained from femurs of 12- and 24-week-old mice.

Femurs of mice from C57BL/6 showed only minor age dependent differences **(Figure 3-2B** and **Table 3-1, 3-2)**: we observed a non-significant tendency of age-dependent reduction of percentage of bone volume and trabecular number, which however was sufficient to yield a significant increase of trabecular separation. The trabecular pattern factor and the mineral density estimated by µCT were not different.

		n	Bone volume, [mm³]	Endocortical volume, [mm³]	Cross sectional thickness, [mm]	Perimeter, [mm]	Bone volume, [mm³]	Endocortical volume, [mm³]	Cross sectional thickness, [mm]	Perimeter, [mm]	Bone volume, [mm³]	Endocortical volume, [mm³]	Cross sectional thickness, [mm]	Perimeter, [mm]	Bone volume, [mm³]	Endocortical volume, [mm³]	Cross sectional thickness, [mm]	Perimeter, [mm]
C57BL/6	12w	8	0.29 ± 0.02	0.34 ± 0.03	0.19 ± 0.01	5.41 ± 0.18	Ø	Ø	Ø	↑*	↑***	↑***	↑***	↑***				
	24w	7					0.32 ± 0.02	0.38 ± 0.03	0.19 ± 0.01	5.7 ± 0.17					Ø	Ø	Ø	Ø
129SvJ/C57BL/6	12w	6									0.38 ± 0.02	0.44 ± 0.02	0.21 ± 0.01	6.08 ± 0.11	↓***	Ø	↓***	Ø
	24w	11													0.34 ± 0.02	0.42 ± 0.04	0.19 ± 0.004	5.87 ± 0.22
			12w				24w				12w				24w			
			C57BL/6								129SvJ/C57BL/6							

Table 3-1 Comparison of cortical bone parameters of 12- and 24-week-old mice on C57BL/6 (B6) and 129SvJ/C57BL/6 (mixed) genetic backgrounds, Ø= no change, ↑= increase compared to reference in the left column and ↓= decrease compared to reference in the left column, calculated as mean ± SD by one-way ANOVA followed by Bonferroni multiple comparison test (* indicates p-value < 0.05 and *** p-value < 0.001). For example, perimeter of femurs obtained from 24-week B6 mice is increased compared to femurs from 12-week B6 mice (black arrow); bone volume of femurs from 12-week mixed mice is larger than bone volume of femurs obtained from 12-week B6 mice (red arrow); bone volume of femurs from 24-week mixed is smaller than bone volume of femurs from 12-week mixed mice (black arrow).

By directly comparing the parameters obtained from the femurs from C57BL/6 and from mixed mice, the data revealed that cortical bone values from mixed femurs, independent of age, are larger than those from C57BL/6 femurs. Whereas in trabecular bone, values obtained only from 12-week mixed femurs, not from 24-week mixed femurs, are more effected compared to 12-week and 24-week C57BL/6 femurs. Accordingly, age-dependent differences are more apparent in femurs from mixed than from B6 mice.

		n	Bone volume fraction, [%]	Trabecular thickness, [mm]	Trabecular separation, [mm]	Trabecular number, [1/mm]	Trabecular pattern factor, [1/mm]	Bone volume fraction, [%]	Trabecular thickness, [mm]	Trabecular separation, [mm]	Trabecular number, [1/mm]	Trabecular pattern factor, [1/mm]	Bone volume fraction, [%]	Trabecular thickness, [mm]	Trabecular separation, [mm]	Trabecular number, [1/mm]	Trabecular pattern factor, [1/mm]	Bone volume fraction, [%]	Trabecular thickness, [mm]	Trabecular separation, [mm]	Trabecular number, [1/mm]	Trabecular pattern factor, [1/mm]
C57BL/6	12w	8	14.16 ± 4.07	0.05 ± 0.003	0.19 ± 0.02	2.93 ± 0.70	21.51 ± 4.68	∅	∅	↑***	∅	∅	↑***	∅	↓**	↑***	↓**					
	24w	7						12.07 ± 2.5	0.05 ± 0.003	0.22 ± 0.01	2.31 ± 0.36	20.6 ± 5.57						∅	∅	∅	∅	∅
129SvJ/C57BL/6	12w	6											21.03 ± 1.69	0.05 ± 0.001	0.15 ± 0.007	4.26 ± 0.27	12.48 ± 2.18	↓***	∅	↑***	↓***	↑*
	24w	11																12.44 ± 1.78	0.05 ± 0.002	0.21 ± 0.018	2.56 ± 0.304	19.15 ± 2.70
			12 w					24 w					12 w					24 w				
			C57BL/6										129SvJ/C57BL/6									

Table 3-2 Comparison of trabecular bone parameters of 12- and 24-week-old mice on C57BL/6 (B6) and 129SvJ/C57BL/6 (mixed) genetic backgrounds, Ø= no change, ↑= increase compared to reference in the left column and ↓= decrease compared to reference in the left column, calculated as mean ± SD by one-way ANOVA followed by Bonferroni multiple comparison test (* indicates p-value < 0.05, ** p-value < 0.01 and *** p-value < 0.001). For example, trabecular separation in femurs obtained from 24-week B6 mice is increased compared to femurs from 12-week B6 mice (black arrow); bone volume fraction in femurs from 12-week mixed mice is larger than bone volume fraction in femurs obtained from 12- week B6 mice (red arrow); bone volume fraction of femurs from 24-week mixed is smaller than bone volume fraction of femurs from 12-week mixed mice (black arrow).

3.1.2 Comparison of normal femur microarchitecture of WT, *Trpc1*$^{-/-}$, *Trpv6*$^{mt/mt}$ and double mutant *Trpc1*$^{-/-}$/*Trpv6*$^{mt/mt}$ mice

Next I wanted to analyze femurs from wild-type, *Trpc1*$^{-/-}$, *Trpv6*$^{mt/mt}$ and *Trpc1*$^{-/-}$/*Trpv6*$^{mt/mt}$ mice. Before starting these experiments, I confirmed that transcripts of *Trpc1* and *Trpv6* are present in RNA extracted from 1) osteoclasts differentiated and cultivated from bone marrow, 2) crushed femur and 3) osteoblasts migrating out of bone slices and cultivated thereafter. **Figure 3-3** shows that *Trpc1* transcripts are present in osteoclast **(Figure 3-3A)**, crushed femur **(Figure 3-3A, B)** and in osteoblast **(Figure 3-3C)**. By similar experiments, I could amplify *Trpv6* transcripts in crushed femur **(Figure 3-3D)** and thereby confirm previous results described by van der Eerden *et al.* (van der Eerden *et al.,* 2012).

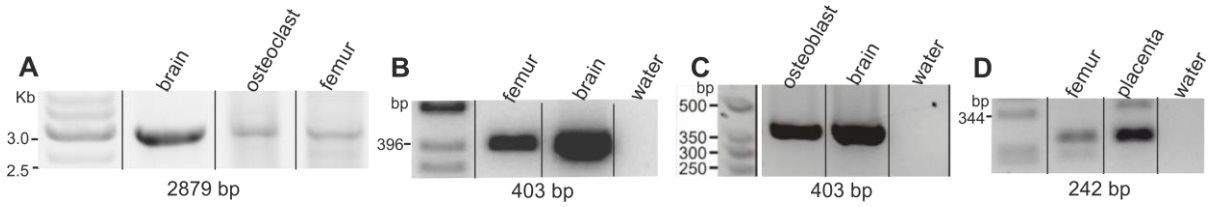

Figure 3-3 *Trpc1* and *Trpv6* transcripts are present in mRNA extracted from bone cells or bone. Representative agarose gels: **(A)** Amplification of the full length TRPC1-encoding transcript (2879 bp) from mouse bone marrow derived *in vitro* cultured osteoclasts and crushed bone (femur). **(B), (C)** *Trpc1* transcript (403 bp) in mRNA from crushed bone (femur) and mouse bone marrow derived *in vitro* cultured osteoblasts. **(D)** *Trpv6* transcript (242 bp) in mRNA from crushed bone (femur). Messenger RNA from brain and placenta or no mRNA (water) used as positive and negative controls. Size marker for each gel (Kb or bp) are indicated.

Trpc1 and *Trpv6* encode proteins, which form tetrameric cation channels. However, no antagonists for these two channel types are available. In order to get hold of these *Trpc1* and *Trpv6* function in bone we analyzed and compared femurs from *Trpc1*$^{-/-}$ mice, *Trpv6*$^{mt/mt}$ mice and *Trpc1*$^{-/-}$*/Trpv6*$^{mt/mt}$ double mutant mice: Functional deficits or additional functions of the bones from mutant mice compared to bones from wild-type mice should point to the functions of *Trpc1* and *Trpv6*. All mice of four different groups were on the same genetic background *i.e.* mixed strain (129SvJ/C57BL/6) and 24-weeks old. The length of femurs from *Trpv6*$^{mt/mt}$ mice and from *Trpc1*$^{-/-}$*/Trpv6*$^{mt/mt}$ mice was smaller than the length of femurs from the wild-type and *Trpc1*$^{-/-}$mice **(Figure 3-4A)** but their estimated cortical mineral densities were not different **(Figure 3-4B)**.

There was a significant increase in cortical bone volume of *Trpc1*$^{-/-}$*/Trpv6*$^{mt/mt}$ femurs whereas endocortical volume was reduced by approximately 30% in *Trpv6*$^{mt/mt}$ and *Trpc1*$^{-/-}$*/Trpv6*$^{mt/mt}$ femurs compared to WT and *Trpc1*$^{-/-}$ femurs. The cortical cross-sectional thickness was significantly increased in both *Trpv6*$^{mt/mt}$ and *Trpc1*$^{-/-}$*/Trpv6*$^{mt/mt}$ femurs compared to WT and *Trpc1*$^{-/-}$ femurs. Moreover, there was a significant increase in cross-sectional thickness of *Trpc1*$^{-/-}$*/Trpv6*$^{mt/mt}$ femurs compared to *Trpv6*$^{mt/mt}$ femurs. The perimeter of the femoral shaft was significantly reduced in *Trpv6*$^{mt/mt}$ and *Trpc1*$^{-/-}$*/Trpv6*$^{mt/mt}$ femurs compared to the bones from wild-type and *Trpc1*$^{-/-}$ mice. In summary, the data indicate a prominent cortical phenotype especially in femurs from *Trpv6*$^{mt/mt}$ mice, which also persists in the *Trpc1*$^{-/-}$*/Trpv6*$^{mt/mt}$ femurs. Whereas *Trpc1* deletion has almost no effect.

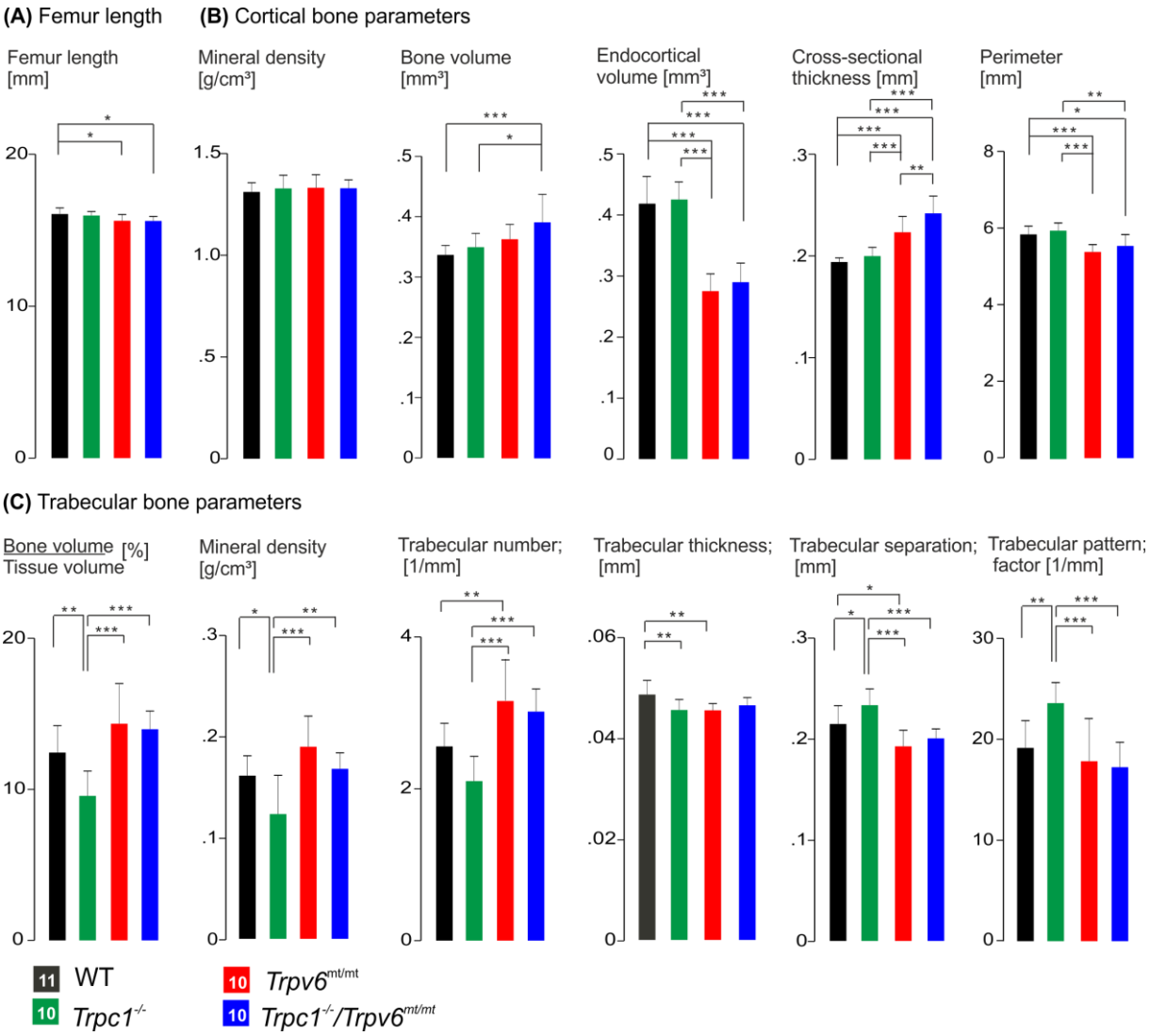

Figure 3-4 Analyses of intact femurs. Femur length **(A)**, cortical- **(B)** and trabecular- **(C)** femur bone parameters of wild-type, *Trpc1*$^{-/-}$, *Trpv6*$^{mt/mt}$ and double mutant *Trpc1*$^{-/-}$/*Trpv6*$^{mt/mt}$ mice determined by µCT. Data are shown as mean ± SD, analyzed by one-way ANOVA followed by Bonferroni multiple comparison test (* indicates p-value < 0.05, ** p-value < 0.01 and *** p-value < 0.001). The four genotypes are indicated in black (wild-type, WT), green (*Trpc1*$^{-/-}$), red (*Trpv6*$^{mt/mt}$) and blue (*Trpc1*$^{-/-}$/*Trpv6*$^{mt/mt}$), with the number of femurs for each group is indicated in the bottom squares.

The µCT data revealed a prominent trabecular phenotype in *Trpc1*$^{-/-}$ compared to WT mice **(Figure 3-4C)**. The ratio of trabecular bone volume/tissue volume, the mineral density and the trabecular thickness were significantly reduced in femurs of *Trpc1*$^{-/-}$ mice compared to femurs from WT mice. In line with these observations, trabecular separation and trabecular pattern factor were significantly increased in femurs of *Trpc1* deficient mice compared to WT femurs. I also analyzed femurs from 12-week-old wild-type and *Trpc1*$^{-/-}$ mice on B6 background and a similar trabecular phenotype was observed **(**supplementary **Figure 6-8)** indicating that this

phenotype is independent of the genetic background. We also observed significant differences in trabecular parameters of femurs from both *Trpv6*$^{mt/mt}$ and *Trpc1*$^{-/-}$*/Trpv6*$^{mt/mt}$ mice in comparison to femurs from *Trpc1*$^{-/-}$ mice: Trabecular bone volume fraction, mineral density and trabecular number were significantly increased while trabecular separation and trabecular pattern factor were significantly reduced in *Trpv6*$^{mt/mt}$ and *Trpc1*$^{-/-}$*/Trpv6*$^{mt/mt}$ femurs compared to *Trpc1*$^{-/-}$ mice. In summary, trabecular bone volume fraction and mineral density is effected by *Trpc1* deletion but not by *Trpv6* mutation, which in *Trpc1*$^{-/-}$*/Trpv6*$^{mt/mt}$ femurs rescues the wild-type phenotype. Similarly, the increased trabecular number and reduced trabecular separation is caused by mutation of *Trpv6* both in *Trpv6*$^{mt/mt}$ and *Trpc1*$^{-/-}$*/Trpv6*$^{mt/mt}$ femurs. These differences in healthy bone parameters led us to establish a fracture model in our laboratory for studying the fracture healing, especially the callus formation in femurs after a defined fracture.

3.1.3 Fractured femur analyses of wild-type, *Trpc1*$^{-/-}$, *Trpv6*$^{mt/mt}$ and double mutant *Trpc1*$^{-/-}$*/Trpv6*$^{mt/mt}$ mice

As outlined in **section 2.1.3.5** and **Figure 2-6**, I established a protocol to derive callus parameters of fractured femurs from 24-week-old male mice, four weeks after fracture, of four different genotypes. The fracture healing of WT mice were compared with the healing of *Trpc1*$^{-/-}$, *Trpv6*$^{mt/mt}$ and double mutant *Trpc1*$^{-/-}$*/Trpv6*$^{mt/mt}$ mice. All mice used in this study had the same genetic background, *i.e.* mixed (129SvJ/C57BL/6). Fractured femurs were removed and after explanting the screws, they were scanned by SkyScan 1172 µCT. We also compared the weight of individual mice immediately before producing the fracture and four weeks later, prior to explanting the screw. We observed no significant reduction in weight of mice during the healing phase, (supplementary **Figure 6-2)**. The µCT data showed that callus parameters remained unchanged in WT and *Trpc1*-deficient femurs **(Figure 3-5)** whereas the volume of total callus and bone volume, the mineralized portion within the callus were approximately 50% reduced in *Trpv6*$^{mt/mt}$ and *Trpc1*$^{-/-}$*/Trpv6*$^{mt/mt}$ mice compared to WT and *Trpc1*$^{-/-}$ mice **(Figure 3-5A)**. A significant increase in mineral density and trabecular number was seen in *Trpv6*$^{mt/mt}$ and *Trpc1*$^{-/-}$*/Trpv6*$^{mt/mt}$ mice compared to WT and *Trpc1*$^{-/-}$ mice. A significant reduction in trabecular separation in *Trpv6*$^{mt/mt}$ and *Trpc1*$^{-/-}$*/Trpv6*$^{mt/mt}$ mice was observed fitting with the increase in trabecular number. The trabecular thickness of callus tissue was not different between the groups **(Figure 3-5A)**.

We also assessed the extent of mineralization by determining the volume of highly and low mineralized bone within the callus of all four groups using two different threshold ranges to estimate the proportion of highly mineralized callus calculated at the threshold range of 98-255 and of low mineralized callus at threshold range of 68-97. The amount of highly mineralized bone was significantly increased in callus tissue from *Trpv6*$^{mt/mt}$ and *Trpc1*$^{-/-}$*/Trpv6*$^{mt/mt}$ mice compared to callus in WT and *Trpc1*$^{-/-}$ mice. To summarize, fractured femur analyses showed significant reduction of total callus volume and a higher proportion of bony callus in *Trpv6*$^{mt/mt}$ and *Trpc1*$^{-/-}$*/Trpv6*$^{mt/mt}$ as compared to callus in wild-type and *Trpc1*$^{-/-}$ mice **(Figure 3-5B, C)**.

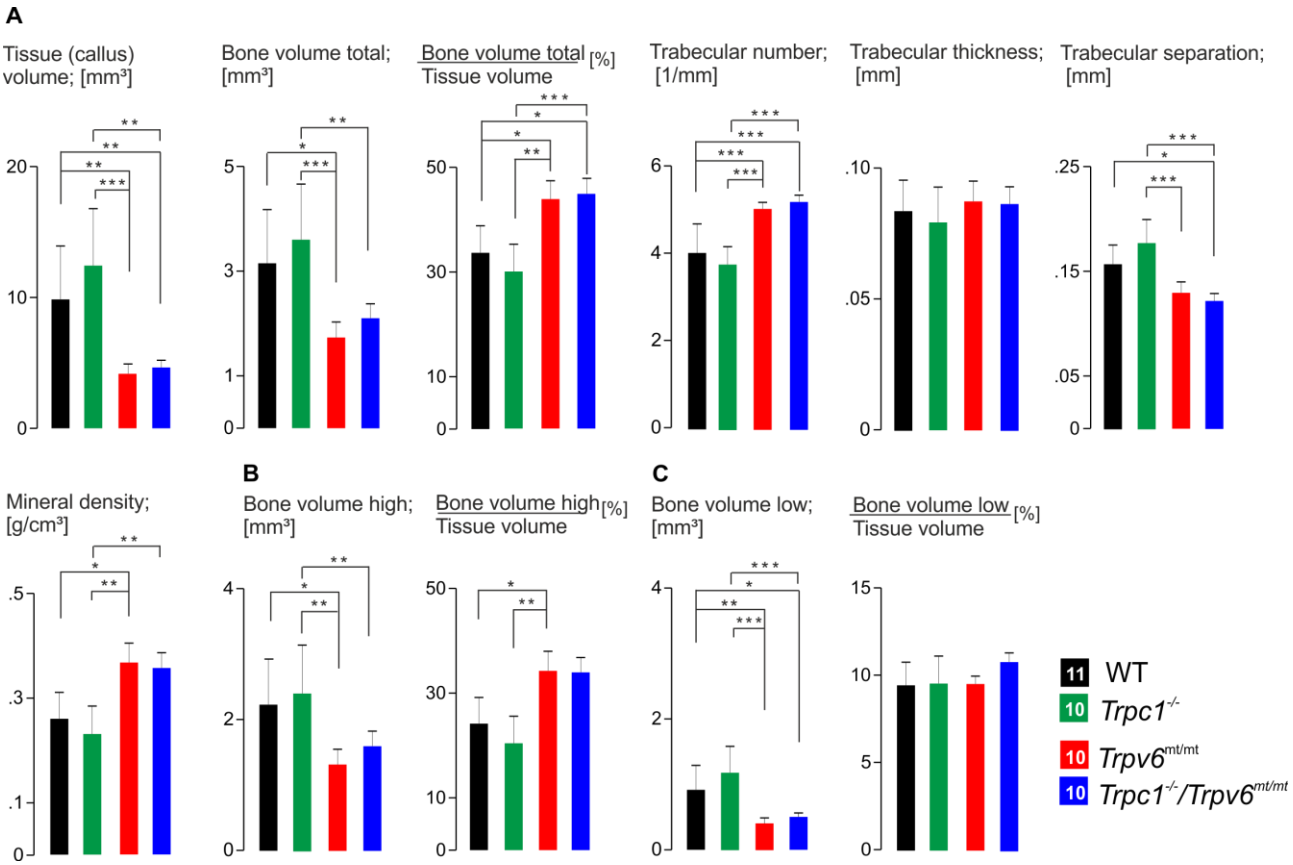

Figure 3-5 Analyses of femurs four weeks after fracture. The defined fracture was applied to 20-weeks old wild-type, *Trpc1*$^{-/-}$, *Trpv6*$^{mt/mt}$ and double mutant *Trpc1*$^{-/-}$*/Trpv6*$^{mt/mt}$ mice. Fractured femurs scanned by SkyScan 1172 to evaluate **(A)** callus parameters determined at a grayscale range of 68-255. **(B, C)** Volume and percentage of highly and low mineralized bone within the callus tissue determined at a threshold range of 98-255 (high) and 68-97 (low). Data shown as mean ± SD statistically calculated by one-way ANOVA followed by Bonferroni multiple comparison test ($p<0.05$ *, $p<0.01$ **, $p<0.001$ ***). The bars represent WT (black), *Trpc1*$^{-/-}$(green), *Trpv6*$^{mt/mt}$ (red) and *Trpc1*$^{-/-}$*/Trpv6*$^{mt/mt}$ (blue), with the number of animals for each group is indicated in the color legends.

3.2 Biomechanical properties of femora

The µCT data helps in understanding the bone microarchitecture but provides minimal insight into the mechanical properties of bone. Therefore, we measured the biomechanical properties of intact and fractured femurs by a 3-point bending device (Herath *et al.*, 2015). The bones from wild-type animals were compared with *Trpc1*$^{-/-}$, *Trpv6*$^{mt/mt}$ and double mutant *Trpc1*$^{-/-}$/*Trpv6*$^{mt/mt}$ mice. As above, all mice used in this experiment were on mixed (129SvJ/C57BL6/N) genetic background and twenty-four weeks old. The data revealed significant increase in bending stiffness of bones from *Trpv6*$^{mt/mt}$ and *Trpc1*$^{-/-}$/*Trpv6*$^{mt/mt}$ as compared to WT and *Trpc1*$^{-/-}$ mice **(Figure 3-6)**. These findings correlate to the results of µCT data especially the increment of cross-sectional thickness of femurs from *Trpv6*$^{mt/mt}$ and *Trpc1*$^{-/-}$/*Trpv6*$^{mt/mt}$ mice compared to wild-type mice **(Figure 3-4A)**.

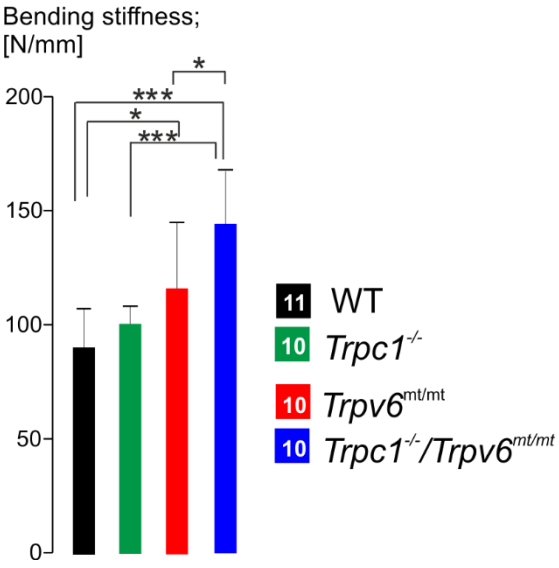

Figure 3-6 Bending stiffness of intact femurs from 24-week-old wild-type, *Trpc1*$^{-/-}$, *Trpv6*$^{mt/mt}$ and double mutant *Trpc1*$^{-/-}$/*Trpv6*$^{mt/mt}$ male mice. Bending stiffness (N/mm) was analyzed by a non-destructive three-point bending test. Data shown as mean ± SD, calculated by one-way ANOVA followed by Bonferroni multiple comparison test (p-value summary, $p<0.05$ *, $p<0.001$ ***). The colored bars represent four different genotypes: wild-type (black), *Trpc1*$^{-/-}$ (green), *Trpv6*$^{mt/mt}$(red) and *Trpc1*$^{-/-}$/*Trpv6*$^{mt/mt}$ (blue) with the number of animals for each group indicated in the colored square.

In conclusion, we observed greatest resistance against the gradually applied force by the bones from *Trpc1*$^{-/-}$/*Trpv6*$^{mt/mt}$ mice in comparison to the other genotypes. We also determined the bending stiffness of fractured femurs of four different genotype mice after explanting the screw. However, no significant difference in bending stiffness was observed between all four groups **(**supplementary **Figure 6-3)**.

3.3 Primary osteoclasts culture

The µCT data revealed a reduced trabecular bone volume fraction in femurs of TRPC1 deficient mice **(Figure 3-4B)** which prompted us to investigate the role of *Trpc1* at the cellular level in

primary osteoclasts culture. Up to this aim, I established the differentiation and culture of osteoclasts from bone marrow derived cells. After flushing out, the bone marrow cells were differentiated in the presence of M-CSF and RANK-L. **Figure 3-7A** shows differentiating osteoclasts at day two (D2) until day eight (D8), at which largely poly-nucleated osteoclasts are present. *Trpc1*-transcripts are present during differentiation and in mature osteoclasts **(Figure 3-7B)**. I also identified transcripts of other members of *Trpc* subfamily in mature osteoclasts **(Figure 3-7C)** with the exception of *Trpc5***.** My colleague Kai-Markus Busch showed that *Trpc1* transcripts also present in osteoblasts, outgrown from bone slices **(**supplementary **Figure 6-7)**.

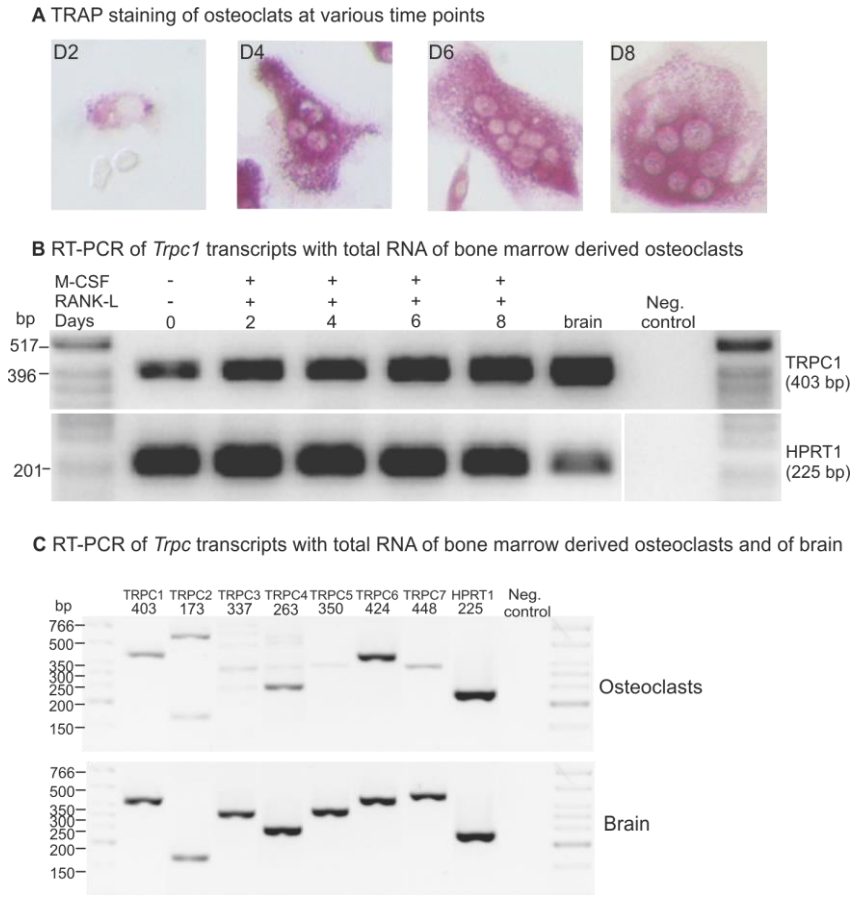

Figure 3-7 Differentiation of primary mouse osteoclast. (A) Representative images of tartrate resistant acid-phosphatase (TRAP) stained precursors (day 2 and 4), and matured multinucleated osteoclasts (day 6 and 8), **(B)** RT-PCR of *Trpc1* transcripts with total RNA isolated from M-CSF and RANK-L untreated (day 0) or M-CSF and RANK-L treated (day 2, 4, 6 and 8) bone marrow-derived cells, mRNA from brain served as a control, *Hprt1* was amplified as a positive control and water was used a negative control, **(C)** RT-PCR of *Trpc* transcripts with total RNA isolated from matured multinucleated osteoclasts (top), and from brain (bottom); negative control as in (B). (Figure 3-7C is also part of the supplement Figure 6-7B.)

The TRAP staining experiments showed significantly reduced osteoclasts number in the culture from bone marrow derived cells form *Trpc1*$^{-/-}$ mice as compared to wild-type mice **(Figure 3-8A, B)** although the same number of cells were seeded *i.e.* 1x10^5 cells per well of 96-well plate. This result suggested that *in vitro* osteoclasts differentiation is impaired in *Trpc1*$^{-/-}$ mice. Using a von Kossa staining, we observed significantly reduced number of resorption pits, formed by the osteoclasts derived from *Trpc1*$^{-/-}$ mice **(Figure 3-8C, D)** complying with our TRAP staining results. These experiments were performed together with my colleague Kai-Markus Busch.

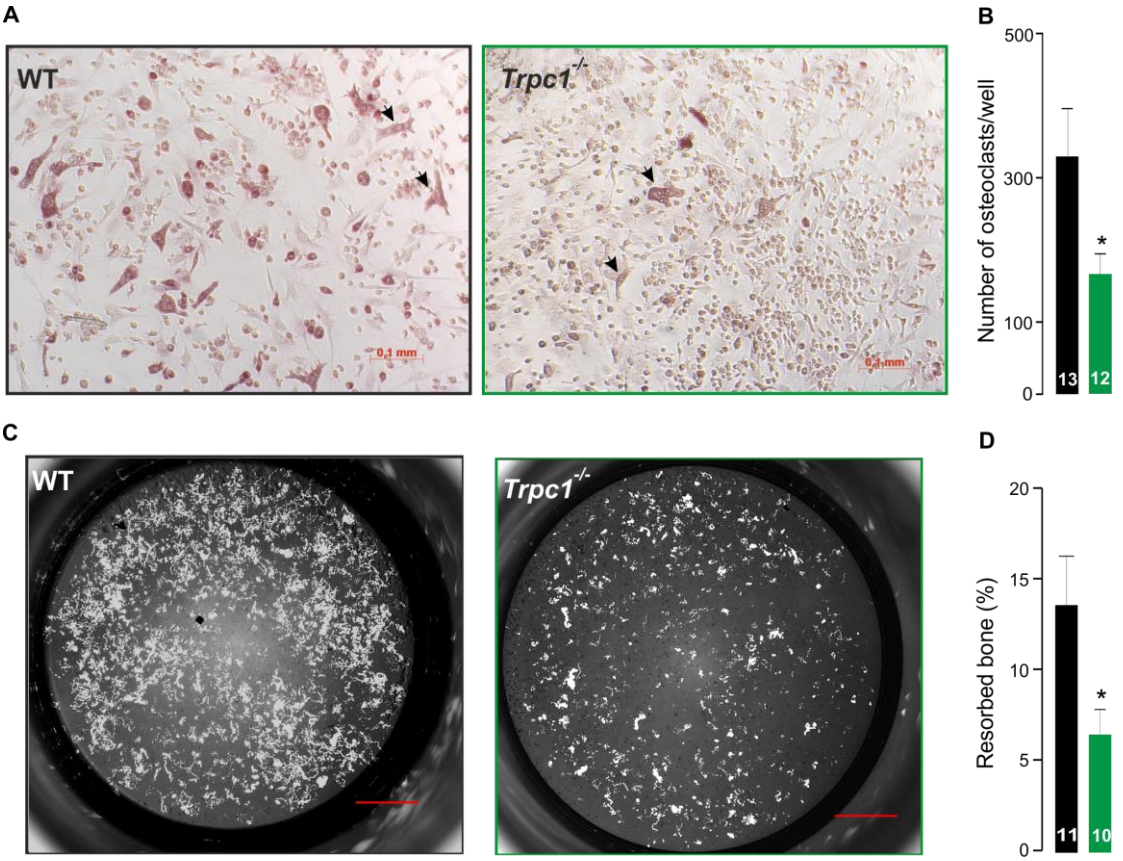

Figure 3-8 Primary osteoclast culture. (A) Representative images of TRAP-positive multinucleated osteoclasts differentiated from bone marrow cells of wild-type (left panel) and *Trpc1*$^{-/-}$ (right panel) mice, black arrows indicate examples of the multinucleated osteoclasts, scale bar = 0.1 mm. **(B)** Bar graphs indicate the number of osteoclasts in each well as mean ± SEM, with three wells per mouse from 13 mice (WT, black) and three wells per mouse from 12 mice (*Trpc1*$^{-/-}$, green). **(C)** Representative images of von Kossa stained bone (black) showing resorbed surface (white) by the activity of differentiated osteoclasts of wild-type (left panel) and *Trpc1*$^{-/-}$ (right panel) mice, scale bar = 1 mm. **(D)** Bar graphs indicate the percentage of resorbed bone in each well as mean ± SEM, with three wells per mouse from 11 mice (WT, black) and three wells per mouse from 10 mice (*Trpc1*$^{-/-}$, green), significance was calculated by two-tailed unpaired student's t-test ($p<0.05$ *).

3.4 Generation of a *Trpc1*-IRES-Cre (*Trpc1*-IC) mouse strain

In previous studies, it has been hypothesized that *Trpc1* transcripts are ubiquitously expressed (Zhu *et al.,* 1995), (Nilius and Flockerzi, 2014a, b), (Wes *et al.*, 1995). However, it has always been very challenging to test this hypothesis because of the following reasons. There is a lack of appropriate antibodies to detect TRPC1 protein by immunohistochemistry and no reliable TRPC1 ion currents have been measured by patch clamp recordings. To overcome these difficulties and to effectively visualize and manipulate *Trpc1*-expressing cells throughout the body in mice, a *Trpc1*-specific Cre recombinase knock-in (KI) mouse strain had to be generated.

3.4.1 Strategy for the generation of a *Trpc1*-IC mouse strain

In order to generate the *Trpc1*-IRES-Cre recombinase KI mouse strain (*Trpc1*-IRES-Cre or TRPC1-IC) an "IRES-Cre recombinase-FRT site-neo-FRT site cassette" had to be inserted just downstream to the STOP codon by gene targeting. The presence of the IRES-DNA sequence downstream the STOP codon should allow generating a bicistronic mRNA under the control of the endogenous *Trpc1* promoter **(Figure 3-9)**.

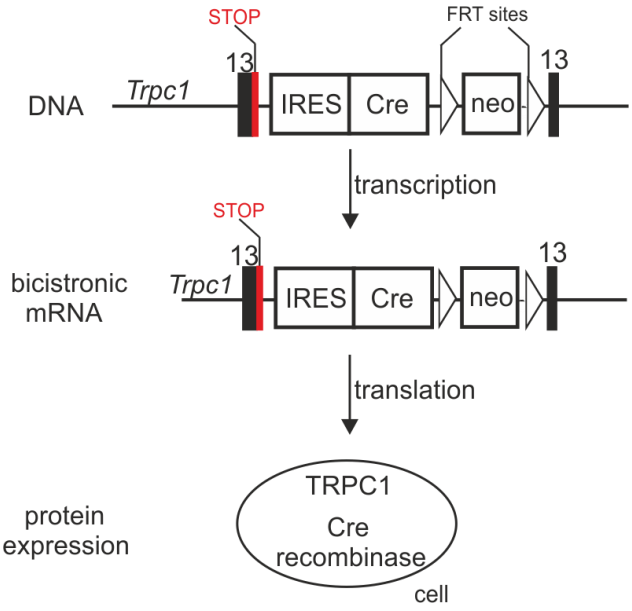

Figure 3-9 Strategy for the generation of a *Trpc1*-IC mouse strain. By homologous recombination the "IRES-Cre recombinase (Cre)-FRT-neo-FRT cassette" is introduced 3' of the STOP codon in the last protein coding exon 13 of the *Trpc1* gene. It transcribes into bicistronic messenger RNA (mRNA), which upon translation yields two independent proteins *i.e*. TRPC1 and Cre-recombinase within the same cell. (Black bars depict exon 13, not in scale, unfilled triangles represent *FRT* site).

These TRPC1-IC mice have to be bred with, for example, eROSA26-τGFP reporter mice. The litters obtained from this breeding, TRPC1-IC/eR26-τGFP animals, will have constitutive τGFP expression in *Trpc1*-expressing cells: The Cre-recombinase, co-expressed with *Trpc1*, will lead to excision of the floxed transcriptional termination signal (STOP cassette). As a result, eROSA26-τGFP-driven transcription of τGFP (or other reporters, depending on the type of reporter mouse) will occur in TRPC1-IC/eR26-τGFP double KI mice **(Figure 3-10)**.

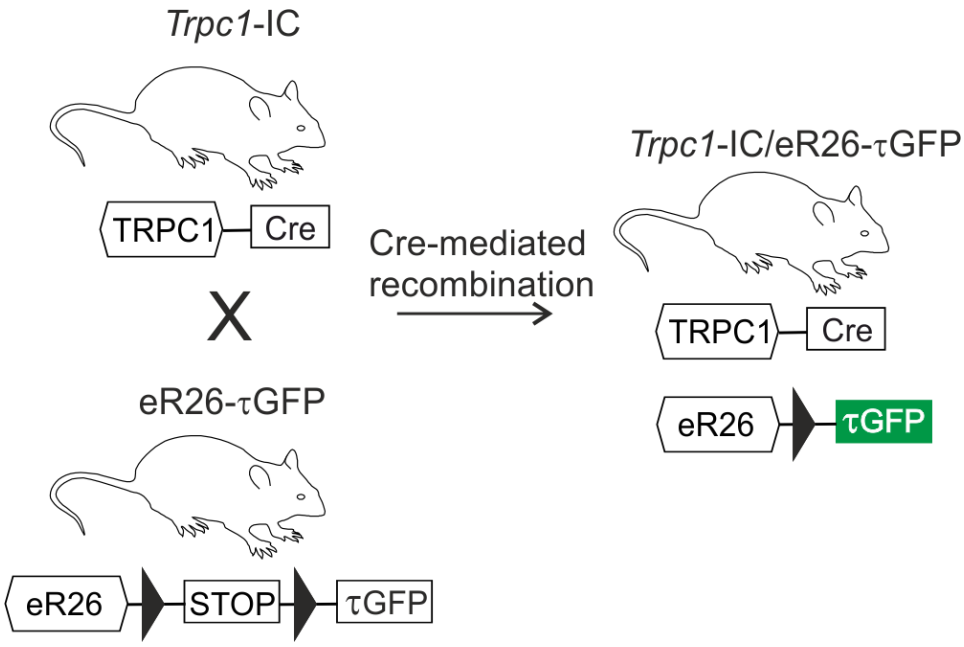

Figure 3-10 Breeding strategy to genetically label *Trpc1*-expressing cells. Breeding of *Trpc1*-IC mice with the eR26-τGFP reporter mouse strain will lead to excision of the floxed transcriptional termination signal (STOP) cassette, which in turn will activate eROSA26-driven transcription of τGFP in *Trpc1*-IC/eR26-τGFP double knock-in mice. (Filled triangles represent *loxP* site). The eR26-τGFP mouse strain was generated (Wen *et al.*, 2011) and generously provided by Prof. Dr. Ulrich Boehm (FR 2.4, Homburg).

3.4.2 Cloning strategy to generate *Trpc1*-IC targeting vector

The *Trpc1*-IC targeting construct (pAR_11, 12939 bp) is composed of a 5' *Trpc1* homology arm followed by an IRES-Cre recombinase cDNA-phosphoglycerate kinase (pgk) promotor driven-*FRT* site-neomycin resistance gene (neo)-*FRT* site cassette- and a 3' *Trpc1* homology arm **(Figure 3-11)**. First, the *Trpc1* gene organization and sequence was obtained from the Ensemble genome browser. The 5' (3254 bp) and 3' (2387 bp) homology regions derived from the *Trpc1* gene from C57BL/6J mice (Gen Bank: AC091531.9, C57BL/6J) were determined,

synthesized and cloned into the pUC18 by Biomatik (Ontario, Canada) to yield plasmids pAR_7 and pAR_6 **(Figure 3-11A)**. The AgeI-NotI 5' homology region (5' Hom) from pAR_7 was subcloned into the AgeI-NotI cut plasmid pAR_6 to yield pAR_8 (8320 bp) **(Figure 3-11B)**. The AscI fragment obtained from plasmid pKO-ICF comprising of splice acceptor IRES-Cre recombinase-phosphoglycerate kinase promotor-driven *FRT*-neomycin resistance-*FRT* cassette was subcloned into AscI cut pAR_8 to yield pAR_9 (11763 bp) **(Figure 3-11C)**. The cassette was inserted 23 nucleotides downstream to the STOP codon of *Trpc1*.

The 'neo' cassette was added as a positive selection marker used for the identification/selection of ES cell clones having integrated targeting construct. In the presence of geneticin only those cells survive which carry the neomycin resistance gene, that is the gene of aminoglycoside phosphotransferase. Geneticin (abbreviated as G418) inhibits protein synthesis and kills eukaryotic cells. The aminoglycoside phosphotransferase phosphorylates HO-groups of G418 thereby inactivating G418 allowing survival of these cells carrying the resistance gene. Finally, phosphoglycerate kinase (pgk)-promoter driven diphtheria toxin A fragment (DTA) cassette was subcloned downstream to the 3' homology: To generate blunt-ended DNA the RsrII cDNA fragment encoding the cassette, DTA, from plasmid pKOselect DTV840 and the NotI cut plasmid pAR_9 were incubated in the presence of T4 DNA polymerase, dNTPs and the blunt-ended DNAs were ligated to obtain pAR_11, the final targeting vector (12939 bp) **(Figure 3-11D)**. The DTA was added to the plasmid as a negative selection marker to ensure the selection of ES cell clones with correctly integrated DNA. In case the targeting construct is randomly integrated, DTA fragment will be translated and kill the cells (Yagi *et al.,* 1993).

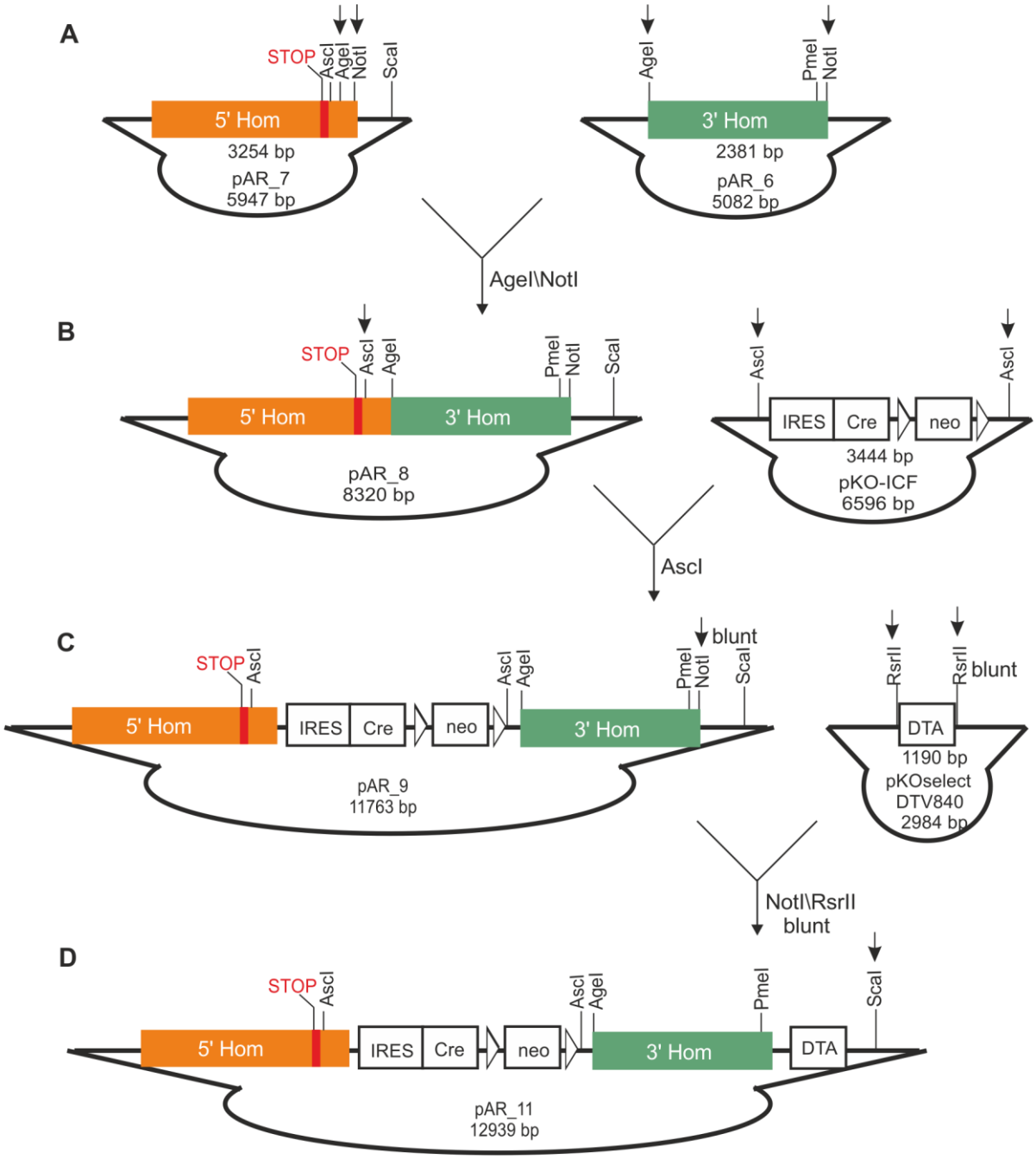

Figure 3-11 Cloning strategy for the generation of *Trpc1*-IC targeting vector. (A) The vectors pAR_7 (5947 bp) and pAR_6 (5082 bp) depicts 5' homology along with the stop codon and 3'homology regions, respectively. The fragment 3' homology arm (2381 bp) is prepared from the vector pAR_6 by the restriction enzymes AgeI and NotI and subcloned into AgeI/NotI cut vector pAR_7 yielding vector pAR_8 (8320 bp) **(B)** Internal ribosome entry site (IRES)-Cre recombinase cDNA (Cre)-pgk promotor-driven Flp recombination target (*FRT*) site-neomycin resistance gene (neo)- *FRT* cassette (3444 bp) is prepared from the vector pKO-ICF (6596 bp) by the restriction enzyme AscI and subcloned into the AscI cut vector pAR_8 downstream of the stop codon yielding vector pAR_9 (11763 bp) **(C)** The Diptheria toxin A (DTA) fragment (1190 bp) is isolated from the vector pKOselect DTV840 (2984 bp) by the enzyme RsrII, blunted and inserted into the vector pAR_9 at the blunted NotI site yielding a vector pAR_11 (12939

bp) **(D)** The final targeting construct pAR_11 is linearized by the restriction enzyme ScaI. Black arrows highlight the approximate location of restriction enzymes required in specific cloning steps. Location of enzymes is determined by the software Accelrys Gene v2.5. Unfilled triangles represent *FRT* sites.

The correctness of pAR_11 was confirmed by restriction enzyme cuts followed by agarose gel electrophoresis and by nucleotide sequencing on both strands. The pAR_11 was linearized with ScaI **(Figure 3-12)**, sent to *iTL* (*ingenious* Targeting Laboratory, Ronkonkoma, New York, USA) and electroporated there into C57BL/6 ES cells. The representative agarose gel images of individual cloning steps are shown in the supplementary **Figure 6-4**. The vectors pKO-ICF and pKOselect DTV840 were generously provided by Prof. Dr. Ulrich Boehm (FR 2.4, Homburg) and Prof. Dr. Thomas Jentsch (MDC/ FMP, Berlin), respectively.

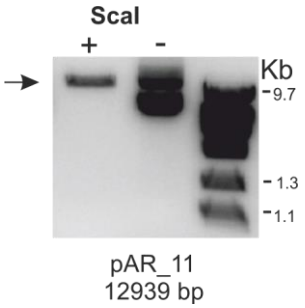

Figure 3-12 Linearized final targeting plasmid, pAR_11. Agarose gel electrophoresis of pAR_11 cut by ScaI (+) and non-cut super-coiled DNA (-), marker was applied on the right lane.

3.4.3 Identification of precisely integrated ES cell clones by Southern blotting

The linearized targeting construct 'pAR_11' was electroporated into C57BL/6 ES. The 5' and 3' homology regions of the targeting construct allow integration at the *Trpc1* gene locus by homologous recombination. After selection with G418 and DTA a total number of 288 ES cell colonies were isolated by *iTL* and lyophilized replicas sent to Homburg for Southern blotting. For the identification of correctly integrated ES cell clones, a Southern blot strategy was established based on three probes, the 5'-probe and the 3'-probe, both probes located outside of the homology regions, and the neo-probe, present within the targeting construct **(Figure 3-13A)**. Initially, I checked 128 ES cell clones by the 5'-probe and 93 clones were found to be positive *i.e*. heterozygous for the mutation, carrying both wild-type and mutant alleles.

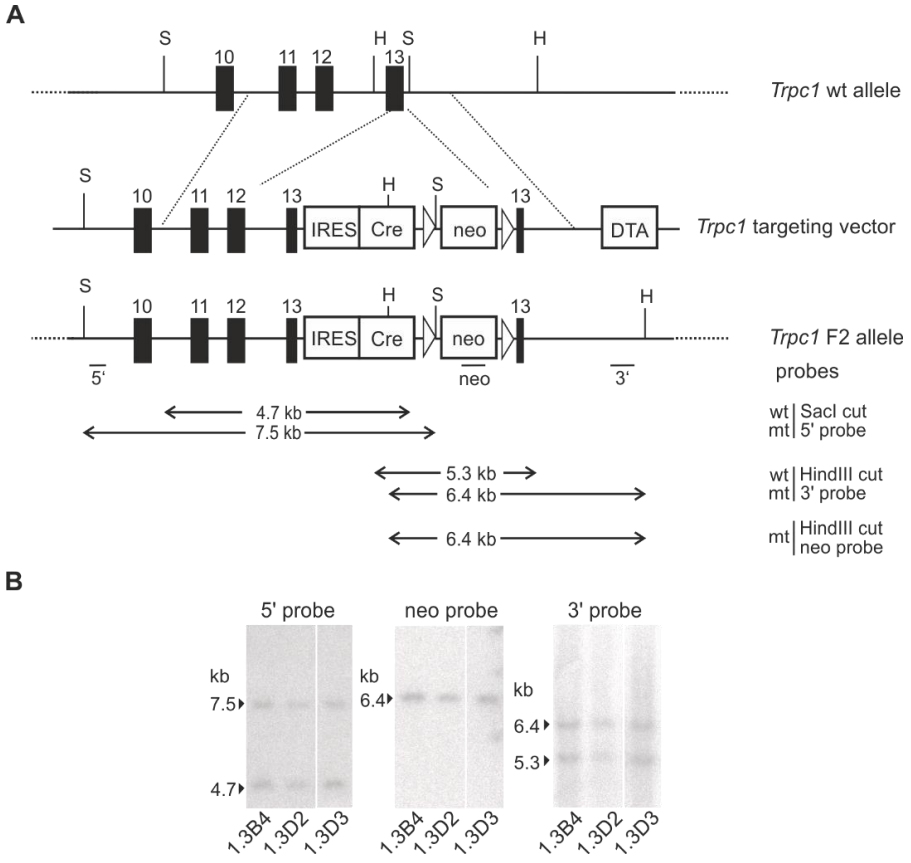

Figure 3-13 Southern blot analysis for the selection of precisely integrated ES cell clones. (A) Southern strategy: from top to bottom, *Trpc1*-wt allele, *Trpc1*-targeting vector and targeted recombination of the *Trpc1* locus (F2 allele) indicated. Translated exons (not in scale) are shown as black boxes. The targeting vector is composed of an internal ribosome entry site (IRES) element followed by a Cre, the coding sequence of Cre recombinase and a neomycin resistance gene (neo) cassette flanked by *FRT,* the Flippase recombination target sites (unfilled triangles) has been inserted after the stop codon present within exon 13. Dotted lines in between the wt allele and targeting vector represent the region of homologous recombination. The sites for restriction enzymes (S, SacI, H, HindIII) and location of 5'-, neo- and 3'-probes used for Southern blot hybridization are indicated. The predicted fragment sizes in both wt and mt alleles are shown by the arrows. **(B)** Southern blot: Representative images indicate the expected bands in the genomic DNA cut by SacI (5' probe) and HindIII (neo and 3'probes) from three independent recombinant *Trpc1*-IC ES-cell clones (clone numbers 1.3B4, 1.3D2 and 1.3D3) using 5'-, neo- and 3'-probes. All representative three ES cell clones show *Trpc1*-wt and -mt alleles.

Thus, the calculated recombination efficiency was approximately 73%. The 5'-probe labelled SacI fragments of genomic ES cell DNA of 4.7 Kb and 7.5 Kb in wt and mt alleles respectively. Thirty-two clones out of those 93 were tested with both the 3'-probe and the neo-probe. The 3'-probe labelled HindIII fragment of 5.3 Kb in the wild-type and 6.4 Kb in the mutant allele. The internal neo probe labelled a single 6.4 Kb HindIII fragment, confirming that the targeting

construct is integrated only once within the genome **(Figure 3-13B)**. Twenty-seven out of 32 clones were found to be positive. All three probes confirmed precise integration of the targeting construct at the *Trpc1* locus by homologous recombination. Five out of 27 were selected, expanded and karyotyped for chromosome count analysis **(Table 3-3)**.

Sr. #	Clone numbers	Euploid karyotype (%)
1	1.3B2	78
2	1.3B4	77
3	1.3D2	100
4	1.3D3	86
5	1.3E4	75

Table 3-3 Chromosome count performed by *iTL* (karyotype result) for five selected ES cell clones for the generation of *Trpc1*-IC KI mouse strain.

3.4.4 Identification of *Trpc1*-IC mice by PCR based genotyping

Three ES cell clones (clone numbers 1.3D2, 1.3B4 and 1.3B2) out of five selected based on their karyogram were injected into BALB/c blastocysts. The summary of injections performed in Interfakultäre Biomedizinische Forschungseinrichtung (IBF) Heidelberg University and *iTL* (USA) is given in the supplementary section **(Table 6-6)**. Subsequently these blastocysts were implanted into the uterus of pseudopregnant C57BL/6 foster mothers. All three implantations resulted in eight chimeras. These pups were the F0 generation. All chimeras were derived from clone 1.3B4. The percentage of chimerism in F0 progeny was estimated based on coat color distribution. The success of a gene targeting depends on the maintenance of a mutant allele in the gametes (sperms or eggs) *i.e.* germline transmission. In this way, the mutation can be transmitted over generations. Therefore, the next step was to backcross the highly chimeric animals with C57BL6/N wild-type mice to check if the mutant allele has been inherited. The presence of the F2 allele in the offspring from chimera was tested by PCR based genotyping using specific primers amplifying the locus of integration within exon 13 and the *FRT* sites **(Figure 3-14B)**. Our results showed the presence of heterozygous mice in F1 generation.

Images of selected heterozygous mice are shown in **Figure 3-15**. They are viable, healthy and show no obvious abnormalities. One of the three ES-cell (1.3B4) derived mouse lines was used for further experiments.

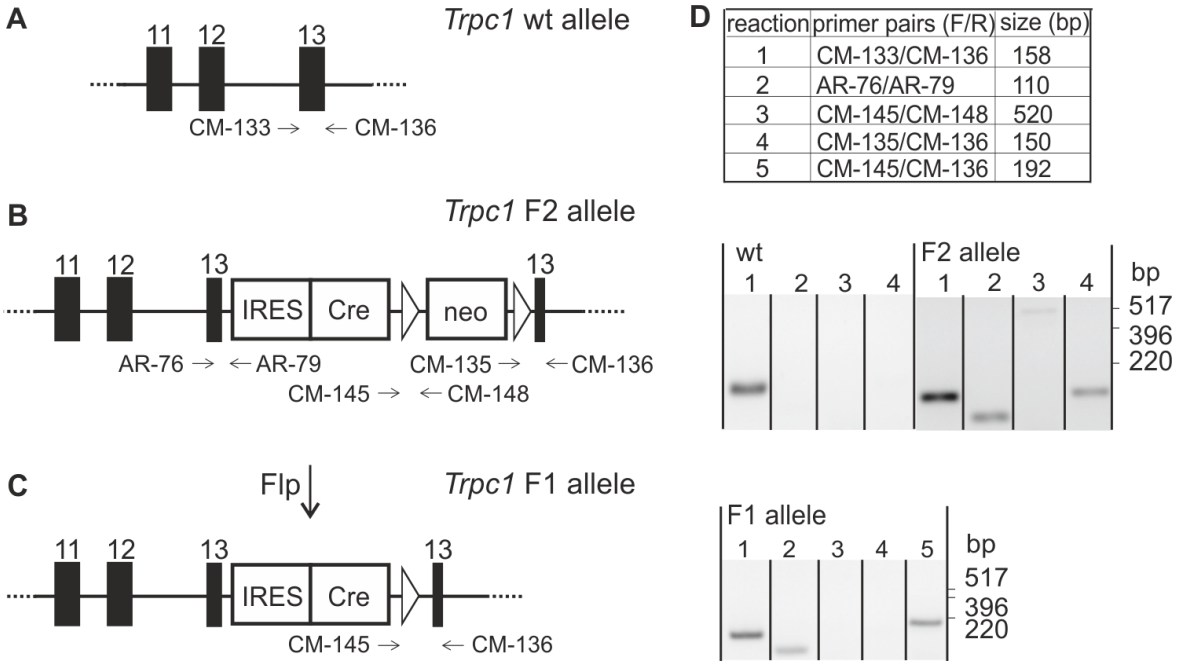

reaction	primer pairs (F/R)	size (bp)
1	CM-133/CM-136	158
2	AR-76/AR-79	110
3	CM-145/CM-148	520
4	CM-135/CM-136	150
5	CM-145/CM-136	192

Figure 3-14 Genotyping strategy to follow successful recombination. Schematic representation of the genotyping strategy: **(A)** *Trpc1* wt allele shows three exons (11-13), filled boxes, not in scale, approximate location of primer combination is shown spanning over the exon 13 to identify the wt allele by PCR, **(B)** *Trpc1* F2 allele, (F2 because of two FRT sites (open triangles)) contains the IRES-Cre-neomycin resistance cassette, neo, flanked by two *FRT* sites inserted after the stop codon in the middle of exon 13. Arrows indicate position of forward and reverse primers used for PCR, **(C)** *Trpc1* F1 allele obtained upon Flp-mediated excision shows IRES-Cre and the single remaining *FRT* site, **(D)** table (top) shows the forward (F) and reverse (R) primer combinations used for the PCR reactions 1 to 5 along with the expected fragment sizes (bp). Representative agarose gel images (middle and bottom) show the PCR based genotyping results for the identification of mice carrying wt, F2 and F1 alleles. Numbers indicate PCR reaction from the table.

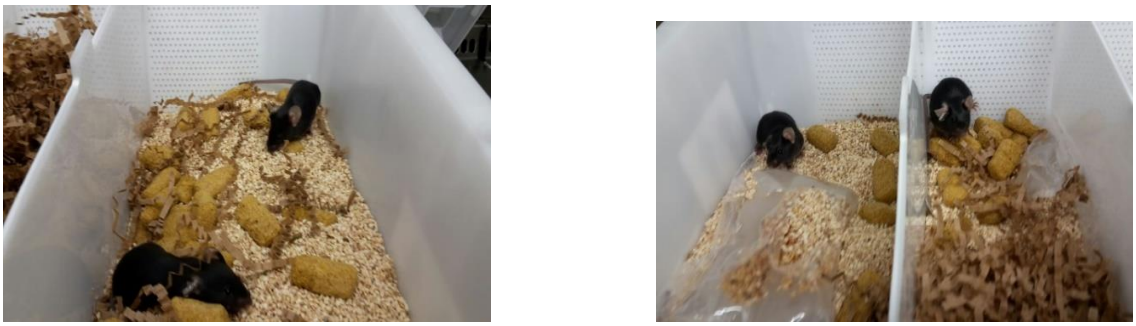

Figure 3-15 *Trpc1*-IC heterozygous mice in F1 generation. Representative images show female (left) and male (right) heterozygous mice identified by genotyping PCR. All mice resulted from the injection of ES cell clone number 1.3B4 into Balb/c blastocysts subsequently implanted in C57BL/6 foster mothers.

Previous studies have shown that the neo cassette contains cryptic splice sites and thus its presence within the genome could interfere with the expression of neighboring genes (Meyers *et al.,* 1998). Therefore, the neo cassette has to be removed once the targeting construct is successfully integrated within the endogenous DNA sequence to avoid a possible hypomorphic allele (Jacks *et al.,* 1994). In our targeting plasmid, the neo cassette is flanked by *FRT* sites. Mice carrying the F2 allele **(Figure 3-14B)** were bred with Flp deleter mice, ubiquitously expressing Flpe recombinase as a transgene (Dymecki, 1996). The resultant pups were genotyped using PCR primers to confirm the deletion of the neo cassette, in terms of the targeting construct recombination results in the *Trpc1* F1 allele or *Trpc1*-IRES-Cre-neo^{-} allele **(Figure 3-14C)**. In terms of mice, the new *Trpc1*-IRES-Cre strain is also dubbed as "*Trpc1*-IC".

Currently, the breeding of *Trpc1*-IC mouse strain is successfully operational in our animal facility. Homozygous pups born are healthy, fertile and without any obvious phenotypic abnormalities. These animals can now be crossed with one of eROSA26-reporter mouse strains provided by Prof. Dr. Ulrich Boehm (FR 2.4, Homburg) in order to manipulate or to visualize *Trpc1*-expressing cells. **(Figure 3-10)** shows the breeding scheme with the eROSA26-τGFP reporter strain (Wen *et al.*, 2011) yielding *Trpc1*-IC/eR26-τGFP mice, with constitutive τGFP expression in *Trpc1* expressing cells. Experiments performed on the pituitary, obtained from *Trpc1*-IC/eR26-τGFP mice by my colleague Dr. Hongmei Wang, enabled us to visualize the TRPC1 expression pattern in pituitary cells and to specifically characterize the *Trpc1*-expressing cells (manuscript submitted).

3.5 Generation of a conditional *Trpc1* mouse strain

In the year 2007, Alexander Dietrich *et al.* reported the generation of a *Trpc1* global KO mouse model and until present, it has been extensively studied to characterize the role of TRPC1 in various organs (Dietrich *et al.,* 2007). However, using a *Trpc1* conventional KO mouse strain, it is quite challenging to explain the cell- or tissue-specific role of *Trpc1.* Thus, in order to determine the specific role of *Trpc1* in any desired cell type or any organ such as bone cells or bone, I have generated a mouse line carrying a conditional *Trpc1* allele, which could be bred with any cell/tissue-specific Cre-recombinase mouse strain to generate *Trpc1* deletion in a cell specific manner.

3.5.1 Strategy for the generation of a conditional *Trpc1* mouse strain

We developed a cloning strategy as outlined in the **(**supplementary **Figure 6-6)** for the generation of a conditional *Trpc1* mouse strain. The *loxP* sites should flank exon 8 and 9, which is part of the ion-conducting TRPC1 pore. The molecular biology techniques employed for getting the targeting construct are identical to those described above for the cloning of the targeting vector required to generate the *Trpc1*-IRES-Cre mouse strain. However, abundant repetitive DNA sequences prevented amplification of the 3' homology region. After several trials, I abandoned this targeting strategy.

Instead, we decided to use a targeting construct from EUCOMM (PG00239_Z_4_A03) with a floxed exon two of the *Trpc1* gene. In the mouse (*mus musculus*) genome, exon 2 of *Trpc1* transcript, *Trpc1*-204, (transcript ID ENSMUST00000189137.6) consists of a 155 bp long nucleotide sequence (5'upstream sequence, start:end, 95,743,351:95,743,197) as indicated in the Ensemble genome browser. Deletion of this particular exon would lead to a shift in the reading frame causing a premature termination during translation of the TRPC1 protein due to nonsense mutations.

We obtained the targeting construct, C1Z_21361 bp, from EUCOMM and had it sequenced on both strands. The targeting construct consists of 5' (5544 bp) and 3' (3616 bp) homology regions for the homologous recombination at the *Trpc1* gene locus in the mouse. The 5' homology arm was followed by a pair of consensus *FRT*-sites. The cassette has been inserted in between the *FRT*-sites consisting of splice acceptor (SA) site- IRES-(bacterial beta-galactosidase gene) *lacZ* cDNA, a polyadenylation (pA) signal site-a *loxP* site and a human beta

actin promoter-driver neo cassette. Exon two of *Trpc1* is flanked by *loxP* sites and DTA has been inserted as a negative selection marker **(Figure 3-16)**.

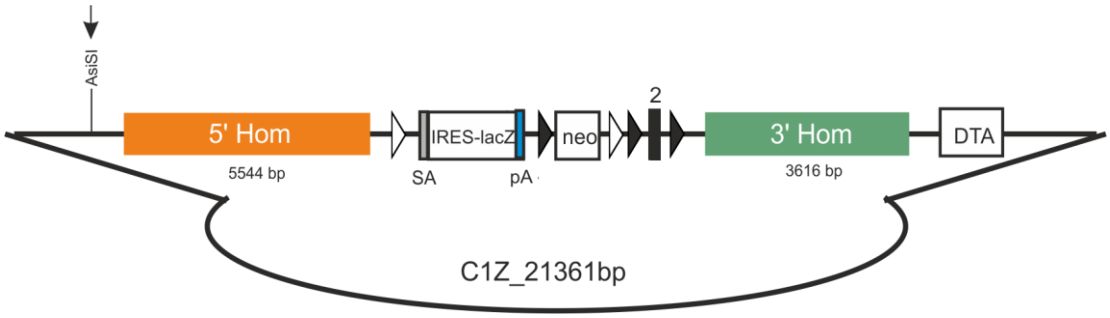

Figure 3-16 Targeting vector (EUCOMM; PG00239_Z_4_A03) for the generation of a conditional *Trpc1* mouse strain. The targeting vector, C1Z_21361 bp consists of 5' (5544 bp) and 3' (3616 bp) homology arms and in between flippase recombination target (*FRT*) site-splice acceptor (SA)- internal ribosome entry site (IRES)-*lacZ*-polyadenylation (pA) signal-*loxP* site-neo cassette-*FRT* is shown. The exon two is flanked by *loxP* sites. Diphtheria toxin A (DTA) is located downstream of the 3'homology arm. Approximate site of the restriction enzyme AsiSI is indicated by the arrow. Unfilled and filled triangles show *FRT* and *loxP* sites respectively.

This vector **(Figure 3-16** and **3-17)** was used for gene targeting in C57BL/6 ES cells to generate ES-cells heterozygous for the inserted mutation; the ES cells should carry the wild-type allele and the *Trpc1* L3F2 allele: L3 stands for three *loxP* sites, F2 stands for two *FRT* sites. By crossing L3F2 mice with Flp recombinase deleter mice, a *Trpc1* flox allele should be generated **(Figure 3-17B)**. In the floxed allele, exon two of the *Trpc1* gene is flanked by two *loxP* sites, within the second and third introns, respectively. Subsequent crossing of *Trpc1* flox mice with tissue specific Cre recombinase deleter mouse lines should lead to the deletion of exon two **(Figure 3-17C)**.

Using this targeting vector, the L3F2 allele can also be used to generate a *lacZ* reporter mouse strain. By crossing mice bearing *Trpc1* L3F2 allele with Cre recombinase deleter mice, a *Trpc1* KO IRES-*lacZ* allele can be generated which comprises of SA-IRES-*lacZ* cassette **(Figure 3-17D)**. By splicing, the IRES-*lacZ* sequence should be attached to the exon one of the *Trpc1* gene due to the presence of splice acceptor (SA) site. The IRES element leads to the formation of a bicistronic mRNA. The first mRNA encodes exon one which upon translation runs into a premature stop. The second mRNA encodes the β-galactosidase encoded by the *lacZ* gene. As transcription of the bicistronic mRNA is under the control of *Trpc1* promoter, the β-

galactosidase should be present only in cells originally expressing *Trpc1* and now lacking *Trpc1*. That means β-galactosidase enzyme activity can be used to identify *Trpc1*-KO cells by adding its substrate 'X-gal' and subsequent detection of blue coloration. By this strategy, we generate a complementary mouse strain to the *Trpc1*-IRES-Cre mouse. The *Trpc1*-IRES-Cre mouse can be bred with reporter strains such as eR26-τGFP in order to visualize *Trpc1*-expressing cells by τGFP **(Figure 3-10)**; with the "*lacZ*" strategy, we are able to visualize *Trpc1* KO cells.

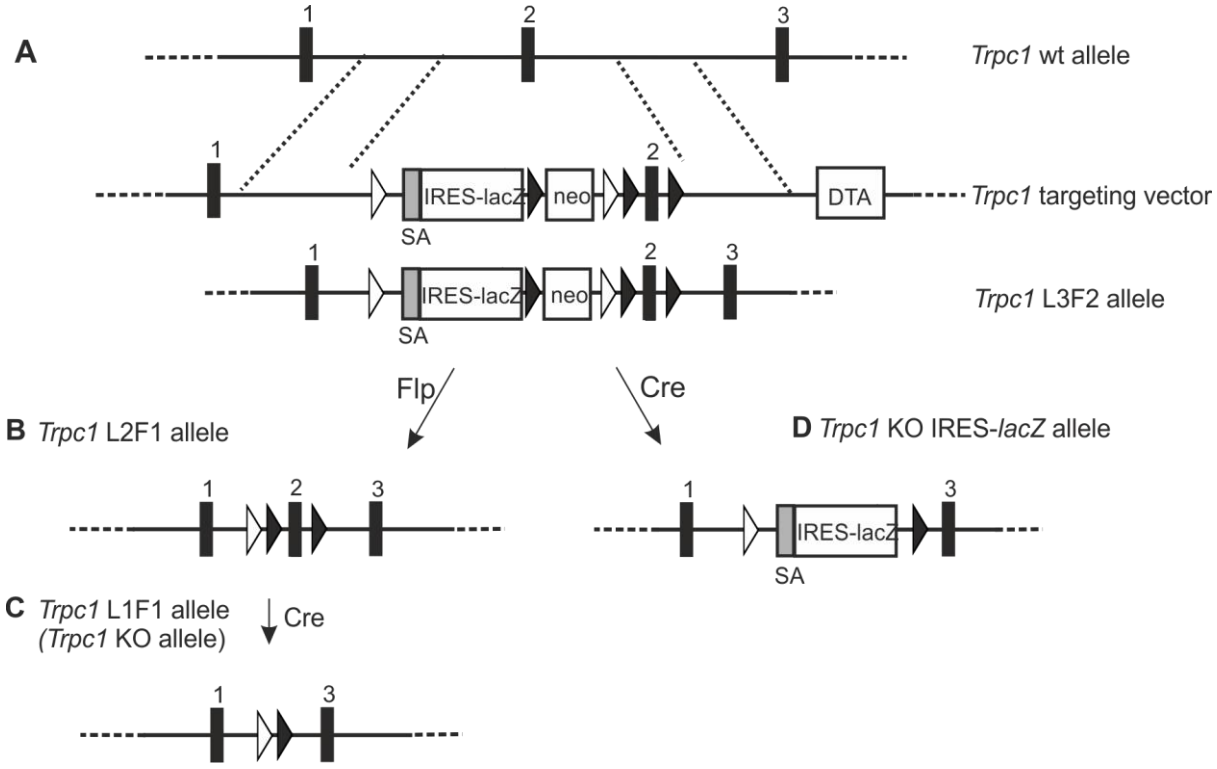

Figure 3-17 Targeting strategy for the generation of conditional *Trpc1* mouse strain. Schematic representation of a targeting strategy **(A)** *Trpc1*-wt allele, *Trpc1*-targeting vector and targeted recombination (L3F2 allele) indicated. Translated exons (not in scale) are shown as black boxes, dotted lines represent the region of homologous recombination. The targeting vector consists of consensus *FRT* sites (unfilled triangles), in between these sites SA-IRES-*lacZ*-*loxP* site-neo cassette is located, exon two flanked by *loxP* sites (filled triangles) is shown. Flp-mediated excision, left panel, will lead to **(B)** *Trpc1* L2F1 allele (L2 because of two *loxP* sites and F1 due to a single *FRT* site) consists of a *FRT* site downstream of the exon one and a floxed exon two, Cre-mediated excision of *Trpc1* L2F1 allele will lead to **(C)** *Trpc1* L1F1 (L1 because of one *loxP* sites and F1 due to of a single *FRT* site) or *Trpc1* KO allele contains *FRT* and *loxP* sites present in between exons one and three is indicated. **(D)** Cre-mediated excision of *Trpc1* L2F1 allele, right panel, will lead to *Trpc1* KO IRES-*lacZ* allele consists of a *FRT* site-SA-IRES-*lacZ*-*loxP* site cassette present in between exons one and three is shown.

3.5.2 Identification of correctly targeted ES cell clones by PCR and Southern blotting

The 'C1Z_21361 bp' targeting vector was confirmed by sequencing on both strands and then linearized by the restriction enzyme AsiSI **(Figure 3-18)**. The linearized plasmid was electroporated into the C57BL/6 ES cells by *ingenious* Targeting Laboratory (*iTL)*.

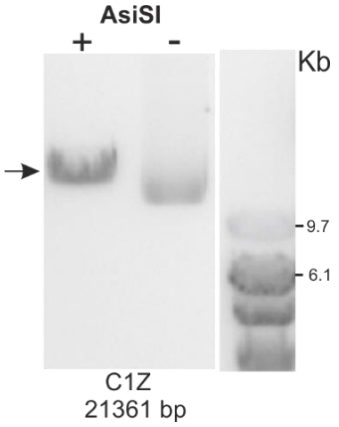

Figure 3-18 Linearized targeting construct, C1Z. The representative agarose gel image shows the plasmid C1Z, cut (+) by AsiSI and super-coiled non-cut (-). Arrow indicates the expected fragment size (21361 bp), size marker in kilo base pairs (Kb) is indicated.

A total number of 288 neomycin-resistant ES cell colonies were picked by *iTL* and sent to us for screening by PCR and Southern blotting. The targeting construct, C1Z, has three loxP sites and the exon two is flanked by the second and third *loxP* sites **(Figure 3-16)**. The third *loxP* site is located close to the 3' homology arm and thus there were greater chances of its loss during homologous recombination. Therefore, it was crucial to verify the insertion of the third *loxP* site into the target sequence. As Southern blotting is not an appropriate method for the detection of 34 bp *loxP* site in the mutant allele, I designed a PCR strategy with a primer combination, AR-74/AR-75, spanning over the third *loxP* site. Initially, I performed PCR on 96 ES cell clones and 88 clones were found positive *i.e.* showing both wt and mutant fragments **(Figure 3-19)**. The representative agarose gel **(Figure 3-19C)** shows a PCR result of a wild-type ES clone and a clone where the third *loxP* site is present. Out of 88 PCR-positive clones, I selected 32 ES cell clones for further Southern analysis.

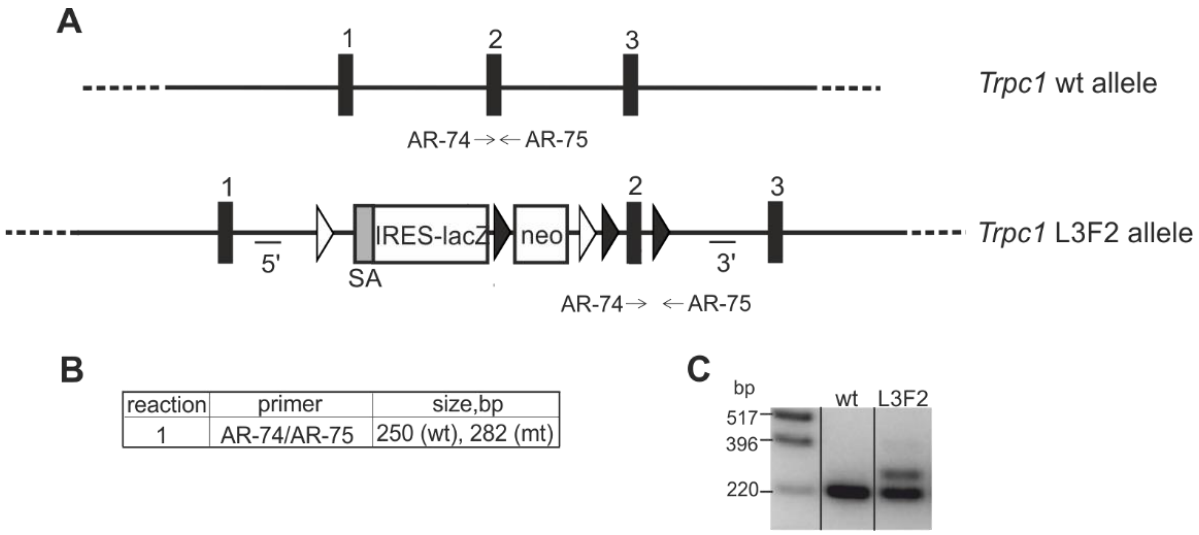

Figure 3-19 PCR strategy for the identification of third *loxP* site insertion in the mutant allele. **(A)** PCR strategy: top, *Trpc1* wt allele containing exons (black boxes), not in scale, and position of forward primer, AR-74 and reverse primer, AR-75; bottom, *Trpc1* L3F2 allele shows the targeting construct, present downstream of the exon one, containing Flippase recombination target (*FRT*) site-splice acceptor (SA)-internal ribosome entry site (IRES)-*lacZ*-*loxP* site-neo cassette-*FRT* site-consensus *loxP* sites. Forward primer, AR-74 and reverse primer, AR-75 spanning over third *loxP* site. Unfilled triangles show *FRT* sites while filled triangles depict *loxP* sites. **(B)** Table shows the expected band sizes in wt and L3F2 alleles obtained by PCR using primers AR-74 and AR-75. **(C)** Representative agarose gel image shows a single band (250 bp) in wt allele, representing the two wt alleles and two bands (250 and 282 bp) in L3F2 allele, representing one wt and one mutant allele both differing in the *loxP* site present in the mutant allele.

In order to identify correctly recombined ES cell clones, I designed a Southern strategy based on three probes namely a 5'-, and a 3'-probe, both external to the targeted sequence and an internal neo'-probe, present within the targeting construct showing singular integration of the targeting vector in the ES cell genome **(Figure 3-20)**. Thirty-two ES cell clones positive for the third *loxP* site were analyzed with all three probes by Southern blot. The 5'-probe hybridized to a 16.2 Kb band and a 13.9 Kb band in StuI cut DNA respectively, the expected DNA fragments from the wild-type allele and the mutant allele **(Figure 3-20B)**. The 3'-probe hybridized to PflMI cut DNA with 6.4 Kb and 9.7 Kb band sizes in wt and mt alleles respectively. The internal probe, neo-, hybridized to PflMI cut DNA; the size of the band was 9.7 Kb indicating singular integration into the L3F2 allele.

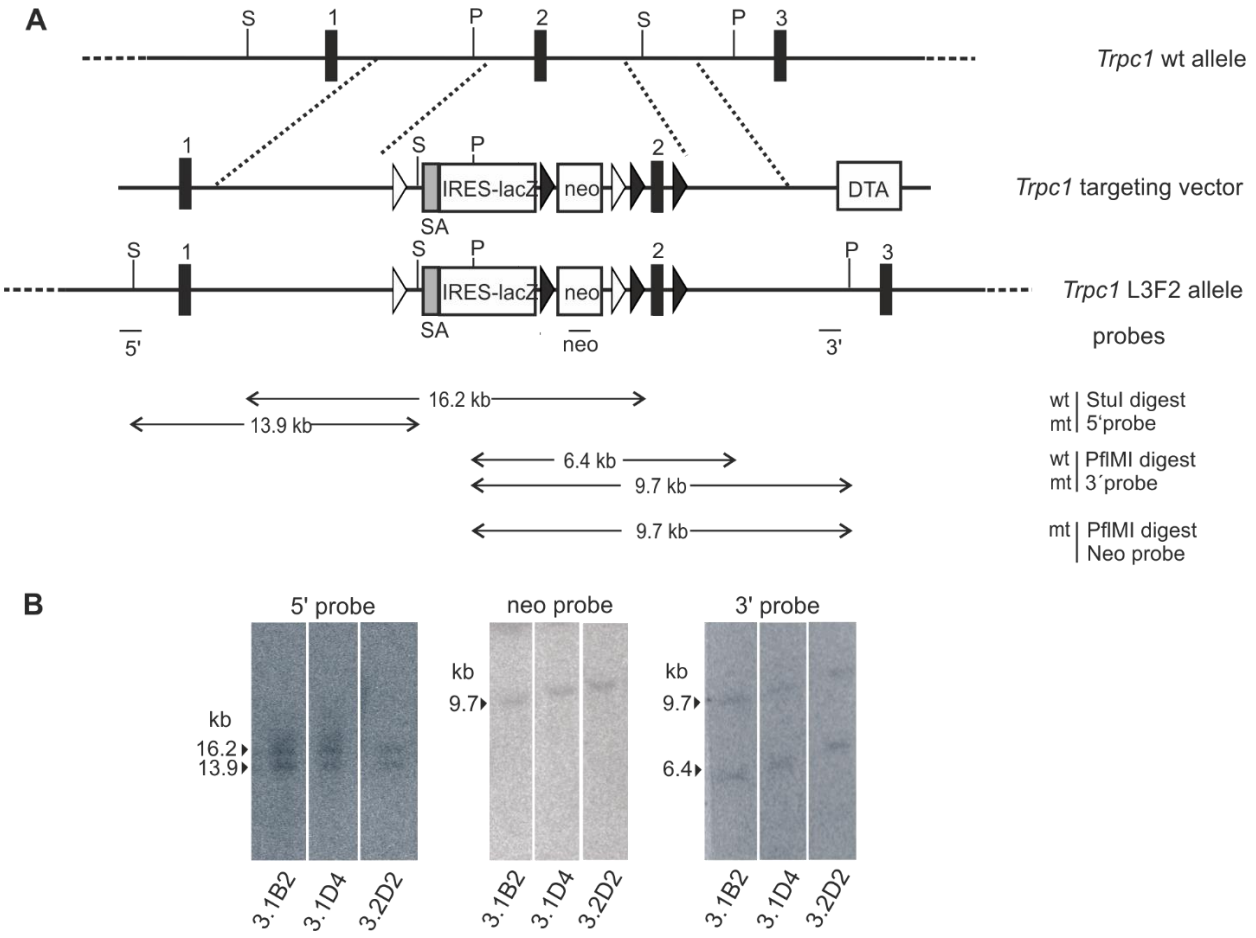

Figure 3-20 Southern blot analysis for the generation of a conditional *Trpc1* mouse strain. (A) Southern strategy: from top to bottom, *Trpc1*- wt allele, *Trpc1*-targeting vector and targeted recombination (L3F2 allele) indicated. Translated exons (not in scale) are shown as black boxes. The targeting vector is composed of 5' homology arm followed by a pair of consensus Flippase recombination target (*FRT*) sites. The cassette inserted in between the *FRT* sites consists of splice acceptor (SA) site-internal ribosome entry site (IRES)-*lacZ* cDNA-*loxP* site and a neomycin resistance gene cassette (neo). Exon two of the *Trpc1* gene is flanked by *loxP* sites and diphtheria toxin A (DTA) as a negative selection marker is shown**.** Dotted lines in between the wt allele and targeting vector represent the regions of homologous recombination. Restriction enzyme sites (S, StuI, P, PflMI) and location of 5'-, neo- and 3'-probes used for Southern blot hybridization are indicated. The predicted fragment sizes in both wt and mt alleles are shown by the arrows. **(B)** Southern blot: Representative images indicate expected bands in the genomic DNA cut by StuI (5'probe) and PflMI (3' and neo probe) from three independent recombinant *Trpc1* ES-cell clones (clone numbers 3.1B2, 3.1D4 and 3.2D2) using 5'-, neo- and 3'-probes. All representative three ES cell clones show *Trpc1*-wt and -mt alleles.

Twenty-four ES cell clones out of 32 were positive with all three probes and six out of those were finally selected for expansion and karyotyping analysis at *iTL* **(Table 3-4)**.

Sr. #	Clone numbers	Euploid karyotype (%)
1	3.1B2	71
2	3.1D3	86
3	3.1D4	75
4	3.2A1	79
5	3.2D2	85
6	3.2D3	86

Table 3-4 Chromosome count performed by *iTL* (karyotype result) for selected six ES cell clones for the generation of the conditional *Trpc1* KO mouse strain.

3.5.3 Identification of *Trpc1*-L3F2 mice by PCR based genotyping

Five out of six ES cell clones, selected on the basis of PCR, Southern and karyogram analyses, were injected into BALB/c blastocysts, and subsequently transplanted into the uterus of C57BL/6 pseudopregnant foster mothers. The summary of injections performed in Interfakultäre Biomedizinische Forschungseinrichtung (IBF) Heidelberg University or *iTL* (USA) is given in the supplementary section **(Table 6-7)**. Only two out of five implanted ES cell clones (clone numbers 3.1D4, 3.2D2) resulted into chimeric progeny **(Figure 3-21)**.

Figure 3-21 Chimeric mice. Representative images show the chimeric progeny resulted from the injection of *Trpc1*-floxed allele positive-ES cell clone number 3.2D2 (left) and 3.1D4 (right).

The percentage of chimerism was estimated based on coat color distribution. Brown/black coat color derives from the mutant ES cells and white coat color from the Balb/c blastocysts. Highly chimeric mice derived from two independent ES cell clones were bred with C57BL/6 WT mice yielded the F1 progeny. The next step was to differentiate between the WT and heterozygous pups. Therefore, a genotyping strategy was designed using various primer combinations spanning different elements of the inserted targeting construct as outlined in

(Figure 3-22A). A representative agarose gel image **(Figure 3-22C)** shows the PCR genotyping result of a WT animal and a mouse, which is heterozygous for the L3F2 allele.

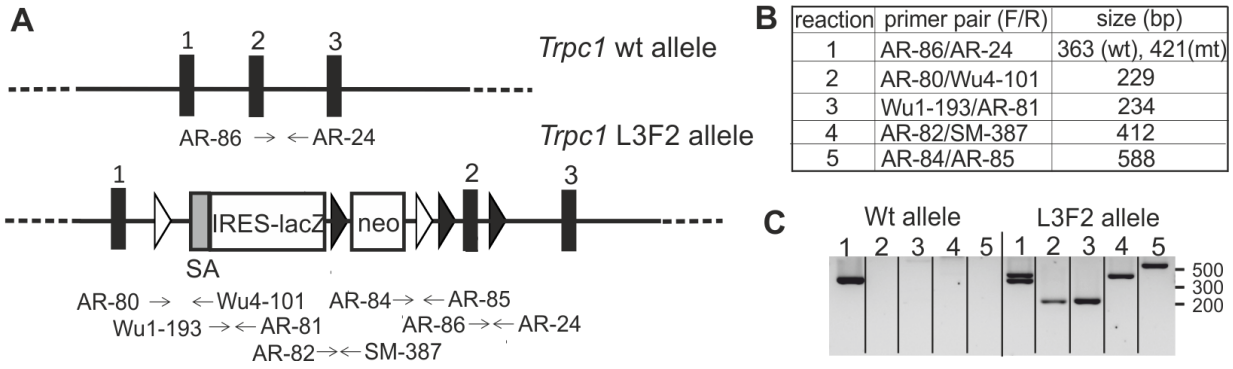

Figure 3-22 Genotyping strategy to identify the *Trpc1*-L3F2 allele and to genotype mice. (A) Genotyping strategy: *Trpc1* wt allele shows three coding exons (1-3, black boxes, not in scale) approximate location of primer combinations is shown spanning over the exon two to identify the wt allele by PCR. *Trpc1* L3F2 allele contains consensus *FRT* sites (unfilled triangles), in between the *FRT* sites, SA-IRES-*lacZ*-*loxP* site-neo cassette is shown. Exon two is flanked by *loxP* sites (filled triangles), arrows indicate position of forward and reverse primers used for PCR. **(B)** Table (top) shows the forward (F) and reverse (R) primer combinations used the PCR reactions along with the expected sizes. **(C)** Representative agarose gel image shows the PCR results for the identification of mice carrying wt and L3F2 alleles. Numbers indicate PCR reactions from the table.

By using PCR genotyping, we identified heterozygous pups in the F1 generation bearing L3F2 allele, indicative of successful germline transmission **(Figure 3-23)**.

Figure 3-23 Conditional *Trpc1* heterozygous mice in F1 generation. Representative images of heterozygous mice identified by genotyping. Mice shown on left and right side resulted from the injection of ES cell clones 3.2D2 and 3.1D4, respectively.

3.5.4 Generation of *Trpc1* flox mice

The heterozygous L3F2 mice serve as a basis for the generation of *Trpc1*-flox mice. Currently heterozygous L3F2 mice are being crossed with Flp deleter mice to remove the *FRT* flanked SA-IRES-*lacZ*-*loxP*-neo cassette resulting in a floxed L2F1 allele **(Figure 3-24B)**. First pups were born and PCR based genotyping revealed the generation of mice bearing L2F1 allele. Figure shows a representative PCR genotyping result of a *Trpc1*$^{+/flox}$ animal, which is also positive for Flp recombinase **(Figure 3-24C)**. Next step will be backcrossing with C57BL6/N wild-type mice to get rid of the Flp gene. The resulting *Trpc1*$^{+/flox}$ Flp^{-} mice can be used for crossing with a osteoclasts specific Cre mouse lines *e.g*. a TRAP- or Cat K- Cre mouse lines (Chiu *et al.*, 2004) to generate an osteoclast specific *Trpc1* KO mouse strain.

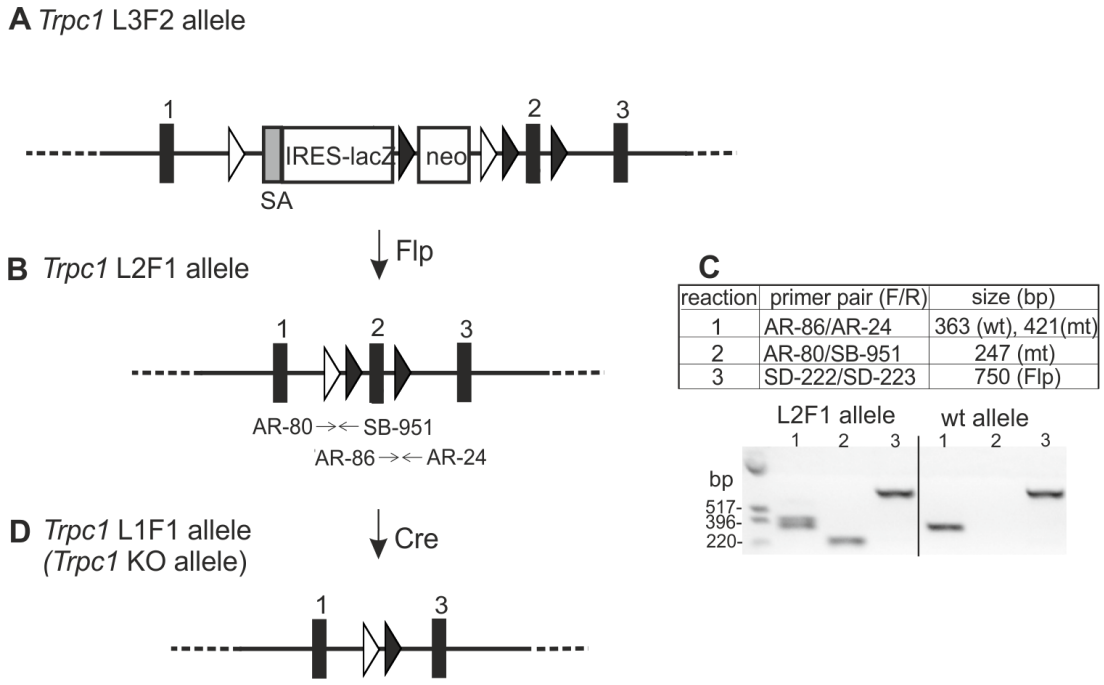

Figure 3-24 Generation of *Trpc1* flox mice. Breeding strategy to generate *Trpc1* flox mice: **(A)** *Trpc1* L3F2 allele contains three exons (1-3), black boxes (not in scale). The targeting construct consists of consensus *FRT* sites (unfilled triangles), in between these sites, SA-IRES-*lacZ*-*loxP* site-neo cassette is located, exon two flanked by *loxP* sites (filled triangles) is shown. Flp-mediated excision will lead to **(B)** *Trpc1* L2F1 allele consisting of a *FRT* site downstream of the exon one and a floxed exon two. **(C)** Table (top) shows the forward (F) and reverse (R) primer combinations used for the PCR reactions along with the expected sizes; a representative agarose gel image (bottom) depicts the PCR results for the identification of mice carrying L2F1 and wt alleles. Both animals are positive for the Flp recombinase as shown in reaction three. Numbers indicate PCR reactions from the table. **(D)** Cre-mediated excision of *Trpc1* L2F1 allele will lead to *Trpc1* L1F1, which is a *Trpc1* KO allele, containing singular *FRT* and *loxP* sites present in between exon one and three as indicated.

4 Discussion

In my thesis, I have generated two mouse strains, TRPC1-IRES-Cre mice and mice carrying a conditional *Trpc1* allele. Both mouse strains will allow dissecting the physiological and pathophysiological roles of *Trpc1* in the living organism. In order to characterize the physiological function of *Trpc1* in bone, I established µCT analysis of long bones, a femur fracture model and the methods to differentiate osteoclasts and to characterize their function. In the following, I will first discuss the contribution of *Trpc1* to bone function, followed by a discussion of the two mouse strains, which I have generated.

4.1 Contribution of TRPC1 to bone function

Although the TRPC1 cDNA was the first mammalian cDNA which has been cloned (Wes *et al.,* 1995), (Zhu *et al.*, 1995), it is still an open question whether TRPC1 itself forms a functional channel or whether it is a part of a heteromeric TRP channel complex. In brain and in hippocampal neurons TRPC1 is a part of heteromeric TRPC4/TRPC1, TRPC5/TRPC1 or TRPC5/TRPC4/TRPC1 channels (Broker-Lai *et al*., 2017). In heterologous expression systems, including cell culture cells such as HEK293 cells or oocytes TRPC1 also forms heterotetrameric channels with TRPC4, TRPC5 but also with TRPV4 or TRPV6. Especially TRPV6 has been shown to negatively interfere with functional TRPC1 or *vice versa* (Courjaret *et al*., 2013), (Schindl *et al*., 2012) . Compared to the broad *Trpc1* gene expression the *Trpv6* gene expression is quite restricted, especially to epididymis, placenta, pancreatic acinar cells and bone.

Both *Trpv6* and *Trpc1* transcripts have been identified in various immortalized bone cells. For instance, we could identify *Trpc1* transcripts in a number of human osteoblast-like cells such as SAOS-2, U-2 OS, SK-N-SH and MG-63 **(**Supplementary **Figure 6-7)**, whereas *Trpv6* transcripts have been identified in the murine KS483 and the human SV-HFO osteoblast-like cells (van der Eerden *et al.,* 2012) and in the murine osteoclast-like cell-line RAW264.7 (van der Eerden *et al*., 2012). More important, van der Eerden *et al.* and Ong *et al.* have shown that either transcript is expressed in cells derived from bone in living mice, but whether or whether not they function in concert or independently is not known.

We decided to answer this question by two approaches: First, we wanted to confirm that transcripts of both genes are expressed in bone. In case, the transcripts are present we wanted to study whether deletion of either gene provokes a bone phenotype. If there would be a phenotype, it would be worthy to go back and analyze bone function and bone cell function in detail.

To get an answer to question one, I performed RT-PCR using RNA from crushed bone as a template. By this approach, I amplified the full-length protein coding 2879 bp cDNA of *Trpc1* **(Figure 3-3A)** and a 242 bp fragment of *Trpv6* **(Figure 3-3D).** These results confirmed that TRPC1 and TRPV6 are expressed in bone. TRPC1 gene-deficient (KO) mice are available in the laboratory as a part of collaboration with Alexander Dietrich (München) and Lutz Birnbaumer (Buenos Aires), as well as TRPV6 mutant mice, which have been generated in our group (Weissgerber *et al.,* 2011), (Weissgerber *et al*., 2012). TRPV6 mutant mice carry a point mutation, which renders the TRPV6 channel non-functional; they behave like TRPV6 KO mice also generated in our group (Weissgerber *et al*., 2012). Next, we thought about a bone phenotype. Using a Bruker µCT system (SkyScan 1172) available at the Institut für Klinisch-Experimentelle Chirurgie, Universität des Saarlandes, Homburg, we decided to look for a phenotype in long bones by comparing the femurs from wild-type, *Trpc1*$^{-/-}$, *Trpv6*$^{mt/mt}$ and *Trpc1*$^{-/-}$/*Trpv6*$^{mt/mt}$ mice.

Mice have been extensively studied using µCT to determine the bone structure at the finest resolution. However, there are several considerations, both mouse- and scanning system-related, that must be taken into account before starting the experiment. Mouse related factors include the effect of age, gender, and genetic background (Halloran *et al.,* 2002), (Wergedal *et al.,* 2005). The µCT-related technical aspects include image resolution, X-ray source voltage and current, filter type and thickness, exposure time and application of beam hardening corrections. We aimed to establish a consistent way of determining the cortical and trabecular bone microarchitecture in line with the guidelines published by Bouxsein (Bouxsein *et al.,* 2010).

Genetic heterogeneity has an effect on the bone phenotype and has to be considered when analyzing the bone parameters (Jilka, 2013). In our animal facility, mice are available on two genetic backgrounds, either as C57BL/6 strain or as mixed 129SvJ/C57BL/6 strain. Like human bones, bones in mice undergo age-dependent changes (Jilka, 2013) and firstly we have

analyzed femurs of wild-type mice of the two genetic strains at two ages, at 12 and at 24 weeks of age. For this basic experiment, we have restricted our studies only to male mice to avoid any influence of recurring physiological changes induced by reproductive hormones in females (Halloran *et al.,* 2002). The settings for µCT scanning were kept constant throughout the study. For the cortical bone analyses, the region of interest covered fifty 6.5 µm cross-sections exactly in the middle of the femur shaft irrespective of age **(Figure 2-5Aa, Ba)**. For the trabecular bone analyses, cross-sections in the region of secondary or mature spongiosa have been used where trabeculae are stable, avoiding the contamination of primary spongiosa as much as possible **(Figure 2-5Ab, Bb)**. Accordingly, I reduced the "offset" for analyzing trabecular bone from 24-week-old mice compared to the measurements of bones from 12-week-old mice **(Figure 2-5Bb)**, although at these two ages, 12- and 24-week, this adjustment yielded identical values of trabecular bone parameters as if taken the 12-week or 24-week offset for both ages (data not shown).

As expected femur length increased with age up to the 12th week in B6, but not in mixed **(Figure 3-1D, E)** and there was an additional increase from the 12th to the 24th week. The cortical bone parameters such as endocortical volume and perimeter increased with age in bones of mice on B6 background **(Figure 3-2A)** but not in bones of mice of mixed genetic background. In comparison to the cortical bone parameters, we have found more prominent differences in trabecular bone parameter with an advancing age in wild-type mice on mixed genetic background with considerable loss of bone volume and trabecular number **(Figure 3-2B)**. Considering these parameters, B6 femurs were not as much affected. Thus, initial investigation emphasizes the need, only to compare mice on an identical genetic background.

For comparing the bone phenotype of *Trpc1*$^{-/-}$, *Trpv6*$^{mt/mt}$, *Trpc1*$^{-/-}$/*Trpv6*$^{mt/mt}$ and wild-type mice, we therefore bred the respective genotypes on the uniform mixed background and consecutively analyzed femurs of 24-week-old male mice. Femur length was shorter in *Trpv6*$^{mt/mt}$ and *Trpc1*$^{-/-}$/*Trpv6*$^{mt/mt}$ mice but not in *Trpc1*$^{-/-}$ mice when compared to femur length of wild-type mice. The cortical bone phenotype in *Trpv6*$^{mt/mt}$ and *Trpc1*$^{-/-}$/*Trpv6*$^{mt/mt}$ mice compared to wild-type and *Trpc1*$^{-/-}$ mice is more prominent as indicated by reduction in endocortical volume and significant increase in cross-sectional thickness **(Figure 3-4B)** of femurs. In the double mutant *Trpc1*$^{-/-}$/*Trpv6*$^{mt/mt}$ mice, we have observed cortical bone differences similar to the *Trpv6*$^{mt/mt}$ suggesting the dominant effect of the *Trpv6* mutant. Our

results do not fully agree with the findings that cortical and trabecular parameters remained unchanged in *Trpv6* mutant femurs as compared to WT mice (van der Eerden *et al.,* 2012). However, the study by van der Eerden *et al.* have also reported reduced femur length and reduced endocortical volume (van der Eerden *et al.,* 2012). Our results suggest a thicker cortical bone in *Trpv6*$^{mt/mt}$ and *Trpc1*$^{-/-}$/*Trpv6*$^{mt/mt}$ mice, indicative of increased mechanical strength. Although µCT parameters such as polar moment of inertia enables us to predict mechanical properties of the bone (Shefelbine *et al.,* 2005), we performed three-point bending stiffness test to directly monitor the mechanical properties of the femurs (Allen and Burr, 2014). Our results show that a significantly elevated force (N) is required for bending bones from *Trpv6*$^{mt/mt}$ and *Trpc1*$^{-/-}$*/Trpv6*$^{mt/mt}$ mice **(Figure 3-6)** which is in agreement with the expectations of the µCT data.

Different to the cortical bone, the trabecular bone parameters are more affected in femurs from *Trpc1*$^{-/-}$ mice: The bone volume fraction, the mineral density and the trabecular thickness is reduced as compared to wild-type femurs. The trabecular separation and trabecular pattern factor are increased fitting with the reduced bone volume fraction as expected **(Figure 3-4C)**. Our data from the femur bone analyses from 12-week-old WT and *Trpc1*$^{-/-}$mice on B6 background **(**supplementary **Figure 6-8)** comply with the trabecular phenotype observed in mice on mixed genetic background. In summary, these findings confirmed the effect of TRPC1 on bone microarchitecture independent of the genetic heterogeneity. Our results are in contrast with the findings from the group of Leonidas Tsiokas, which showed significantly increased trabecular bone mass, whereas all other parameters remained unchanged (Ong *et al.,* 2013). At least three reasons might explain these differences: Ong *et al*. showed µCT analysis performed on the tibiae from 12-week-old mice, the µCT scanning settings have not been fully described and might have been different, and the genetic background of the mice analyzed is not known.

The trabecular number is increased in *Trpv6*$^{mt/mt}$ femurs and, again, data indicate a dominant effect of the TRPV6 mutation on the *Trpc1* KO, abrogating the TRPC1 phenotype. In summary, these data indicate that deletion/mutation of TRPV6 cannot be compensated by the deletion of TRPC1 whereas the effect of *Trpc1* deletion on trabecular bone was compensated by the *Trpv6* mutation.

Those findings prompted us to investigate the involvement of these channel subunits in a functional assay, in healing of a defined femur fracture (Histing *et al.,* 2011). Fracture healing is a complex phenomenon, which begins with the inflammatory response and involves a variety of cellular components, growth factors and cytokines (Stegen *et al.,* 2015). Osteoclasts perform cartilage resorption and remodeling while osteoblasts form new bone and together these are the two main key players in the healing process of a fractured bone (He *et al.,* 2017). We have used a closed femur fracture model in our studies where the ends of a broken femur are stabilized by a screw **(Figure 2-1)**. Although some cells of the intramedullary cavity could get flush out, and thereupon might interfere with the healing mechanism. During the fracture healing, the periosteal and endosteal callus tissue, surrounding the cortical bone, provides mechanical stability to the fractured bone. Therefore, for the precise determination of callus parameters, it is mandatory to select all callus tissue for analyses. Unfortunately, currently there is no reliable algorithm available for the automatic isolation of the region of the callus, therefore I have selected the callus region of interest manually by drawing the borders of the callus **(**Supplementary **Figure 6-5)**.

The µCT data obtained show a significantly reduced amount of callus volume in fractured femurs of *Trpv6*$^{mt/mt}$ and *Trpc1*$^{-/-}$*/Trpv6*$^{mt/mt}$ mice. The percentage of highly mineralized bony callus is also increased in these mice, an indicative for the rapid healing process. The trabecular parameters such as trabecular number and the estimate of mineral density is also increased in femurs from *Trpv6*$^{mt/mt}$ - and *Trpc1*$^{-/-}$*/Trpv6*$^{mt/mt}$ mice, indicative of more bony callus **(Figure 3-5)**. However, this "bony callus" does not translate into increased mechanical strength because we observed no difference in the bending stiffness of the fractured bones from all four groups using three-point bending test **(**Supplementary **Figure 6-3)**. It must be noted that a four-point bending test might be preferable for estimation of the bending stiffness in fractured bones because of a more adequate application of the bending forces to the femur (Allen and Burr, 2014): The surface of the bony callus is not smooth and the force transducer hits exactly the fractured region of the femur using the three-point bending apparatus.

The µCT findings point to a remarkable trabecular phenotype in *Trpc1*$^{-/-}$ mice and as osteoclasts and osteoblast are major players in bone modelling and remodeling to construct the overall bone structure, we decided to elucidate the role of *Trpc1* in osteoclast formation and functionality. During differentiation of bone marrow derived cells to osteoclasts, we

observed a significant reduction in osteoclast number. This reduction was mirrored by less bone resorption monitored by von Kossa stained pits and trails **(Figure 3-8)**. Our observations from the osteoclast culture experiments contrast with the µCT results where we have observed reduced trabecular numbers. Our culture experiments also contrast with the published results from the group of L. Tsiokas: Ong *et al.* have shown no difference in osteoclast differentiation and resorption in the cultured cells from wild-type and *Trpc1*$^{-/-}$ mice (Ong *et al.,* 2013). As osteoclasts and osteoblasts both play a vital role in the fracture healing, compromised osteoclastogenesis would slow down the cartilage resorption ultimately resulting in delayed fracture healing. On the other hand, the fractured bone data has shown no significant differences in callus tissue parameters from *Trpc1*$^{-/-}$ mice compared to wild-type mice. Therefore, further attention must be paid towards primary osteoblasts, which do express *Trpc1* **(**supplementary **Figure 6-7B)**, and might essentially contribute to the observed trabecular bone phenotype.

4.2 Generation of a *Trpc1*-IC KI mouse strain

Gathering conclusive data on the presence of TRPC1 protein in a given cell is challenging because of the lack of reliable TRPC1-antibodies for immunohistochemistry as well as the absence of authentic TRPC1-mediated currents in patch-clamp experiments. In order to overcome these limitations, there was a critical need of visualizing *Trpc1*-expressing cells in mice including TRPC1-expressing bone cells.

I generated a novel TRPC1-IRES-Cre knock-in mouse strain by inserting an IRES-Cre cassette 26 nucleotides downstream of the stop codon present within coding exon 13 of the *Trpc1* gene. The presence of an IRES element causes transcription of a bicistronic mRNA under control of the endogenous TRPC1 promoter, which is translated into two independent proteins, TRPC1 and Cre recombinase within the same cell. For the characterization of *Trpc1*-expressing cells, homozygous *Trpc1*-IC mice have been bred with the reporter mouse strain eROSA26-τGFP (Wen *et al.,* 2011) to obtain double knock-in *Trpc1*-IC/eR26-τGFP mice. The Cre recombinase present in *Trpc1*-expressing cells, deletes the transcriptional termination signal dubbed "STOP" in **Figure 3-10**. As a consequence, the DNA of the green fluorescent protein will be expressed under control of the ROSA26 promoter. The ROSA26 (R26) locus is ubiquitously expressed. The efficiency of the R26 promoter has been enhanced by introducing a so called CAGS fragment based the on chicken-β-actin promoter and cytomegalovirus (CMV) enhancer (Wen *et al.,* 2011). Once switched on by Cre-dependent recombination, the green fluorescence exclusively depends on the eR26 locus. In the absence of Cre-mediated recombination, the transcriptional termination signal "STOP" flanked by two *loxP* sites, prevents transcription of the GFP DNA. Other reporter mouse strains (Wyatt *et al.,* 2017) carrying yellow or red fluorescent protein, can be bred with the TRPC1-IC mouse.

This binary genetic approach leads to the amplification of the fluorescent signal and thereby visualizes*Trpc1*-expressing cells. Other strategies involve the fusion of the fluorescent protein DNA as an IRES cassette: Like expression of the IRES-Cre cassette in the TRPC1-IC mouse, the expression of the IRES GFP cassette would be under the control of the TRPC1 promoter. Considering a very low expression level of TRPC1, the GFP expression would also very low and the fluorescent signal would be difficult to be detected using the later approach. In the current approach, fluorophore and Cre recombinase are expressed from two independent promotors: Even a single Cre molecule is sufficient to "switch on" the transcription of the GFP DNA. In

summary, *Trpc1*-IC KI mouse strain is a step towards solving the expression profile of the *Trpc1* gene.

In ongoing experiments, we, my colleague Dr. Hongmei Wang and myself, have visualized TRPC1 expressing cells in the pituitary after breeding the *Trpc1*-IC and the eROSA26-τGFP mouse lines. Single green cells and non-green cells were isolated and checked for the expression of *Trpc1*. All green cells and very low non-green cells do express *Trpc1* transcripts (manuscript submitted). Apparently, the green fluorescence of the "non-green" cells expressing *Trpc1* might escape our detection. Overall, these experiments demonstrate the versatility of this approach.

4.3 Generation of a conditional *Trpc1* mouse strain

In addition to the *Trpc1*-IC strain, I generated a mouse line carrying a conditional *Trpc1* allele that functions as a wild-type allele in an undeleted state or as a null allele upon Cre-mediated excision. In 2007, Dietrich *et al.* described the generation of a global *Trpc1* knockout by deleting the coding exon 8, supposedly involved in the formation of a pore region (Dietrich *et al.,* 2007). This global *Trpc1* gene-deficient model has been studied to characterize the role of TRPC1 in working memory formation (Broker-Lai *et al.,* 2017), salivary fluid secretions (Ambudkar, 2014), in hemodynamic stress and cardiac hypertrophy (Seth *et al.,* 2009), osteoclastogenesis and bone architecture (Ong *et al.,* 2013). However, by the global TRPC1 knockout, it is difficult to determine the role of TRPC1 in specific cells or organs. Therefore, it was in high demand to generate a conditional *Trpc1* mouse model enabling to study the cell-specific role of *Trpc1* without interfering with the expression of *Trpc1* in other cells.

For the generation of a conditional *Trpc1* mouse strain, we first wanted to insert *loxP* sites up-stream of exon seven and downstream of exon eight. However, because of presence of repetitive nucleic acid sequences we abandoned that targeting strategy. As an alternative strategy, exon two was flanked by *loxP* sites. The resulting targeting vector was electroporated into ES cells. The ES cells were selected and the homologous recombination in ES cells heterozygous for the mutation was proven by PCR and Southern blotting. We performed three independent set of trials by injecting six different ES cell clones at IBF, Heidelberg in cooperation with Prof. Dr. Marc Freichel and at *iTL* (New York, USA). From three independent clones we received 14 chimeras at IBF, with the chimerism percentage based on coat color distribution varies between 10-90%. We set different breedings in order to get F1 mice *i.e.* germline transmission but remained unsuccessful. The reason for this ordeal remained unknown. However, we remained successful in obtaining chimeras and subsequently F1 mice at *iTL* from three independent ES cell clones **(**supplementary **Table 6-7)**. With these F1 mice carrying the conditional allele, it is possible to obtain mice carrying a *Trpc1* floxed allele by Flp recombinase activity and/or a *Trpc1* L1F1 allele upon Cre-recombinase activity **(Figure 3-17)**.

Conditional gene targeting using a site-specific recombinase system *i.e.* Cre/*loxP* allows to delete the *Trpc1* gene from any desired organ or a cell type at any time using a specific Cre-recombinase expressing deleter mouse strains. It is based on the principle of breeding two independent mouse strains; one carrying a floxed *Trpc1* allele and the other strain expresses

Cre-recombinase in selected cell types or tissues. For instance, we have observed a trabecular bone phenotype and compromised osteoclastogenesis in our experiments performed on *Trpc1*-global knockout mice. For precisely defining the role of *Trpc1* in osteoclast, deletion of *Trpc1* specifically in osteoclasts is required using Cre-deleter strains which express the Cre-recombinase gene under control of either TRAP or Cat K promoters (Chiu *et al.,* 2004). The *Osx (Osxterix*)-*Cre* mouse strain can be used to delete *Trpc1* specifically from the osteoblasts (Rodda and McMahon, 2006). However, endogenous skeletal defects such as delayed calvarial ossification have been identified in *Osx-Cre* deleter mice; making these mice not a good choice (Huang and Olsen, 2015).

In summary, the conditional *Trpc1* mouse strain will be useful for the deletion of the *Trpc1* gene in a spatially restricted or/and temporally restricted way. Our knowledge from studies with *Trpc1* global knockout mice and our new studies with the *Trpc1*-IRES-Cre mouse have been shown the involvement of TRPC1 in different cells serving different functions. Studies with the conditional *Trpc1* strain will complement this work and allow to dissect *Trpc1* function with higher accuracy.

5 References

5.1 Reference list

Aaron, R.K., Ciombor, D.M., Wang, S., and Simon, B. (2006). Clinical biophysics: the promotion of skeletal repair by physical forces. Ann N Y Acad Sci *1068*, 513-531.

Ai-Aql, Z.S., Alagl, A.S., Graves, D.T., Gerstenfeld, L.C., and Einhorn, T.A. (2008). Molecular mechanisms controlling bone formation during fracture healing and distraction osteogenesis. J Dent Res *87*, 107-118.

Albert, H., Dale, E.C., Lee, E., and Ow, D.W. (1995). Site-specific integration of DNA into wild-type and mutant lox sites placed in the plant genome. Plant J *7*, 649-659.

Allen, M.R., and Burr, D.B. (2014). Basic and applied bone biology (London; Waltham, MA: Academic Press).

Ambudkar, I.S. (2014). Ca^{2+} signaling and regulation of fluid secretion in salivary gland acinar cells. Cell Calcium *55*, 297-305.

Andersen, T.L., Abdelgawad, M.E., Kristensen, H.B., Hauge, E.M., Rolighed, L., Bollerslev, J., Kjaersgaard-Andersen, P., and Delaisse, J.M. (2013). Understanding coupling between bone resorption and formation: are reversal cells the missing link? Am J Pathol *183*, 235-246.

Andersen, T.L., Sondergaard, T.E., Skorzynska, K.E., Dagnaes-Hansen, F., Plesner, T.L., Hauge, E.M., Plesner, T., and Delaisse, J.M. (2009). A physical mechanism for coupling bone resorption and formation in adult human bone. Am J Pathol *174*, 239-247.

Barnes, G.L., Kostenuik, P.J., Gerstenfeld, L.C., and Einhorn, T.A. (1999). Growth factor regulation of fracture repair. J Bone Miner Res *14*, 1805-1815.

Beck, A., Gotz, V., Qiao, S., Weissgerber, P., Flockerzi, V., Freichel, M., and Boehm, U. (2017). Functional Characterization of Transient Receptor Potential (TRP) Channel C5 in Female Murine Gonadotropes. Endocrinology *158*, 887-902.

Bianco, S.D., Peng, J.B., Takanaga, H., Suzuki, Y., Crescenzi, A., Kos, C.H., Zhuang, L., Freeman, M.R., Gouveia, C.H., Wu, J.*, et al.* (2007). Marked disturbance of calcium homeostasis in mice with targeted disruption of the Trpv6 calcium channel gene. J Bone Miner Res *22*, 274-285.

Bolander, M.E. (1992). Regulation of fracture repair by growth factors. Proc Soc Exp Biol Med *200*, 165-170.

Bonewald, L.F. (2007). Osteocytes as dynamic multifunctional cells. Ann N Y Acad Sci *1116*, 281-290.

Bosemark, P., Isaksson, H., McDonald, M.M., Little, D.G., and Tagil, M. (2013). Augmentation of autologous bone graft by a combination of bone morphogenic protein and bisphosphonate increased both callus volume and strength. Acta Orthop *84*, 106-111.

Bouillon, R., and Prodonova, A. (2000). Growth and hormone deficiency and peak bone mass. J Pediatr Endocrinol Metab *13 Suppl 6*, 1327-1336.

Bouxsein, M.L., Boyd, S.K., Christiansen, B.A., Guldberg, R.E., Jepsen, K.J., and Muller, R. (2010). Guidelines for assessment of bone microstructure in rodents using micro-computed tomography. J Bone Miner Res *25*, 1468-1486.

Brixel, L.R., Monteilh-Zoller, M.K., Ingenbrandt, C.S., Fleig, A., Penner, R., Enklaar, T., Zabel, B.U., and Prawitt, D. (2010). TRPM5 regulates glucose-stimulated insulin secretion. Pflugers Arch *460*, 69-76.

Broker-Lai, J., Kollewe, A., Schindeldecker, B., Pohle, J., Nguyen Chi, V., Mathar, I., Guzman, R., Schwarz, Y., Lai, A., Weissgerber, P.*, et al.* (2017). Heteromeric channels formed by TRPC1, TRPC4 and TRPC5 define hippocampal synaptic transmission and working memory. EMBO J *36*, 2770-2789.

Buchholz, F., Angrand, P.O., and Stewart, A.F. (1998). Improved properties of FLP recombinase evolved by cycling mutagenesis. Nat Biotechnol *16*, 657-662.
Cao, E., Liao, M., Cheng, Y., and Julius, D. (2013). TRPV1 structures in distinct conformations reveal activation mechanisms. Nature *504*, 113-118.

Cao, X., and Chen, D. (2005). The BMP signaling and in vivo bone formation. Gene *357*, 1-8.

Capecchi, M.R. (1989). Altering the genome by homologous recombination. Science *244*, 1288-1292.

Casanova, M., Herelle, J., Thomas, M., Softley, R., Schindeler, A., Little, D., Schneider, P., and Muller, R. (2016). Effect of combined treatment with zoledronic acid and parathyroid hormone on mouse bone callus structure and composition. Bone *92*, 70-78.

Casanova, M., Schindeler, A., Little, D., Muller, R., and Schneider, P. (2014). Quantitative phenotyping of bone fracture repair: a review. Bonekey Rep *3*, 550.

Chen, D., Zhao, M., and Mundy, G.R. (2004). Bone morphogenetic proteins. Growth Factors *22*, 233-241.

Chiu, W.S., McManus, J.F., Notini, A.J., Cassady, A.I., Zajac, J.D., and Davey, R.A. (2004). Transgenic mice that express Cre recombinase in osteoclasts. Genesis *39*, 178-185.

Chung, C.T., Niemela, S.L., and Miller, R.H. (1989). One-step preparation of competent Escherichia coli: transformation and storage of bacterial cells in the same solution. Proc Natl Acad Sci U S A *86*, 2172-2175.

Church, G.M., and Gilbert, W. (1984). Genomic sequencing. Proc Natl Acad Sci U S A *81*, 1991-1995.

Colsoul, B., Schraenen, A., Lemaire, K., Quintens, R., Van Lommel, L., Segal, A., Owsianik, G., Talavera, K., Voets, T., Margolskee, R.F.*, et al.* (2010). Loss of high-frequency glucose-induced Ca2+ oscillations in pancreatic islets correlates with impaired glucose tolerance in Trpm5-/- mice. Proc Natl Acad Sci U S A *107*, 5208-5213.

Cosens, D.J., and Manning, A. (1969). Abnormal Electroretinogram from a Drosophila Mutant. Nature *224*, 285.

Courjaret, R., Hubrack, S., Daalis, A., Dib, M., and Machaca, K. (2013). The Xenopus TRPV6 homolog encodes a Mg(2+) -permeant channel that is inhibited by interaction with TRPC1. J Cell Physiol *228*, 2386-2398.

Day, T.F., Guo, X., Garrett-Beal, L., and Yang, Y. (2005). Wnt/beta-catenin signaling in mesenchymal progenitors controls osteoblast and chondrocyte differentiation during vertebrate skeletogenesis. Dev Cell *8*, 739-750.

Dietrich, A., Fahlbusch, M., and Gudermann, T. (2014). Classical Transient Receptor Potential 1 (TRPC1): Channel or Channel Regulator? Cells *3*, 939-962.

Dietrich, A., Kalwa, H., Storch, U., Mederos y Schnitzler, M., Salanova, B., Pinkenburg, O., Dubrovska, G., Essin, K., Gollasch, M., Birnbaumer, L.*, et al.* (2007). Pressure-induced and store-operated cation influx in vascular smooth muscle cells is independent of TRPC1. Pflugers Arch *455*, 465-477.

Dietrich, A., Mederos, Y.S.M., Gollasch, M., Gross, V., Storch, U., Dubrovska, G., Obst, M., Yildirim, E., Salanova, B., Kalwa, H.*, et al.* (2005). Increased vascular smooth muscle contractility in TRPC6-/- mice. Mol Cell Biol *25*, 6980-6989.

Dohke, Y., Oh, Y.S., Ambudkar, I.S., and Turner, R.J. (2004). Biogenesis and topology of the transient receptor potential Ca2+ channel TRPC1. J Biol Chem *279*, 12242-12248.

Dymecki, S.M. (1996). Flp recombinase promotes site-specific DNA recombination in embryonic stem cells and transgenic mice. Proc Natl Acad Sci U S A *93*, 6191-6196.

Eckardt, I., and Hein, H.J. (2001). Quantitative measurements of the mechanical properties of human bone tissues by scanning acoustic microscopy. Ann Biomed Eng *29*, 1043-1047.

Eghbali-Fatourechi, G.Z., Lamsam, J., Fraser, D., Nagel, D., Riggs, B.L., and Khosla, S. (2005). Circulating osteoblast-lineage cells in humans. N Engl J Med *352*, 1959-1966.

Einhorn, T.A. (1998). The cell and molecular biology of fracture healing. Clin Orthop Relat Res, S7-21.

Epari, D.R., Duda, G.N., and Thompson, M.S. (2010). Mechanobiology of bone healing and regeneration: in vivo models. Proc Inst Mech Eng H *224*, 1543-1553.

Everts, V., Delaisse, J.M., Korper, W., Jansen, D.C., Tigchelaar-Gutter, W., Saftig, P., and Beertsen, W. (2002). The bone lining cell: its role in cleaning Howship's lacunae and initiating bone formation. J Bone Miner Res *17*, 77-90.

Feinberg, A.P., and Vogelstein, B. (1984). "A technique for radiolabeling DNA restriction endonuclease fragments to high specific activity". Addendum. Anal Biochem *137*, 266-267.

Flockerzi, V., and Nilius, B. (2007). Transient receptor potential (TRP) channels (Berlin: Springer).

Freichel, M., Almering, J., and Tsvilovskyy, V. (2012). The Role of TRP Proteins in Mast Cells. Front Immunol *3*, 150.

Garcia-Otin, A.L., and Guillou, F. (2006). Mammalian genome targeting using site-specific recombinases. Front Biosci *11*, 1108-1136.

Gerstenfeld, L.C., Cullinane, D.M., Barnes, G.L., Graves, D.T., and Einhorn, T.A. (2003). Fracture healing as a post-natal developmental process: molecular, spatial, and temporal aspects of its regulation. J Cell Biochem *88*, 873-884.

Green, M.R., and Sambrook, J. (2012). Molecular cloning a laboratory manual (Cold Spring Harbor, N.Y.: Cold Spring Harbor Laboratory Press).

Halloran, B.P., Ferguson, V.L., Simske, S.J., Burghardt, A., Venton, L.L., and Majumdar, S. (2002). Changes in bone structure and mass with advancing age in the male C57BL/6J mouse. J Bone Miner Res *17*, 1044-1050.

He, L.H., Liu, M., He, Y., Xiao, E., Zhao, L., Zhang, T., Yang, H.Q., and Zhang, Y. (2017). TRPV1 deletion impaired fracture healing and inhibited osteoclast and osteoblast differentiation. Sci Rep *7*, 42385.

Helfrich, M.H. (2012). Bone Research Protocols (New York: Humana Press).

Herath, S.C., Lion, T., Klein, M., Stenger, D., Scheuer, C., Holstein, J.H., Morsdorf, P., Rollmann, M.F., Pohlemann, T., Menger, M.D*., et al.* (2015). Stimulation of angiogenesis by cilostazol accelerates fracture healing in mice. J Orthop Res *33*, 1880-1887.

Hernlund, E., Svedbom, A., Ivergard, M., Compston, J., Cooper, C., Stenmark, J., McCloskey, E.V., Jonsson, B., and Kanis, J.A. (2013). Osteoporosis in the European Union: medical management, epidemiology and economic burden. A report prepared in collaboration with the International Osteoporosis Foundation (IOF) and the European Federation of Pharmaceutical Industry Associations (EFPIA). Arch Osteoporos *8*, 136.

Hirnet, D., Olausson, J., Fecher-Trost, C., Bodding, M., Nastainczyk, W., Wissenbach, U., Flockerzi, V., and Freichel, M. (2003). The TRPV6 gene, cDNA and protein. Cell Calcium *33*, 509-518.

Histing, T., Garcia, P., Holstein, J.H., Klein, M., Matthys, R., Nuetzi, R., Steck, R., Laschke, M.W., Wehner, T., Bindl, R.*, et al.* (2011). Small animal bone healing models: standards, tips, and pitfalls results of a consensus meeting. Bone *49*, 591-599.

Hoenderop, J.G., Vennekens, R., Muller, D., Prenen, J., Droogmans, G., Bindels, R.J., and Nilius, B. (2001). Function and expression of the epithelial Ca^{2+} channel family: comparison of mammalian ECaC1 and 2. J Physiol *537*, 747-761.

Hoenderop, J.G., Voets, T., Hoefs, S., Weidema, F., Prenen, J., Nilius, B., and Bindels, R.J. (2003). Homo- and heterotetrameric architecture of the epithelial Ca2+ channels TRPV5 and TRPV6. EMBO J *22*, 776-785.

Hoess, R.H., Ziese, M., and Sternberg, N. (1982). P1 site-specific recombination: nucleotide sequence of the recombining sites. Proc Natl Acad Sci U S A *79*, 3398-3402.

Holmes, D.S., and Quigley, M. (1981). A rapid boiling method for the preparation of bacterial plasmids. Anal Biochem *114*, 193-197.

Huang, W., and Olsen, B.R. (2015). Skeletal defects in Osterix-Cre transgenic mice. Transgenic Res *24*, 167-172.

Jacks, T., Shih, T.S., Schmitt, E.M., Bronson, R.T., Bernards, A., and Weinberg, R.A. (1994). Tumour predisposition in mice heterozygous for a targeted mutation in Nf1. Nature Genetics *7*, 353.

Jilka, R.L. (2013). The relevance of mouse models for investigating age-related bone loss in humans. J Gerontol A Biol Sci Med Sci *68*, 1209-1217.

Jin, J., Desai, B.N., Navarro, B., Donovan, A., Andrews, N.C., and Clapham, D.E. (2008). Deletion of Trpm7 disrupts embryonic development and thymopoiesis without altering Mg2+ homeostasis. Science *322*, 756-760.

Jin, J., Wu, L.J., Jun, J., Cheng, X., Xu, H., Andrews, N.C., and Clapham, D.E. (2012). The channel kinase, TRPM7, is required for early embryonic development. Proc Natl Acad Sci U S A *109*, E225-233.

Joyner, A.L. (2005). Gene targeting: a practical approach (Oxford: Oxford Univ. Press).

Juppner, H., Abou-Samra, A.B., Freeman, M., Kong, X.F., Schipani, E., Richards, J., Kolakowski, L.F., Jr., Hock, J., Potts, J.T., Jr., Kronenberg, H.M.*, et al.* (1991). A G protein-linked receptor for parathyroid hormone and parathyroid hormone-related peptide. Science *254*, 1024-1026.

Karsenty, G., Kronenberg, H.M., and Settembre, C. (2009). Genetic control of bone formation. Annu Rev Cell Dev Biol *25*, 629-648.

Katsimbri, P. (2017). The biology of normal bone remodelling. Eur J Cancer Care (Engl) *26*.

Kobayashi, S., Takahashi, H.E., Ito, A., Saito, N., Nawata, M., Horiuchi, H., Ohta, H., Ito, A., Iorio, R., Yamamoto, N.*, et al.* (2003). Trabecular minimodeling in human iliac bone. Bone *32*, 163-169.

Kondo, E., Yasoda, A., Fujii, T., Nakao, K., Yamashita, Y., Ueda-Sakane, Y., Kanamoto, N., Miura, M., Arai, H., Mukoyama, M.*, et al.* (2015). Increased Bone Turnover and Possible Accelerated Fracture Healing in a Murine Model With an Increased Circulating C-Type Natriuretic Peptide. Endocrinology *156*, 2518-2529.

Kornak, U., Kasper, D., Bosl, M.R., Kaiser, E., Schweizer, M., Schulz, A., Friedrich, W., Delling, G., and Jentsch, T.J. (2001). Loss of the ClC-7 chloride channel leads to osteopetrosis in mice and man. Cell *104*, 205-215.

Le Pecq, J.B., and Paoletti, C. (1966). A new fluorometric method for RNA and DNA determination. Anal Biochem *17*, 100-107.

Lehen'kyi, V., Raphael, M., and Prevarskaya, N. (2012). The role of the TRPV6 channel in cancer. J Physiol *590*, 1369-1376.

Leong, P.L., and Morgan, E.F. (2008). Measurement of fracture callus material properties via nanoindentation. Acta Biomater *4*, 1569-1575.

Lieben, L., and Carmeliet, G. (2012). The Involvement of TRP Channels in Bone Homeostasis. Front Endocrinol (Lausanne) *3*, 99.

Lind, M., Deleuran, B., Thestrup-Pedersen, K., Soballe, K., Eriksen, E.F., and Bunger, C. (1995). Chemotaxis of human osteoblasts. Effects of osteotropic growth factors. APMIS *103*, 140-146.

Liu, X., Cheng, K.T., Bandyopadhyay, B.C., Pani, B., Dietrich, A., Paria, B.C., Swaim, W.D., Beech, D., Yildrim, E., Singh, B.B*., et al.* (2007). Attenuation of store-operated Ca2+ current impairs salivary gland fluid secretion in TRPC1$^{-/-}$ mice. Proc Natl Acad Sci U S A *104*, 17542-17547.

Lobe, C.G., Koop, K.E., Kreppner, W., Lomeli, H., Gertsenstein, M., and Nagy, A. (1999). Z/AP, a double reporter for cre-mediated recombination. Dev Biol *208*, 281-292.

Luxenburg, C., Geblinger, D., Klein, E., Anderson, K., Hanein, D., Geiger, B., and Addadi, L. (2007). The architecture of the adhesive apparatus of cultured osteoclasts: from podosome formation to sealing zone assembly. PLoS One *2*, e179.

Lüllmann-Rauch, R. (2012). Taschenlehrbuch Histologie (Stuttgart: Georg Thieme Verlag ;).

Madej, M.G., and Ziegler, C.M. (2018). Dawning of a new era in TRP channel structural biology by cryo-electron microscopy. Pflugers Arch *470*, 213-225.

Martin, T.J., and Sims, N.A. (2005). Osteoclast-derived activity in the coupling of bone formation to resorption. Trends Mol Med *11*, 76-81.

Mattson, M.P. (2012). Parkinson's disease: don't mess with calcium. J Clin Invest *122*, 1195-1198.

Merkwitz, C., Blaschuk, O., Schulz, A., and Ricken, A.M. (2016). Comments on Methods to Suppress Endogenous β-Galactosidase Activity in Mouse Tissues Expressing the LacZ Reporter Gene. Journal of Histochemistry & Cytochemistry *64*, 579-586.

Meyers, E.N., Lewandoski, M., and Martin, G.R. (1998). An Fgf8 mutant allelic series generated by Cre- and Flp-mediated recombination. Nat Genet *18*, 136-141.

Mizuguchi, H., Xu, Z., Ishii-Watabe, A., Uchida, E., and Hayakawa, T. (2000). IRES-dependent second gene expression is significantly lower than cap-dependent first gene expression in a bicistronic vector. Mol Ther *1*, 376-382.

Monroe, D.G., McGee-Lawrence, M.E., Oursler, M.J., and Westendorf, J.J. (2012). Update on Wnt signaling in bone cell biology and bone disease. Gene *492*, 1-18.

Montell, C., and Rubin, G.M. (1989). Molecular characterization of the Drosophila trp locus: a putative integral membrane protein required for phototransduction. Neuron *2*, 1313-1323.

Moreau, R., Daoud, G., Bernatchez, R., Simoneau, L., Masse, A., and Lafond, J. (2002). Calcium uptake and calcium transporter expression by trophoblast cells from human term placenta. Biochimica et Biophysica Acta (BBA) - Biomembranes *1564*, 325-332.

Morgan, E.F., Mason, Z.D., Chien, K.B., Pfeiffer, A.J., Barnes, G.L., Einhorn, T.A., and Gerstenfeld, L.C. (2009). Micro-computed tomography assessment of fracture healing: relationships among callus structure, composition, and mechanical function. Bone *44*, 335-344.

Nagy, A. (2000). Cre recombinase: the universal reagent for genome tailoring. Genesis *26*, 99-109.

Nakase, T., and Yoshikawa, H. (2006). Potential roles of bone morphogenetic proteins (BMPs) in skeletal repair and regeneration. J Bone Miner Metab *24*, 425-433.

Nakashima, K., Zhou, X., Kunkel, G., Zhang, Z., Deng, J.M., Behringer, R.R., and de Crombrugghe, B. (2002). The novel zinc finger-containing transcription factor osterix is required for osteoblast differentiation and bone formation. Cell *108*, 17-29.

Niemeyer, B.A., Bergs, C., Wissenbach, U., Flockerzi, V., and Trost, C. (2001). Competitive regulation of CaT-like-mediated Ca2+ entry by protein kinase C and calmodulin. Proc Natl Acad Sci U S A *98*, 3600-3605.

Nesbitt, S.A., and Horton, M.A. (1997). Trafficking of matrix collagens through bone-resorbing osteoclasts. Science *276*, 266-269.

Nijenhuis, T., Hoenderop, J.G., van der Kemp, A.W., and Bindels, R.J. (2003). Localization and regulation of the epithelial Ca2+ channel TRPV6 in the kidney. J Am Soc Nephrol *14*, 2731-2740.

Nilius, B., and Flockerzi, V. (2014a). Mammalian Transient Receptor Potential (TRP) Cation Channels : Volume II (Cham: Springer International Publishing : Springer e-books : Imprint: Springer : Springer e-books).

Nilius, B., and Flockerzi, V. (2014b). Mammalian Transient Receptor Potential (TRP) cation channels. Volume I Volume I (Berlin; Heifelberg: Springer).

Nilius, B., and Owsianik, G. (2011). The transient receptor potential family of ion channels. Genome Biol *12*, 218.

Ong, E.C., Nesin, V., Long, C.L., Bai, C.X., Guz, J.L., Ivanov, I.P., Abramowitz, J., Birnbaumer, L., Humphrey, M.B., and Tsiokas, L. (2013). A TRPC1 protein-dependent pathway regulates osteoclast formation and function. J Biol Chem *288*, 22219-22232.

Ong, H.L., Chen, J., Chataway, T., Brereton, H., Zhang, L., Downs, T., Tsiokas, L., and Barritt, G. (2002). Specific detection of the endogenous transient receptor potential (TRP)-1 protein in liver and airway smooth muscle cells using immunoprecipitation and Western-blot analysis. Biochem J *364*, 641-648.

Orth, M., Kruse, N.J., Braun, B.J., Scheuer, C., Holstein, J.H., Khalil, A., Yu, X., Murphy, W.L., Pohlemann, T., Laschke, M.W*., et al.* (2017). BMP-2-coated mineral coated microparticles improve bone repair in atrophic non-unions. Eur Cell Mater *33*, 1-12.

Pani, B., and Singh, B.B. (2008). Darier's disease: a calcium-signaling perspective. Cell Mol Life Sci *65*, 205-211.

Paulsen, C.E., Armache, J.P., Gao, Y., Cheng, Y., and Julius, D. (2015). Structure of the TRPA1 ion channel suggests regulatory mechanisms. Nature *520*, 511-517.

Peng, J.B., Chen, X.Z., Berger, U.V., Vassilev, P.M., Tsukaguchi, H., Brown, E.M., and Hediger, M.A. (1999). Molecular cloning and characterization of a channel-like transporter mediating intestinal calcium absorption. J Biol Chem *274*, 22739-22746.

Rodda, S.J., and McMahon, A.P. (2006). Distinct roles for Hedgehog and canonical Wnt signaling in specification, differentiation and maintenance of osteoblast progenitors. Development *133*, 3231-3244.

Rumi, M.N., Deol, G.S., Singapuri, K.P., and Pellegrini, V.D., Jr. (2005). The origin of osteoprogenitor cells responsible for heterotopic ossification following hip surgery: an animal model in the rabbit. J Orthop Res *23*, 34-40.

Saotome, K., Singh, A.K., Yelshanskaya, M.V., and Sobolevsky, A.I. (2016). Crystal structure of the epithelial calcium channel TRPV6. Nature *534*, 506-511.

Sauer, B. (1998). Inducible gene targeting in mice using the Cre/lox system. Methods *14*, 381-392.

Schilit, S.L., Ohtsuka, M., Quadros, R.M., and Gurumurthy, C.B. (2016). Pronuclear Injection-Based Targeted Transgenesis. Curr Protoc Hum Genet *91*, 15 10 11-15 10 28.

Schindeler, A., McDonald, M.M., Bokko, P., and Little, D.G. (2008). Bone remodeling during fracture repair: The cellular picture. Semin Cell Dev Biol *19*, 459-466.

Schindl, R., Fritsch, R., Jardin, I., Frischauf, I., Kahr, H., Muik, M., Riedl, M.C., Groschner, K., and Romanin, C. (2012). Canonical transient receptor potential (TRPC) 1 acts as a negative regulator for vanilloid TRPV6-mediated Ca2+ influx. J Biol Chem *287*, 35612-35620.

Schwenk, F., Baron, U., and Rajewsky, K. (1995). A cre-transgenic mouse strain for the ubiquitous deletion of loxP-flanked gene segments including deletion in germ cells. Nucleic Acids Res *23*, 5080-5081.

Seth, M., Zhang, Z.S., Mao, L., Graham, V., Burch, J., Stiber, J., Tsiokas, L., Winn, M., Abramowitz, J., Rockman, H.A*., et al.* (2009). TRPC1 channels are critical for hypertrophic signaling in the heart. Circ Res *105*, 1023-1030.

Shapiro, F. (2008). Bone development and its relation to fracture repair. The role of mesenchymal osteoblasts and surface osteoblasts. Eur Cell Mater *15*, 53-76.

Shefelbine, S.J., Simon, U., Claes, L., Gold, A., Gabet, Y., Bab, I., Muller, R., and Augat, P. (2005). Prediction of fracture callus mechanical properties using micro-CT images and voxel-based finite element analysis. Bone *36*, 480-488.

Stegen, S., van Gastel, N., and Carmeliet, G. (2015). Bringing new life to damaged bone: the importance of angiogenesis in bone repair and regeneration. Bone *70*, 19-27.

Sternberg, N., Hamilton, D., Austin, S., Yarmolinsky, M., and Hoess, R. (1981). Site-specific recombination and its role in the life cycle of bacteriophage P1. Cold Spring Harb Symp Quant Biol *45 Pt 1*, 297-309.

Teitelbaum, S.L. (2007). Osteoclasts: what do they do and how do they do it? Am J Pathol *170*, 427-435.

Teitelbaum, S.L., and Ross, F.P. (2003). Genetic regulation of osteoclast development and function. Nat Rev Genet *4*, 638-649.

van der Eerden, B.C., Hoenderop, J.G., de Vries, T.J., Schoenmaker, T., Buurman, C.J., Uitterlinden, A.G., Pols, H.A., Bindels, R.J., and van Leeuwen, J.P. (2005). The epithelial Ca2+ channel TRPV5 is essential for proper osteoclastic bone resorption. Proc Natl Acad Sci U S A *102*, 17507-17512.

van der Eerden, B.C., Weissgerber, P., Fratzl-Zelman, N., Olausson, J., Hoenderop, J.G., Schreuders-Koedam, M., Eijken, M., Roschger, P., de Vries, T.J., Chiba, H*., et al.* (2012). The transient receptor potential channel TRPV6 is dynamically expressed in bone cells but is not crucial for bone mineralization in mice. J Cell Physiol *227*, 1951-1959.

Vassilev, P.M., Peng, J.B., Johnson, J., Hediger, M.A., and Brown, E.M. (2001). Inhibition of CaT1 channel activity by a noncompetitive IP3 antagonist. Biochem Biophys Res Commun *280*, 145-150.

Voets, T., Janssens, A., Prenen, J., Droogmans, G., and Nilius, B. (2003). Mg2+-dependent gating and strong inward rectification of the cation channel TRPV6. J Gen Physiol *121*, 245-260.

Walder, R.Y., Yang, B., Stokes, J.B., Kirby, P.A., Cao, X., Shi, P., Searby, C.C., Husted, R.F., and Sheffield, V.C. (2009). Mice defective in Trpm6 show embryonic mortality and neural tube defects. Hum Mol Genet *18*, 4367-4375.

Ward, W.E., Kim, S., Chan, D., and Fonseca, D. (2005). Serum equol, bone mineral density and biomechanical bone strength differ among four mouse strains. J Nutr Biochem *16*, 743-749.

Weissgerber, P., Kriebs, U., Tsvilovskyy, V., Olausson, J., Kretz, O., Stoerger, C., Mannebach, S., Wissenbach, U., Vennekens, R., Middendorff, R*., et al.* (2012). Excision of Trpv6 gene leads to severe defects in epididymal Ca2+ absorption and male fertility much like single D541A pore mutation. J Biol Chem *287*, 17930-17941.

Weissgerber, P., Kriebs, U., Tsvilovskyy, V., Olausson, J., Kretz, O., Stoerger, C., Vennekens, R., Wissenbach, U., Middendorff, R., Flockerzi, V.*, et al.* (2011). Male fertility depends on Ca^{2+} absorption by TRPV6 in epididymal epithelia. Sci Signal *4*, ra27.

Wen, S., Gotze, I.N., Mai, O., Schauer, C., Leinders-Zufall, T., and Boehm, U. (2011). Genetic identification of GnRH receptor neurons: a new model for studying neural circuits underlying reproductive physiology in the mouse brain. Endocrinology *152*, 1515-1526.

Wergedal, J.E., Sheng, M.H., Ackert-Bicknell, C.L., Beamer, W.G., and Baylink, D.J. (2005). Genetic variation in femur extrinsic strength in 29 different inbred strains of mice is dependent on variations in femur cross-sectional geometry and bone density. Bone *36*, 111-122.

Wes, P.D., Chevesich, J., Jeromin, A., Rosenberg, C., Stetten, G., and Montell, C. (1995). TRPC1, a human homolog of a Drosophila store-operated channel. Proc Natl Acad Sci U S A *92*, 9652-9656.

Wissenbach, U., Niemeyer, B., Himmerkus, N., Fixemer, T., Bonkhoff, H., and Flockerzi, V. (2004). TRPV6 and prostate cancer: cancer growth beyond the prostate correlates with increased TRPV6 Ca2+ channel expression. Biochem Biophys Res Commun *322*, 1359-1363.

Wissenbach, U., Niemeyer, B.A., Fixemer, T., Schneidewind, A., Trost, C., Cavalie, A., Reus, K., Meese, E., Bonkhoff, H., and Flockerzi, V. (2001). Expression of CaT-like, a novel calcium-selective channel, correlates with the malignancy of prostate cancer. J Biol Chem *276*, 19461-19468.

Wu, G., D'Agati, V., Cai, Y., Markowitz, G., Park, J.H., Reynolds, D.M., Maeda, Y., Le, T.C., Hou, H., Jr., Kucherlapati, R.*, et al.* (1998). Somatic inactivation of Pkd2 results in polycystic kidney disease. Cell *93*, 177-188.

Wu, J., Shih, H.P., Vigont, V., Hrdlicka, L., Diggins, L., Singh, C., Mahoney, M., Chesworth, R., Shapiro, G., Zimina, O.*, et al.* (2011). Neuronal store-operated calcium entry pathway as a novel therapeutic target for Huntington's disease treatment. Chem Biol *18*, 777-793.

Wu, L.J., Sweet, T.B., and Clapham, D.E. (2010). International Union of Basic and Clinical Pharmacology. LXXVI. Current progress in the mammalian TRP ion channel family. Pharmacol Rev *62*, 381-404.

Wyatt, A., Wartenberg, P., Candlish, M., Krasteva-Christ, G., Flockerzi, V., and Boehm, U. (2017). Genetic strategies to analyze primary TRP channel-expressing cells in mice. Cell Calcium *67*, 91-104.

Yagi, T., Nada, S., Watanabe, N., Tamemoto, H., Kohmura, N., Ikawa, Y., and Aizawa, S. (1993). A novel negative selection for homologous recombinants using diphtheria toxin A fragment gene. Anal Biochem *214*, 77-86.

Yamaza, T., Goto, T., Kamiya, T., Kobayashi, Y., Sakai, H., and Tanaka, T. (1998). Study of immunoelectron microscopic localization of cathepsin K in osteoclasts and other bone cells in the mouse femur. Bone *23*, 499-509.

Yoshida, H., Hayashi, S., Kunisada, T., Ogawa, M., Nishikawa, S., Okamura, H., Sudo, T., Shultz, L.D., and Nishikawa, S. (1990). The murine mutation osteopetrosis is in the coding region of the macrophage colony stimulating factor gene. Nature *345*, 442-444.

Zanou, N., Shapovalov, G., Louis, M., Tajeddine, N., Gallo, C., Van Schoor, M., Anguish, I., Cao, M.L., Schakman, O., Dietrich, A.*, et al.* (2010). Role of TRPC1 channel in skeletal muscle function. Am J Physiol Cell Physiol *298*, C149-162.

Zhang, D., Freedman, B.I., Flekac, M., Santos, E., Hicks, P.J., Bowden, D.W., Efendic, S., Brismar, K., and Gu, H.F. (2009). Evaluation of genetic association and expression reduction of TRPC1 in the development of diabetic nephropathy. Am J Nephrol *29*, 244-251.

Zhu, X., Chu, P.B., Peyton, M., and Birnbaumer, L. (1995). Molecular cloning of a widely expressed human homologue for the Drosophila trp gene. FEBS Lett *373*, 193-198.

Zubcevic, L., Herzik Jr, M.A., Chung, B.C., Liu, Z., Lander, G.C., and Lee, S.-Y. (2016). Cryo-electron microscopy structure of the TRPV2 ion channel. Nature Structural &Amp; Molecular Biology *23*, 180.

5.2 Own publications

1. Fecher-Trost C, Lux F, Busch K-M, **Raza A**, Hielscher F, Winter M, Belkacemi T, van der Eerden BC, Boehm U, Freichel M and Weissgerber P. (2018) Maternal transient receptor potential vanilloid 6 (*Trpv6*) is involved in offspring bone development, *Journal of Bone and Mineral Research,* in press.

2. **Raza A**, Saeed A, Ibrar A, Muddassar M, Khan AA and Iqbal J. (2012) Pharmacological evaluation and docking studies of 3-Thiadiazolyl- and Thioxo-1,2,4-triazolylcoumarin derivatives as cholinesterase inhibitors, *ISRN Pharmacol*.

3. Raza R, Saeed A, Arif M, Mahmood S, Muddassar M, **Raza A** and Iqbal J. (2012) Synthesis and biological evaluation of 3-thiazolocoumarinyl Schiff-base derivatives as cholinesterase inhibitors, *Chem Biol Drug Des.*

Submitted:

4. Wang H*, **Raza A***, Wardas B**,** Belkacemi A, Mannebach S, Qiao S, Aoki M, Birnbaumer L, Dietrich A, Philipp S, Boehm U, Beck A and Flockerzi V. (2018) TRPC1 tightly controls pituitary growth hormone release by mitigating TRPC5 function, *manuscript submitted.* (*contributed equally)

5. Beggs MR, Lee J, Busch K, **Raza A**, Dimke H, Weissgerber P, Engel J, Flockerzi V and Alexander RT. (2018) TRPV6 and $Ca_v1.3$ mediate small bowel calcium absorption in early life, *manuscript submitted.*

5.3 Abstracts

1. **Raza A**, Busch K-M and Flockerzi V. (2016) **"**Role of TRPC1 in bones". International Symposium on "Regulation of Cell Functions by Transient Receptor Potential Channels", Herrsching (Germany), 28 September – 01 October, 2016.

2. **Raza A**, Busch K-M, van der Eerden BC and Flockerzi V. (2017) "Co-relation of femur microarchitecture by µCT and histomorphometry in mice of different ages". 44th European Calcified Tissue Society (ECTS) Congress, Salzburg (Austria), 13 – 16 May, 2017.

3. Busch K-M, **Raza A,** Ullah S, Weissgerber P and Flockerzi V. (2017) "Correlation of femur microarchitecture in mice of different ages and backgrounds: Role of TRPV6". 42nd European Symposium on Hormones and Cell Regulation, Mont Ste. Odile (France), 04 – 07 October, 2017.

4. Wang H**, Raza A**, Wardas B, and Flockerzi V. (2018) **"**TRPC1 function in Ca^{2+} homeostasis". On-site review of Sonderforschungsbereich (SFB) TRR152, Homburg (Germany), 22 – 23 February, 2018.

5. Belkacemi A, **Raza A**, Busch K-M and Flockerzi V. (2018) **"**Ca_vß2-and Ca_vß3- dependent signal transduction". On-site review of Sonderforschungsbereich (SFB) 894, Homburg (Germany), 11 – 12 September, 2018.

6. Beck A, **Raza A**, Mannebach S and Flockerzi V. (2018) **"**Ca^{2+} channels in micro- and macroglial cells". On-site review of Sonderforschungsbereich (SFB) 894, Homburg (Germany), 11 – 12 September, 2018.

6 Supplementary data and information

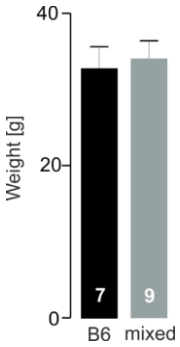

Figure 6-1 Comparison of weight between two strains of wild-type mice. Comparison of weight (grams, g) of 20-week-old male wild-type mice of two genetic backgrounds *i.e.* B6 strain, C57BL/6 and mixed strain, 129SvJ/C57BL/6 is shown. 'n' numbers of wild-type mice on B6 and mixed genetic backgrounds are seven and nine, respectively. Statistics: Mean ± SD, two-tailed unpaired student's t-test, with the number of mice indicated in the bars.

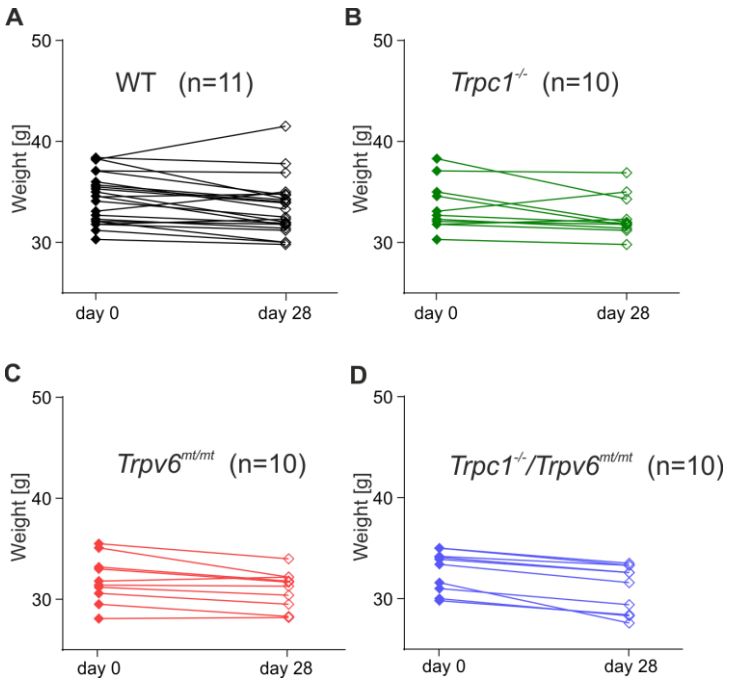

Figure 6-2 Comparison of weight before fracture and after the healing phase of wild-type, *Trpc1*$^{-/-}$, *Trpv6*$^{mt/mt}$ and double mutant *Trpc1*$^{-/-}$*/Trpv6*$^{mt/mt}$ mice. Comparison of weight (grams, g) at day 0 (before the surgical procedure) and at day 28 (after sacrificing the mice, still with the screws) of **(A)** WT **(B)** *Trpc1*$^{-/-}$ **(C)** *Trpv6*$^{mt/mt}$ and **(D)** *Trpc1*$^{-/-}$*/Trpv6*$^{mt/mt}$ mice is shown. 'n' numbers of WT, *Trpc1*$^{-/-}$, *Trpv6*$^{mt/mt}$ and *Trpc1*$^{-/-}$*/Trpv6*$^{mt/mt}$ mice are 11, 10, 10, 10 respectively.

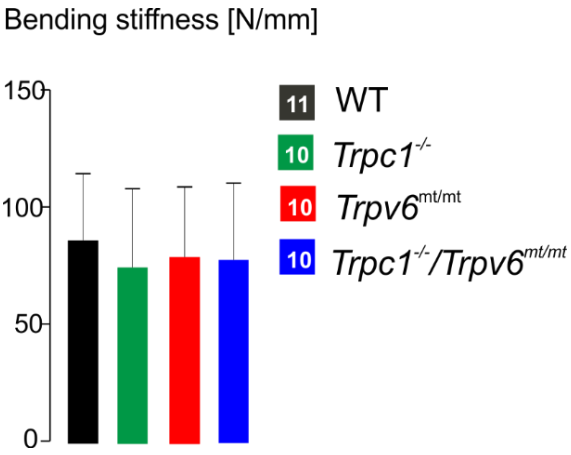

Figure 6-3 Biomechanical analyses of fractured femurs from 24-week-old male WT, *Trpc1*$^{-/-}$, *Trpv6*$^{mt/mt}$ and double mutant *Trpc1*$^{-/-}$*/Trpv6*$^{mt/mt}$ mice. Bending stiffness (N/mm) of fractured femurs analyzed by a non-destructive three-point bending test. Data shown as mean ± SD, calculated by one-way ANOVA followed by Bonferroni multiple comparison test. Four different colored bars represent four different genotypes: WT (black), *Trpc1*$^{-/-}$(green), *Trpv6*$^{mt/mt}$(red) and *Trpc1*$^{-/-}$*/Trpv6*$^{mt/mt}$ (blue) with 'n' representing number of femurs in each group are 11, 10, 10, and 10 respectively.

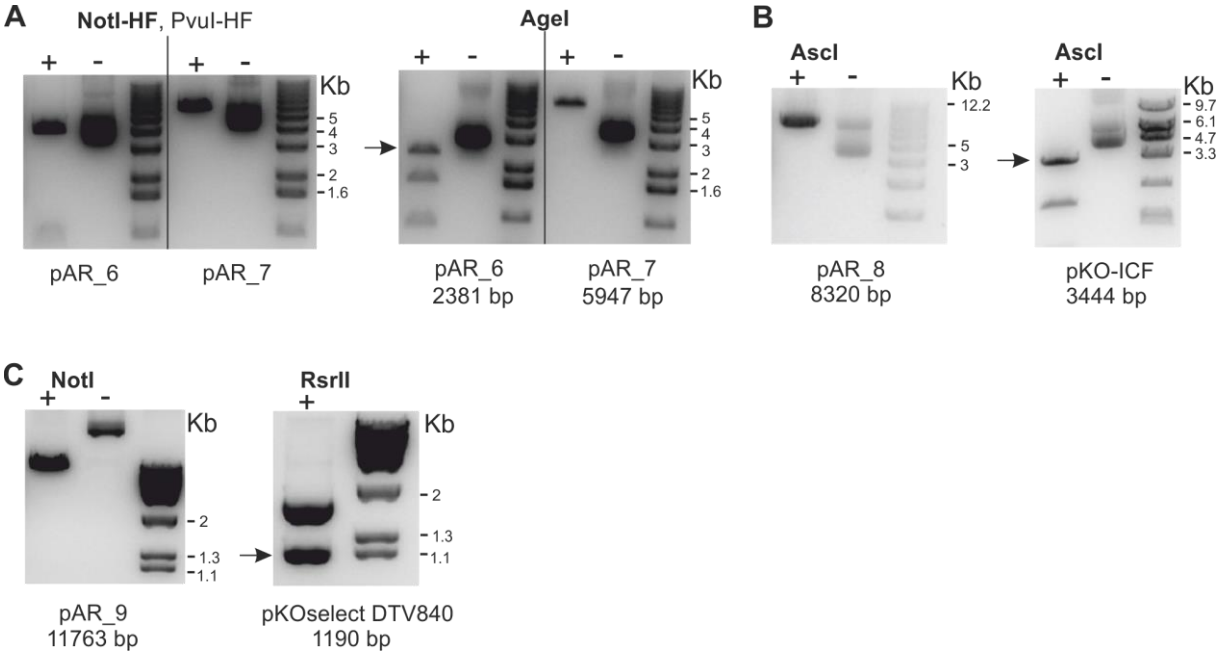

Figure 6-4 Cloning steps for the construction of the targeting construct, pAR_11, to generate the *Trpc1*-IC KI mouse strain. Agarose gel electrophoresis images show preparation of **(A)** pAR_6 and pAR_7 by sequential restriction enzyme cut, firstly, plasmids treated with (+) or without (-) restriction enzymes NotI-HF and PvuI-HF. Second cut with AgeI to obtain expected fragment size of 2381 bp (pAR_6) and 5947 bp (pAR_7). **(B)** Vector pAR_8 (8320 bp) and fragment pKO_ICF (3444 bp), arrow, after cut with the enzyme AscI. **(C)** Vector pAR_9 (11763 bp) and fragment pKOselect DTV840 (1190 bp), arrow, after cut with the enzymes NotI and RsrII, respectively. The signs + or – depict presence or absence of restriction enzymes in the reaction.

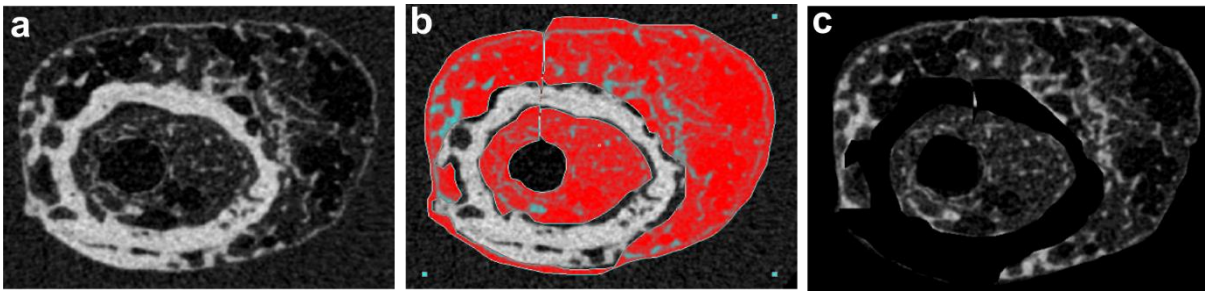

Figure 6-5 Selection of periosteal and endosteal calluses for analyses. Schematic representation of **(a)** a 6.5 µm cross-section with the cortical bone and periosteal and endosteal callus regions, **(b)** manually selected callus regions highlighted in red delineating the cortical bone in white, and **(c)** ROI consisting of only callus tissue for analyses.

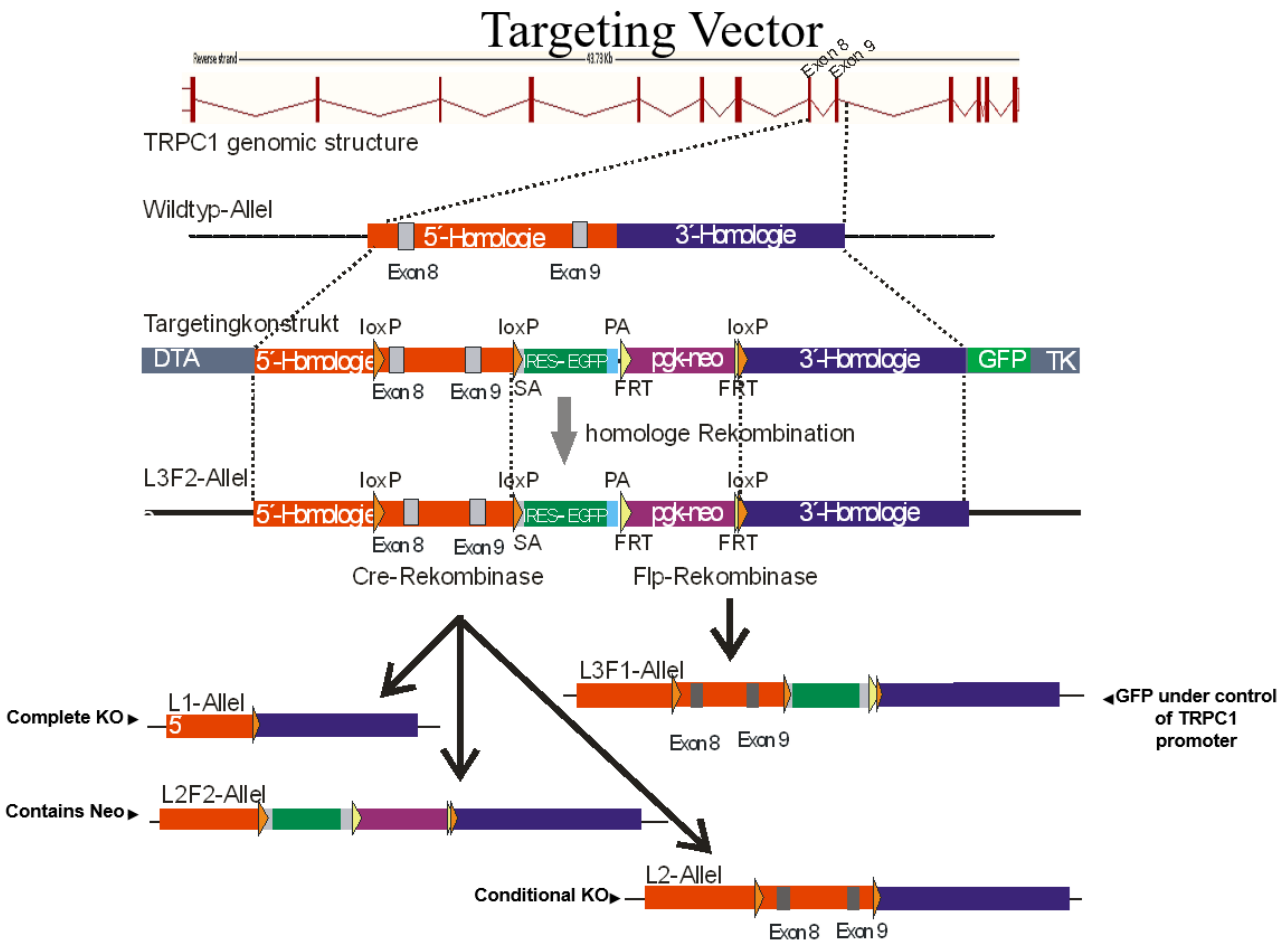

Figure 6-6 Abandoned targeting strategy for the generation of conditional *Trpc1* mouse strain by floxing the exons 8 and 9.

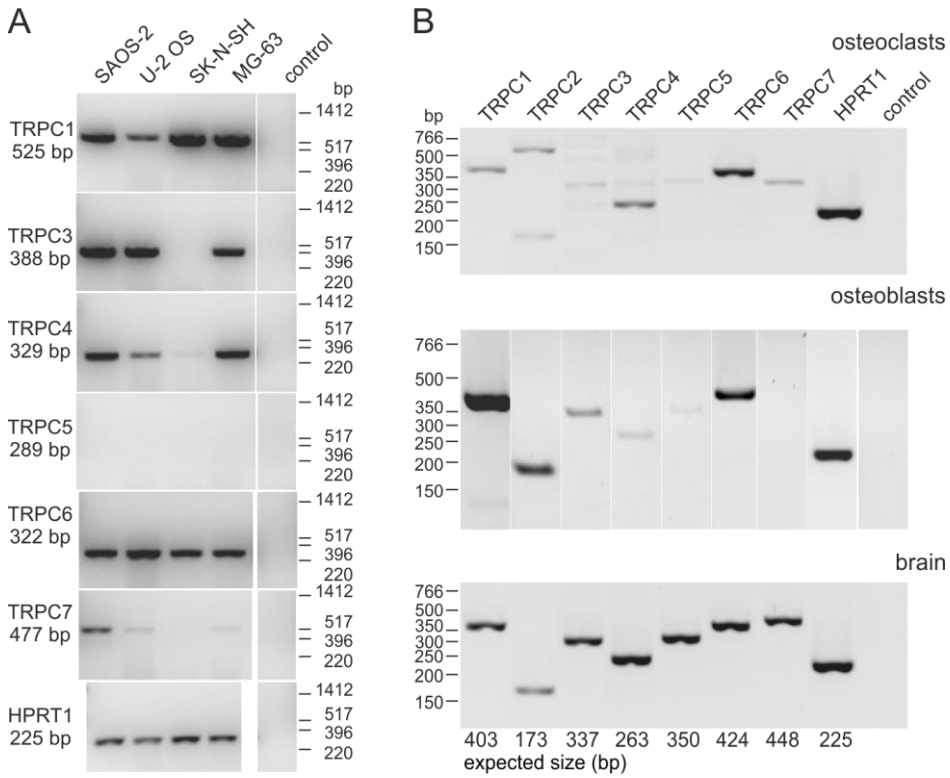

Figure 6-7 RT-PCR of *Trpc* transcripts with total RNA of **(A)** immortalized human osteoblast like cells and **(B)** bone marrow derived-osteoclasts (top), and bone derived-osteoblasts (middle), mRNA from brain served as a control (bottom), *Hprt1* was amplified as a positive control and water used a negative control.

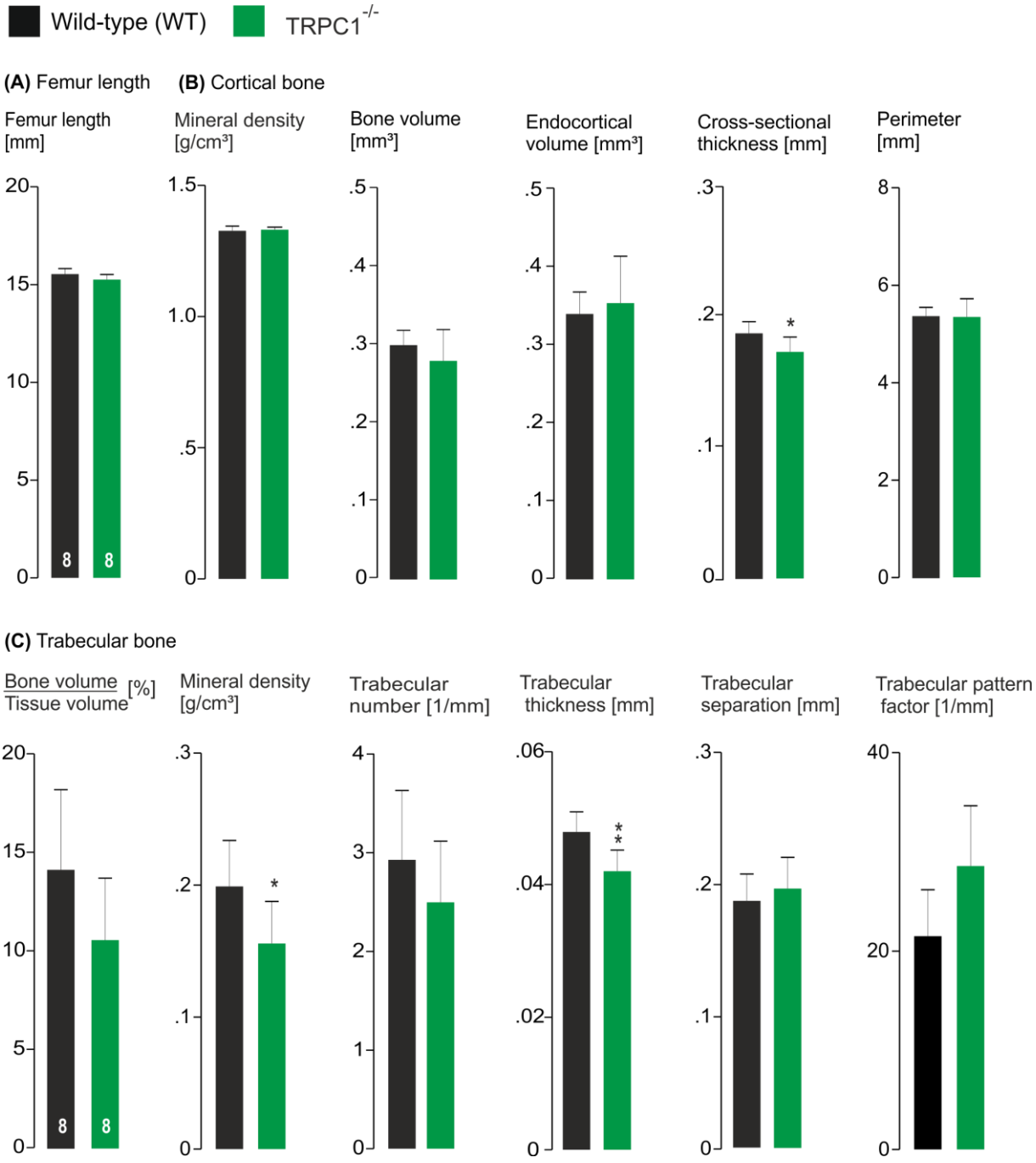

Figure 6-8 Femur length **(A)** and parameters of cortical- **(B)** and trabecular- **(C)** bone of wild-type and *Trpc1*$^{-/-}$ 12-week-old male mice on C57BL/6 (B6) genetic background determined by µCT. Data are shown as mean ± SD, analyzed by two-tailed unpaired t-test (* indicates p-value < 0.05, ** p-value < 0.01). The two genotypes are indicated in black (wild-type, WT) and green (*Trpc1*$^{-/-}$), with the number of femurs for WT and *Trpc1*$^{-/-}$ mice are 8 and 8, respectively.

Collection | Task list | Internal | External | Output/Report

Name	Description
Thresholding	Segment the foreground from background to binary images.
ROI shrink-wrap	Shrink a ROI to the boundary of a binarised object.
Despeckle	Remove speckles from images.
2D analysis	Calculate 2D parameters of binary images.
3D analysis	Calculate 3D parameters of binary images.
Save bitmaps	Save images to new folder.
Save bitmaps	Save images to new folder.

Table 6-1 Tasklist (Final_cortical_tasklist_Ahsan.ctt) for the determination of cortical bone parameters

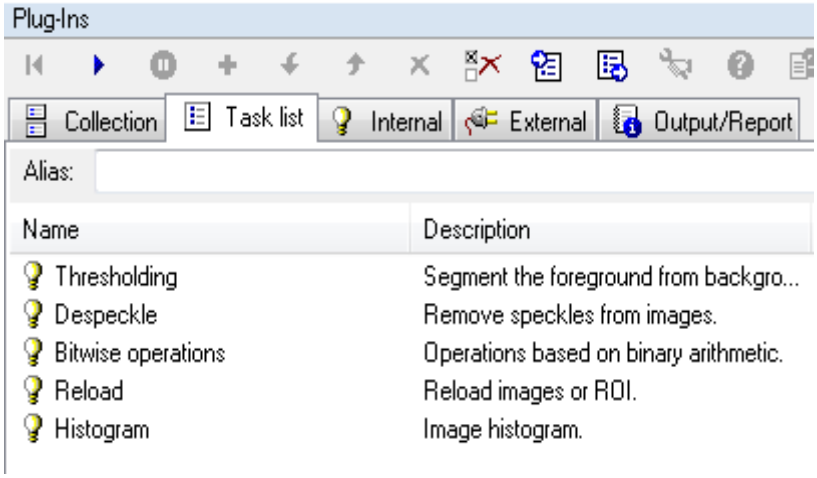

Table 6-2 Tasklist (Bruker_cortical (TMD)_tasklist_AR.ctt) for the determination of cortical TMD

Collection | Task list | Internal | External | Output/Report

Name	Description
Thresholding	Segment the foreground from background to binary images.
ROI shrink-wrap	Shrink a ROI to the boundary of a binarised object.
Despeckle	Remove speckles from images.
Bitwise operations	Operations based on binary arithmetic.
Morphological operations	Morphology-based operations.
Bitwise operations	Operations based on binary arithmetic.
Reload	Reload images or ROI.
Thresholding	Segment the foreground from background to binary images.
Morphological operations	Morphology-based operations.
Despeckle	Remove speckles from images.
Despeckle	Remove speckles from images.
Filtering	Smoothing, noise reduction and unsharping of images. The result is a grayscale image.
Thresholding	Segment the foreground from background to binary images.
Bitwise operations	Operations based on binary arithmetic.
Despeckle	Remove speckles from images.
Morphological operations	Morphology-based operations.
Bitwise operations	Operations based on binary arithmetic.
Morphological operations	Morphology-based operations.
Despeckle	Remove speckles from images.
Bitwise operations	Operations based on binary arithmetic.
Despeckle	Remove speckles from images.
Morphological operations	Morphology-based operations.
Reload	Reload images or ROI.
Thresholding	Segment the foreground from background to binary images.
Morphological operations	Morphology-based operations.
Despeckle	Remove speckles from images.
2D analysis	Calculate 2D parameters of binary images.
3D analysis	Calculate 3D parameters of binary images.
Save bitmaps	Save images to new folder.
Save bitmaps	Save images to new folder.

Table 6-3 Tasklist (Final_trabecular_tasklist_Ahsan.ctt) for the determination of trabecular bone parameters

Plug-Ins

Collection | Task list | Internal | External | Output/Report

Alias:

Name	Description
Histogram	Image histogram.

Table 6-4 Tasklist (Bruker_trabecular (BMD)_tasklist_AR.ctt) for the determination of trabecular BMD

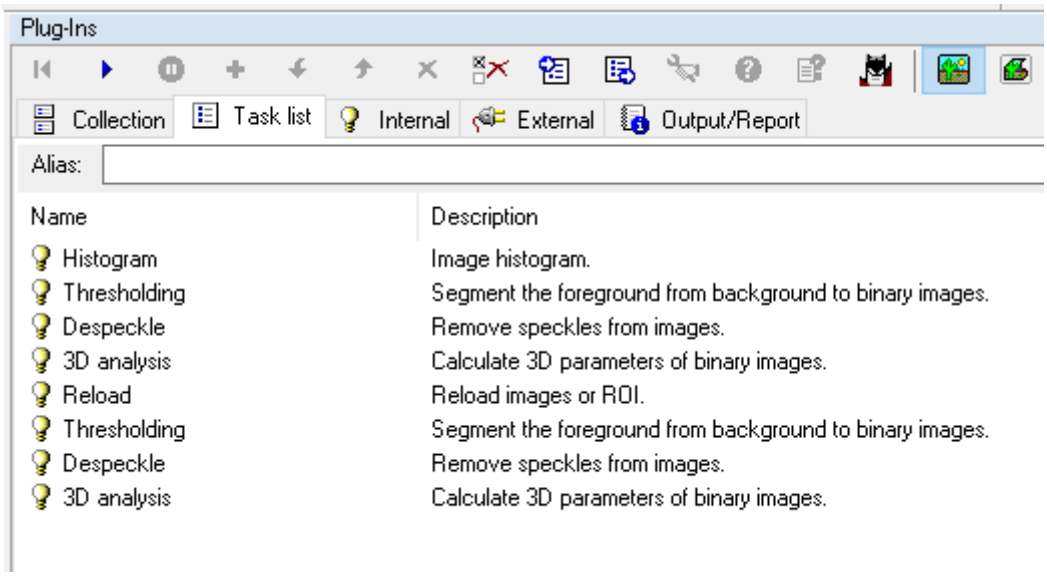

Table 6-5 Tasklist (AR_callus analysis_final.ctt) for the determination of callus tissue parameters.

Clone number	Euploid karyotype (%)	IBF (Heidelberg)	*iTL* (USA)	Pups (chimera) obtained	Number of F1 mice
13D2	100	✓	✓	1 (*iTL)*	-
13D3	86	✓		-	
13B4	77		✓	6	8
13B2	78		✓	1	-

Table 6-6 Summary of injections performed in Interfakultäre Biomedizinische Forschungseinrichtung (IBF), Heidelberg University, and *iTL* for the generation of *Trpc1*-IC mouse strain.

Clone number	Euploid karyotype (%)	IBF (Heidelberg)	*iTL* (USA)	Pups (chimera) obtained	Number of F1 mice
11D3	80	✓		-	
12A4	69	✓		-	
31D3	86	✓	✓	-	
32A1	79	✓	✓	1 (*iTL)*	-
31B2	71		✓	-	
32D2	85		✓	1	16
31D4	75		✓	5	7

Table 6-7 Summary of injections performed in Interfakultäre Biomedizinische Forschungseinrichtung (IBF), Heidelberg University, and *iTL* for the generation of conditional *Trpc1* mouse strain.